2017 REU REPORTS

• CNF • CNF iREU • HHMI EXROP • KEP •
• JHU PARADIM • PARADIM • PARADIM CALTECH SURF •
RESEARCH EXPERIENCE FOR UNDERGRADUATES PROGRAMS

Photographs of the 2017 REU Interns were taken by: Don Tennant, Julie Nucci, Kathy Springer, Melanie-Claire Mallison, and Georgia Tech staff.

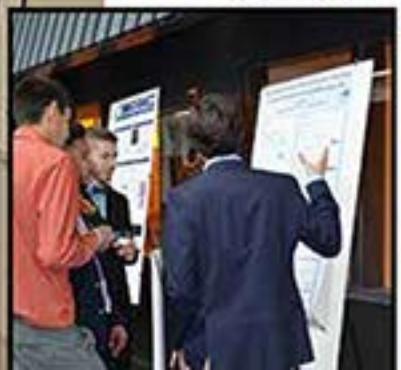

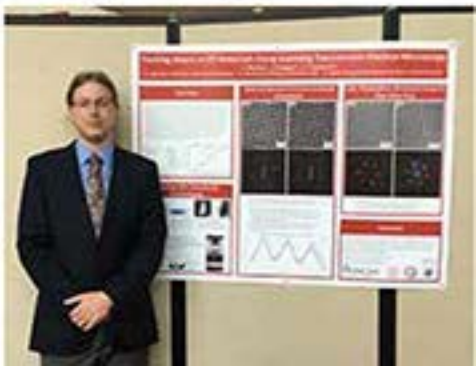

2017 Research Experience for Undergraduates Final Reports

REU PROGRAMS REPRESENTED

Cornell NanoScale Science & Technology Facility (CNF) & CNF International (CNF iREU) Program

Howard Hughes Medical Institute EXceptional Opportunities Program (HHMI EXROP)

Keeping the Ezra Promise Research Experience for Undergraduates (KEP REU) Program

Johns Hopkins University Platform for the Accelerated Realization, Analysis, and Discovery of Interface Materials Research Experience for Undergraduates (JHU PARADIM REU) Program

Platform for the Accelerated Realization, Analysis, and Discovery of Interface Materials Research Experience for Undergraduates (PARADIM REU) Program

Table of Contents

Fabrication of Dynamic Surfaces for in vitro Study of 'EMT' Progression 2
Robert P. Accolla, CNF iREU

Optimization of Microfluidic Devices for Formation of Supported Lipid Bilayers 4
Natalia M. Agosto Berríos, KEP REU

Characterization of Multiferroic Thin Films Generated with Molecular Beam Epitaxy 6
Margaret Anderson, PARADIM & Caltech SURF

Fluorescent DNA-Binding Proteins for Single Molecule Visualization 8
Dante M. Avalos, HHMI EXROP

Design and Manipulation of Ferroelectric Domains in $BaTiO_3$ Thin-Films.. 10
Daniel T. Bouman, PARADIM REU

Probing Single Crystal Growth Experimentally and through Computational Simulations 12
Heather Calcaterra, JHU PARADIM REU

Investigation of Atomic Layer Deposition for Distributed Bragg Reflectors . .. .14
Jonathan Chandonait, CNF REU

Synthesis of Core Substituted Napthalenediimides for n-Type Organic Semiconducting.. 16
Robert Chrostowski, CNF iREU

Compositional Analysis of Off-Stoichiometric Multiferroic $LuMnO_3$ and Electrode Nano-patterning of $(SrTiO_3)_n(BaTiO_3)_1SrO$ Thin Films.. ..18
Kaynan Goldberg, PARADIM REU

Electrical and Structural Characterization of Superconducting Ruthenate Ruddlesen-Popper Thin Films 20
Morgan Grandon, PARADIM REU

Bacterial Mechanics on a Chip . .. .22
Gabriel Guisado, CNF REU

Multi-Functional Platform for Characterization of Nanostructured Polymer Brushes. 24
Michael E. Klaczko, CNF REU

High Concentration Supporting Electrolytes for Enabling Stable Zinc Electrodeposition.. 26
Jadiel López González, KEP REU

Nanostamp Optimization for Single-Molecule DNA/Protein Array Studies 28
Mónica M. López Martínez, CNF REU

Exploring Thermoelectric Properties of Thin Film YbB_x 30
Maya Martirossyan, CNF iREU

An Investigation into the Effects of Quantum Structures on the Carrier Dynamics of GaAs/GaNAs Solar Cells.. 32
John Nance, CNF iREU

Growth Parameter Control of Structures and Properties of Perovskite Thin Films. 34
Skye Tackkett, CNF iREU

Piezoelectric Radio Frequency SAW-Based Energy Detectors. 36
Daniel Teal, CNF REU

Manipulation of Cell Spreading and Cytoskeleton of Stem Cells by Micropatterned Surfaces. 38
Cooper Thome, CNF iREU

Investigation of Ferroelectric Properties of Oxide Superlattices at Low Temperatures: How do Strain, Dimensionality, and Polarization Compete in the Low-Dimensional Structure, $(SrTiO_3)_n(BaTiO_3)_mSrO$? 40
Vibha Vijayakumar, PARADIM & Caltech SURF

Tracking Atoms in Two-Dimensional Materials Using Scanning TEM . .. .42
Jacob Waelder, PARADIM REU

Index . .. .44

Fabrication of Dynamic Surfaces for *in vitro* Study of 'Epithelial Mesenchymal Transition' Progression

Robert P. Accolla

Department of Biomedical Engineering, University of Florida

REU Program: 2017 Cornell NanoScale Science & Technology Facility International Research Experience for Undergraduates (CNF iREU) Program at the National Institute of Material Science (NIMS), Tsukuba, Ibaraki, Japan

CNF iREU Principal Investigator: Dr. Jun Nakanishi, Mechanobiology, NIMS-MANA

CNF iREU Mentor: Dr. Shota Yamamoto, Mechanobiology, NIMS-MANA

Primary Source of CNF iREU Funding: National Science Foundation under Grant No. OISE #1559368

Contact: raccolla@ufl.edu, nakanishi.jun@nims.go.jp, yamamoto.shota@nims.go.jp

Website: http://www.cnf.cornell.edu/cnf_2017reu.html

Abstract:

A dynamic extra cellular matrix (ECM) mimicking surface is introduced that allows tuning of surface bound compounds by ultraviolet irradiation. This is accomplished by synthesizing a photocleavable variant of cyclic Arginine-Glycine-Aspartate (cRGD), a known promoter of integrin-based cell adhesion [1,2], and manipulating its concentration in the presence of cells. Surfaces were fabricated from thin film deposited titanium and gold on borosilicate glass that was reacted with an ethylene glycol (EG_6) diluted mixture to create a heterogeneous monolayer. The resultant surfaces were cultured with Madin Darby Canine Kidney (MDCK) cells and irradiated to observe changes in phenotype and immunofluorescence. The design results in the ability to actively observe progression of epithelial mesenchymal transition (EMT)-like phenotype changes in the MDCK cell line.

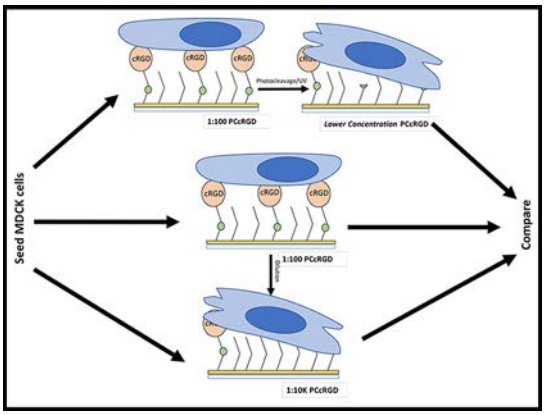

Figure 1: Strategy for observing and confirming EMT progression with dynamic PCcRGD surfaces.

Introduction:

EMT is a well-studied morphological change in epithelial cell lines where adherent, clustering cell populations transition into a migrating, mesenchymal phenotype due to changes in ECM adherence controlled by mechanical and biochemical cues [1]. This process has been shown to play a role in the progression of metastatic cancer, as it enables the movement of cancer cells throughout the body and away from the initial tumor site. The importance of one ECM component, cRGD, has been demonstrated previously with high surface densities yielding clustered cells and low densities resulting in EMT-like phenotypes.

The goal is to synthesize a photocleavable variant of surface-bound cRGD (PCcRGD) and demonstrate the ability to alter the overall cRGD concentration in the presence of MDCK cells and observe the progression of phenotype changes with real-time immunofluorescence imaging.

Summary of Research:

PCcRGD was synthesized by reacting cRGD with photocleavable PEG (PCP) in tetrahydrofuran (THF) with triethylamine (ET_3N) acting as a catalyst. This solution was reacted over 24 hours and then evaporated before being characterized by nuclear magnetic resonance (NMR) spectroscopy. Once the structure was confirmed, a 50 micromolar stock in methanol (MeOH) was made to fabricate surfaces. Pre-prepared borosilicate glass wafer layered with a 5 nm titanium nitride (TiN) mid-layer and a 20 nm gold (Au) top-layer were ozone cleaned and then reacted with 20 microliters of 1:100 and 1:10K PCcRGD:EG_6 dilution solutions (50 micromolar each) overnight in a sealed vessel. Surfaces were cleaned with MeOH and dried with nitrogen (N_2) before being placed in phosphate-buffered saline (PBS) in a 24-well plate.

The 1:100 dilution surfaces were irradiated with the gold surface facing down in PBS using 365 nm ultraviolet radiation for a dosage of 2.4 joules before being cultured with 2.0×10^4 MDCK cells per well (3.5 cm diameter circle). Cells were incubated at 37°C and 5% carbon dioxide (CO_2) for eight hours before being fixed, permeabilized, and stained for immunofluorescence of actin, phospho-myosin, and nucleus. This procedure created "pre-irradiation" surfaces, and a similar procedure was used for "post-irradiation" surfaces, where 2.0×10^4 MDCK cells per well were cultured onto each surface and allowed to adhere in an incubator

for three hours before being irradiated for a 2.4 joule dosage and then incubated for an additional five hours. Phase contrast and immunofluorescence imaging were done on a Zeiss single-channel microscope. Images were taken at 40x magnification with a 100-500 millisecond exposure time and then merged.

For live imaging of actin dynamics, MDCK cells were cultured at 1.1×10^4 cell per well in a 24-well plate and incubated overnight before being incubated for 12 hours with a solution of 2.5 microliters lipofectamine and 0.5 micrograms LifeAct-GFP DNA in 400 microliters MEM basic media per well. The 1:100 dilution surfaces were cultured with transfected cells, incubated for three hours, and then irradiated with a 2.4 joule dosage. Time-lapse imaging was done on an Olympus upright, single-channel microscope.

Results and Conclusions:

Analysis of pre-irradiation images shown in Figure 2 show results similar to those seen with traditional 1:10k cRGD surfaces [2] with degradation of the cortical actin surrounding cell clusters, formation of actin stress fibers across cells, and gaps in phospho-myosin at cell-cell junctions. Observation of the visual morphology of cells on surfaces with phase contrast imaging provided further evidence that PCcRGD surfaces behave similarly to cRGD surfaces fabricated by dilution. Post-irradiated surfaces showed identical changes in actin and phospho-myosin to a lesser degree, which infers that the surface is capable of changing cRGD density in the presence of cells, though the concentration of surface-bound PCcRGD after irradiation is between the 1:100 and 1:10k cRGD controls. Live imaging showed an increase in membrane ruffling in cells following exposure to irradiation, which is a result of actin formation in cytoplasmic protrusions found in migratory cells [3].

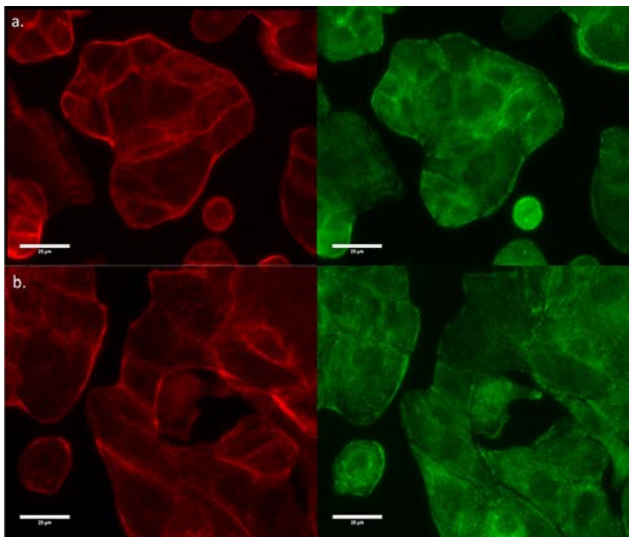

Figure 2: Immunofluorescence of MDCK cells on (a) 1:100 PCcRGD surface and (b) 2.4 J UV-irradiated 1:100 PCcRGD surface. Actin shown in red and phopsho-myosin shown in green.

Future Work:

The ability to observe progression of cell morphology is crucial for understanding the inner workings of EMT, however the issue of unknown concentration of surface-bound PCcRGD before and after irradiation makes comparison difficult. Future work will focus on developing procedures to do this, as well as exploring the cleavage rate of PCcRGD relative to irradiation dose. There is evidence that an additional cleavage reaction is occurring under specific experiment conditions shown in Figure 4, and this complicates the process of comparing to static cRGD surfaces. This cleavage mechanism must be identified and either controlled or used to reach the desired surface density.

Acknowledgments:

Author would like to recognize National Science Foundation grant OISE #1559368 for supporting this project. Author would also like to thank Dr. Shimaa Adellatef and the Nakanishi Lab for assistance and training.

References:

[1] de Rooij, J., et al. (2005). "Integrin-dependent actomyosin contraction regulates epithelial cell scattering." J Cell Biol 171(1): 153-164.

[2] Marlar, S., et al. (2016). "Reduced adhesive ligand density in engineered extracellular matrices induces an epithelial-mesenchymal-like transition." Acta Biomaterialia 39: 106-113.

[3] Cheresh, D. A., Leng, J., and Klemke, R. L. (1999). Regulation of Cell Contraction and Membrane Ruffling by Distinct Signals in Migratory Cells. The Journal of Cell Biology, 146(5), 1107-1116.

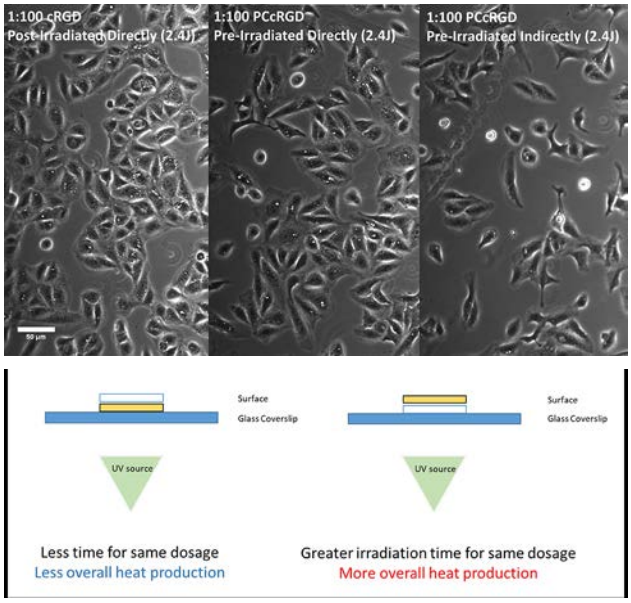

Figure 3, top: Morphology differences in MDCK cells based on orientation during UV irradiation. Figure 4, bottom: Orientation of samples during surface irradiation.

Optimization of Microfluidic Devices for Formation of Supported Lipid Bilayers

Natalia M. Agosto Berríos
Chemical Engineering, University of Puerto Rico, Mayagüez Campus (UPRM)

REU Program: 2017 Keeping the Ezra Promise Research Experience for Undergraduates (KEP REU) Program
KEP REU Principal Investigator: Prof. Susan Daniel, Robert Frederick Smith School of Chemical and Biomolecular Engineering, Cornell University
KEP REU Mentor: Lakshmi Nathan, Robert Frederick Smith School of Chemical and Biomolecular Engineering, Cornell University
Primary Source of KEP REU Funding: Keeping the Ezra Promise (KEP), Robert Frederick Smith School of Chemical and Biomolecular Engineering, Cornell University
CNF Tools Used: Heidelberg Mask Writer DWL66FS, Hamatech-Steag Mask Processors, Manual Resist Spinners, SUEX/ADEX Laminator, ABM Contact Aligner, SU-8 Hotplates
Contact: natalia.agosto@upr.edu, sd386@cornell.edu, ln258@cornell.edu
Website: http://www.cnf.cornell.edu/cnf_2017reu.html

Abstract:

Interactions between biological nanoparticles, like viruses, bacterial outer membrane vesicles, or oncogenic microvesicles, with cell membranes play important roles in the progression of disease. To get a better understanding of these nanoparticles, their interactions with supported lipid bilayers (SLBs) can be monitored using microscopy. SLBs act like cell membrane mimics and have the main features of cell membranes including proteins, lipids, and sugars. Forming SLBs within microfluidics enables control over the environment the nanoparticles are in, but bilayers formed this way tend to have plenty of defects. The goal of this study is to determine which microfluidic design results in bilayers with the fewest defects. Bilayers of 1-palmitoyl-2-oleoyl-sn-glycero-3-phosphocholine (POPC) were formed in devices of width ranging from 50 to 2000 µm and height from 200 to 500 µm. The mobility of lipids in these bilayers was tested using fluorescence recovery after photobleaching (FRAP) characterization. Microfluidic devices containing bigger channels dimensions stimulated formation of POPC supported lipid bilayers with fewer defects and higher lipid mobility.

Summary of Research:

Researchers need tools to perform analytical assays on biological nanoparticles-cell membrane interactions in a quick and safe manner to monitor virus evolution for vaccine development, screen new antiviral drugs, and study fundamental membrane fusion processes [1]. Studying these nanoparticles in live systems can be difficult; however, studying with *in vitro* systems using supported lipid bilayers (SLBs) make it easier. SLBs act like membrane mimics. This biomimetic material preserves lipid mobility and the planar geometry removes many experimental complications imposed by live cells [1]. Using microfluidic devices for formation of SLBs enables control over the nanoparticles' environment, however the Daniel group's current microfluidic design results in bilayers with plenty of defects. To counter this problem, we created three new microfluidics designs (Figure 1).

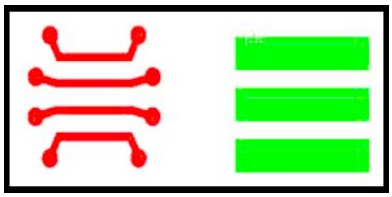

Figure 1: New designs for microfluidic devices (a) Design 1, Design 2; (b) Design 3.

For this study, Design 1 consisted of four channels of 5000 µm long, 500 µm wide, and 200 µm high. Design 2 had the same appearance and measurements as Design 1, except this device was 500 µm high. The last design, Design 3, consisted of three wider and longer channels, each one being 10,000 µm long and 2,000 µm wide by 200 µm. To test the quality of

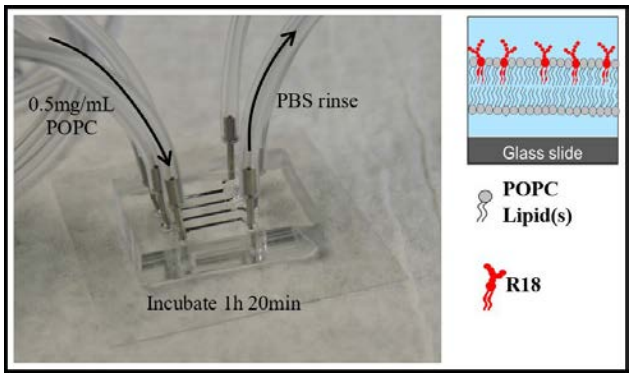

Figure 2: Formation of supported lipid bilayers (SLBs) with fluorescent label R18.

the bilayers formed in each microfluidic device, we examined the diffusion of the lipids within it, using fluorescence recovery after photobleaching (FRAP). In order to do this, 0.5mg/mL of POPC liposomes were added to either a polydimethylsiloxane (PDMS) well or injected into a microfluidic device and incubated for 1 h 20 min before rinsing it with phosphate-buffered saline (PBS) buffer (Figure 2).

Prior to the bilayer formation, the liposomes were fluorescently labeled with R18. This fluorescent label enabled the visualization of the lipid bilayers and was a probe for mobility measurements [1]. During the photobleaching experiment, the microscope shoots a laser light in one spot of the microfluidic channel, bleaching the R18 in it. Over time, the lipids will move around covering the bleached spot. The recovery data was fitted using a MATLAB code to calculate the diffusion coefficient using the two-dimensional solution of the Soumpasis equation:

$$D = \frac{w^2}{4t_{1/2}}$$

where w is the width of the bleached spot, and $t_{1/2}$ the time at which the bleached spot has recovered half of its original intensity. Also from this code we get a fractional recovery vs. time graph showing how the fluorescence intensity of the bleached spot changes over time, Fig. 3.

Results and Conclusions:

The images obtained from the FRAP analysis demonstrate that for bilayers formed in Design 1, the bleached spot did not recover. However, Design 3 demonstrated a fast fluorescent recovery. A comparison of the diffusion coefficient values (Figure 4) for all the microfluidic devices and PDMS well in a boxplot, showed that the closer values to 0.3 $\mu m^2/s$ corresponded to the PDMS well platform and microfluidics with Design 3. The average values were 0.302 and 0.298 $\mu m^2/s$, respectively. This confirms the information obtained from the microscopy imaging, wider channels dimensions stimulated the good formation of supported lipid bilayers.

Future Work:

Supported bilayers derived from cell membranes must be integrated to see if Design 3 still works for them as well.

Acknowledgements:

I thank Dr. Susan Daniel for hosting me in her research group, my mentor Lakshmi Nathan and all members of Daniel Research Group for training me on the techniques and useful discussions. Thank you for the funding via KEP and the Robert Frederick Smith School of Chemical and Biomolecular Engineering. Also, I thank Cornell NanoScale Facility, a member of the National Nanotechnology Infrastructure Network, which is supported by the National Science Foundation (Grant ECCS-1542081).

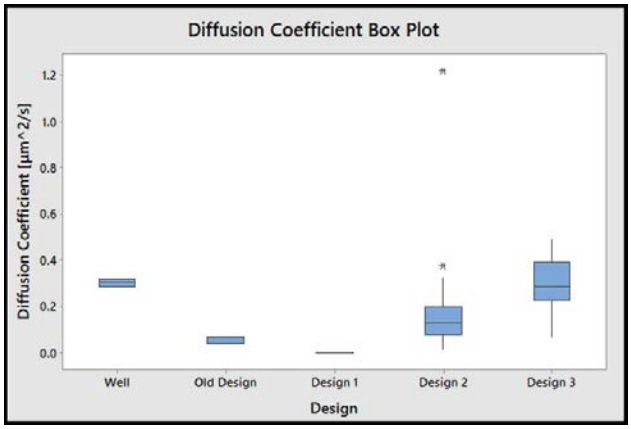

Figure 4: Comparison of diffusion coefficient of R18 in POPC supported lipid bilayers obtained from FRAP analysis under different experimental platforms.

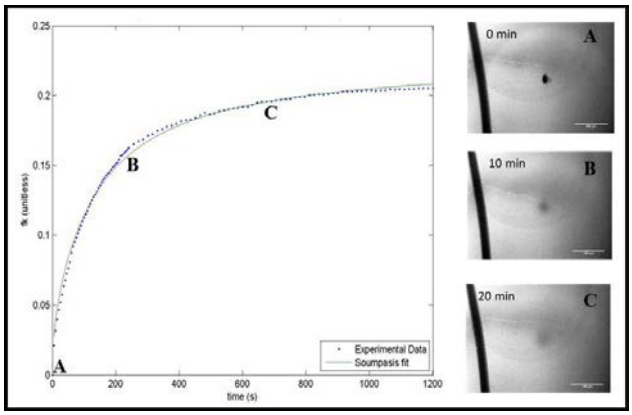

Figure 3: Diffusion of R18-labeled POPC supported lipid bilayer on a PDMS well with time after photobleaching.

References:

[1] Costello, D. A.; Hsia, C.; Millet, J. K.; Porri, T.; Daniel, S. Membrane Fusion-Competent Virus-Like Proteoliposomes and Proteinaceous Supported Bilayers Made Directly from Cell Plasma Membranes. Langmuir 2013, 29, 6409.6419.

Characterization of Multiferroic Thin Films Generated with Molecular Beam Epitaxy

Margaret Anderson
California Institute of Technology

REU Program: 2017 Platform for the Accelerated Realization, Analysis, and Discovery of Interface Materials Research Experience for Undergraduates (PARADIM REU) Program with Caltech SURF
PARADIM REU Principal Investigator: Darrell Schlom, PARADIM Director, Materials Science and Engineering, Cornell University
PARADIM REU Mentor: Rachel Steinhardt, Materials Science and Engineering, Cornell University
REU Caltech Co-Mentor: Katherine Faber, Materials Science, California Institute of Technology
Primary Sources of PARADIM REU Funding: NSF Materials Innovation Platform Program, Grant # DMR-1539918; Caltech Student-Faculty Programs Summer Undergraduate Research Fellowship (SURF)
Contact: maanders@caltech.edu, ds636@cornell.edu, rs963@cornell.edu
Website: http://www.cnf.cornell.edu/cnf_2017reu.html

Abstract:

Magnetoelectric multiferroic thin films exhibit coupled ferromagnetism and ferroelectricity. Interest in these multiferroics stems from their potential applications in spin-based computing and novel information storage methods. Through characterization with x-ray diffraction (XRD), atomic force microscopy (AFM), and vibrating sample magnetometry (VSM), the growth of multiferroic films with molecular beam epitaxy (MBE) was optimized. Both strain-coupled Fe_xGa_{1-x} composites and rare earth ferrite superlattices were studied. Additionally, this study searched for compatible bottom electrodes that facilitate the measurement of the ferroelectric properties of the films. Because the electrodes are necessarily located between the substrate and the film, all three must have compatible crystal lattice parameters in order to grow successfully with MBE. Characterization of the electrodes with XRD omega rocking curves and AFM revealed that PIN-PMN-PT produced slightly better iridium electrodes and Fe_xGa_{1-x} films than PMN-PT.

Methods:

X-ray Diffraction. X-ray diffraction was conducted with a Rigaku Smartlab X-ray Diffractometer with a Ge 220 monochrometer on the incident side in a parallel beam (PB) configuration. Samples were placed on misoriented single crystal silicon during scanning to limit the background signal — θ-2θ scans were used to verify composition, phase, and orientation of the epitaxial thin films. Based on Bragg's law, x-rays incident on the crystalline sample at a Bragg angle (determined by the presence and separation of crystal planes within the material) diffract with a relative displacement equal to an integer multiple of their wavelength. As a result, the x-rays interact with constructive interference, producing a peak in a θ-2θ scan at the Bragg angle — ω-rocking curves gave a measure of structural crystal quality. By 'rocking' the incident angle of the x-rays near a Bragg angle in XRD, the width of a peak can give an indication of the quality of the crystal. If the crystal was absolutely perfect, the rocking curve would have a FWHM of nearly 0 degrees. The only angle that would satisfy Bragg's law and diffract x-rays would be the exact Bragg angle. However, defects within the crystal introduce slight changes in the orientation of the crystal planes and diffract x-rays at angles slightly off from the exact Bragg angle of a theoretically pure crystal, thereby widening the peak. Therefore, by performing rocking curve measurements, the structural quality of crystal samples can be determined by the FWHM of the resulting peak.

Atomic Force Microscopy. An Asylum Research MFP-3D scanning probe microscope system in AC tapping mode was used to evaluate the surface quality of samples. AFM uses the change in amplitude of a harmonically oscillating cantilever to map the surface features of a sample. The calculated height of the sample at each position is represented as a colored pixel and arranged spatially to produce an image of the surface. RMS surface roughness, a measure of the average deviation of the film surface from a perfectly flat plane, was used to evaluate the smoothness of film growth.

Vibrating Sample Magnetometry. A 9T Quantum Design Physical Property Measurement System (PPMS) with a vibrating sample magnetometer was used to evaluate the magnetic properties of Fe_xGa_{1-x} thin films. Measurements were conducted at room temperature. By oscillating the sample in a sweeping external magnetic field, a hysteresis loop characteristic of ferromagnetic materials was generated. The raw data was the summation of the magnetic signal from both the sample and the diamagnetic substrate. The result is the sloped loop shown below in Figure 1.

The diamagnetic signal from the substrate is characteristically a negatively sloped straight line. The slope of this line was determined via regression on the tails of the uncorrected hysteresis loop (Figure 2). The result was subtracted from the data. To quantify the

magnetic moment in emu/cm^3, the data was divided by the volume of the Fe_xGa_{1-x} film, resulting in the final hysteresis loop used to describe the ferromagnetic properties of the film.

Molecular Beam Epitaxy. The samples in this study were grown by reactive-oxide molecular beam epitaxy (MBE) using a Veeco Gen 10 growth chamber. My graduate student mentor, Rachel Steinhardt, grew all of the films characterized here because the complex method of MBE was beyond the scope of a ten-week fellowship. In MBE, pure samples of each element within the desired structure are heated within a crucible, called an effusion cell, to produce a 'beam' that is directed towards the heated substrate. The elements are deposited on the substrate, producing an epitaxial crystalline film. By varying each element's flux rate, substrate temperature, and the pressure of O_2 and ozone within the growth chamber, complex and atomically ordered crystalline films can be grown with high precision.

In order to grow high quality epitaxial crystals, the films must be grown on structurally compatible substrates. For example, lutetium ferrite has a hexagonal structure, rather than the cubic structure of many perovskites grown with MBE. Yttria-stabilized zirconium (YSZ) has a cubic structure that is generally incompatible with the hexagonal ferrites. Yet, when cut to expose the <111> crystallographic plane, the surface behaves hexagonally (Figure 3). Therefore YSZ <111> is a suitable substrate for lutetium ferrite superlattice growth.

Acknowledgments:

This work was supported by the NSF via the Platform for the Accelerated Realization, Analysis, and Discovery of Interface Materials (PARADIM) under Cooperative Agreement No. DMR-1539918, and made use of the Cornell Center for Materials Research Shared Facilities, which are supported through the NSF MRSEC program (DMR-1120296). I would like to thank Professor Darrell Schlom for his advice and kindness during this research experience. Special thanks to Rachel Steinhardt for her technical guidance and dedication to making my summer a success. I would also like to thank Professor Katherine Faber for agreeing to act as my faculty co-mentor at Caltech. Finally, I would like to thank the Caltech Student-Faculty Programs office for the opportunity to participate in the Summer Undergraduate Research Fellowship and all of the personnel at both Caltech and Cornell that offered welcome advice and assistance in my voyage across the country to have this world-class research fellowship.

Find Margaret's full Caltech report online at http://paradim.cornell.edu/education/2017-reu-participants/

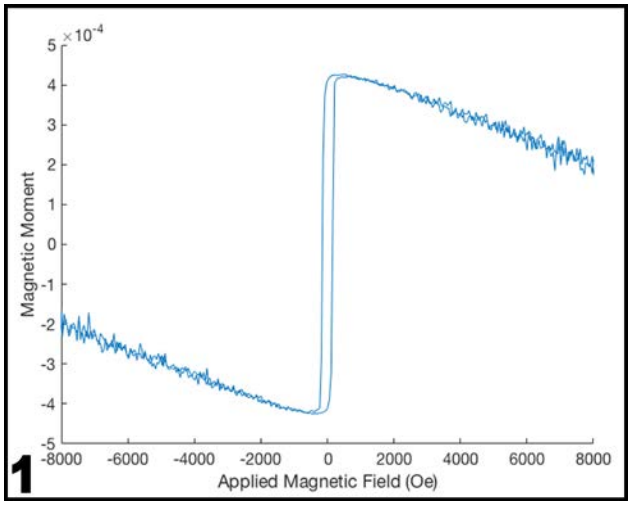

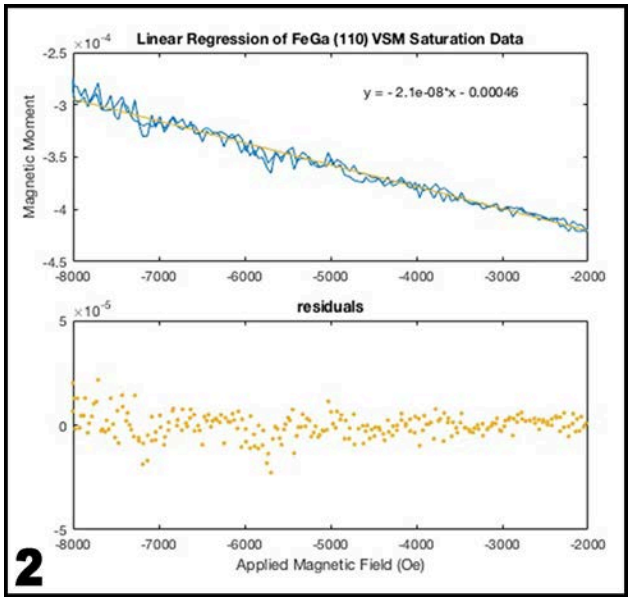

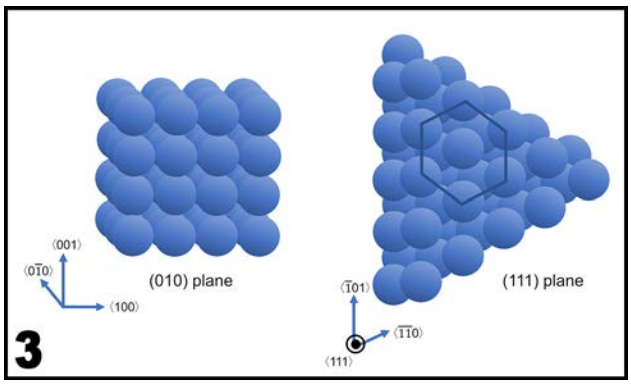

Figure 1, top: Uncorrected M vs. H hysteresis loop for an Fe_xGa_x film on PIN-PMN-PT measured in the <110> direction.

Figure 2, middle: Linear regression on the lower tail of <110> uncorrected data. Residuals show random scatter indicating that the linear model is valid. The slope of the equation in the upper graph was used as the slope of the linear diamagnetic signal subtracted from the raw data.

Figure 3, bottom: On the left is a simple cubic crystal structure. When sliced to expose the <111> plane, the result is a hexagonal structured surface as depicted on the right. A similar hexagonal structure is produced along the <111> of a face-centered cubic crystal like YSZ. Crystallographic directions are shown for reference.

Fluorescent DNA-Binding Proteins for Single Molecule Visualization

Dante M. Avalos

Biochemistry, New Mexico State University

REU Program: 2017 Howard Hughes Medical Institute EXceptional Opportunities Program (HHMI EXROP)

HHMI EXROP REU Principal Investigator: Dr. Michelle D. Wang, Laboratory of Atomic and Solid State Physics, Cornell University; Howard Hughes Medical Institute, Cornell University

HHMI EXROP REU Mentors: Dr. James E. Baker, Laboratory of Atomic and Solid State Physics, Cornell University; Dr. Chuang Tan, Laboratory of Atomic and Solid State Physics, Cornell University

Primary Source of Research Funding: Howard Hughes Medical Institute EXceptional Opportunities Program (HHMI EXROP)

Contact: toad@nmsu.edu, mdw17@cornell.edu, jeb94@cornell.edu, tc542@cornell.edu

Website: http://www.cnf.cornell.edu/cnf_2017reu.html

Abstract:

Single molecule manipulation techniques are powerful tools to examine the physical properties of nucleic acid biopolymers. Although the width of DNA is well below the diffraction limit, many remarkable studies have been achieved by monitoring microsphere handles attached to the nucleic acids. Combining single-molecule manipulation techniques with fluorescence visualization methods may open new pathways for future nucleic acid studies. Novel fluorescent DNA-binding proteins have recently been developed and could serve as a reversible method of visualizing DNA directly [1]. This study aims at complimenting single molecule manipulation techniques with fluorescent DNA-binding proteins. *Escherichia coli* (*E. coli)* cells were transformed in order to purify fluorescent DNA-binding proteins of interest. These proteins were then used in simple single molecule experiments to verify functionality. Fully characterized proteins will be incorporated into future single-molecule manipulation studies to enhance measurement capabilities.

Introduction:

Deoxyribonucleic acid (DNA) is a vital polymer in every known organism, which contains all of the genetic information of those organisms. DNA is essential in the biological processes of transcription and replication. These processes require molecular motors, which both recognize and temporarily alter the mechanical configuration of DNA [2]. Functional DNA topology is maintained through various enzymatic pathways, indicating the importance of torsional strain on individual DNA strands. If the DNA structure is not maintained, processes like transcription will fail or produce mutated products [3], which can cause death or disease to multicellular organisms.

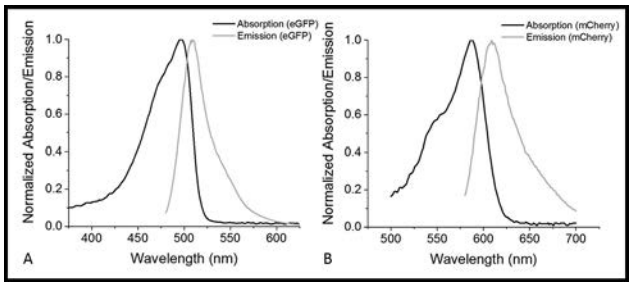

Figure 1: Measured spectra of eGFP-DBP (A) and mCherry-DBP (B) at their excitation and emission wavelengths.

This research aims at using fluorescent DNA-binding proteins (FDBP) to enhance these techniques by allowing visualization of individual strands of DNA.

Methods:

Protein Purification. *E. coli* cells (BL21 DE3) were transformed to express two FDBPs: eGFP DNA-binding protein (eGFP-DBP) and mCherry DNA-binding protein (mCherry-DBP). These proteins were purified using a Ni-NTA column followed by dialysis. The absorption and emission spectra of the purified proteins were characterized (Figure 1) and were in agreement with published values.

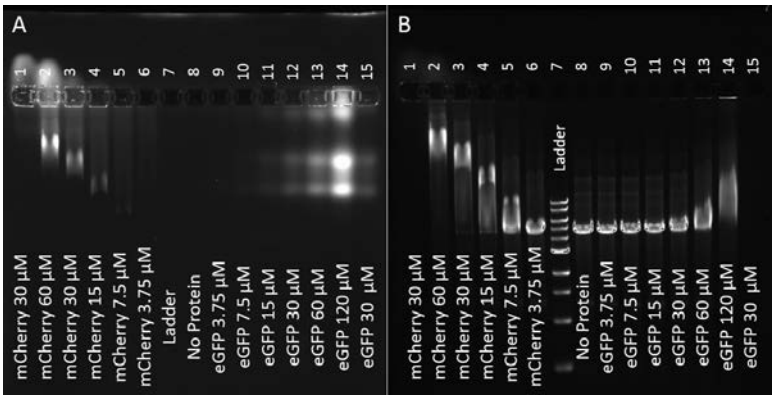

Figure 2: Gel mobility assay for determining DNA-Binding ability of both FDBPs. All lanes (except lanes 1 and 15) include 150 ng of 4.7 kbp DNA. Contents are labeled on each lane. (A) mCherry (left) and eGFP (right) fluorescence. (B) DNA stained with ethidium bromide.

DNA-Binding Characterization. The ability of the proteins to bind DNA was characterized by gel electrophoresis. Bound proteins are expected to slow the travel of the DNA through the gel, varying with concentration. Figure 2 shows that mCherry-DBP bound DNA, as indicated by the reduction of DNA travel with increasing protein concentration. eGFP-DBP bound DNA less efficiently, and furthermore, two strong bands appear on Figure 2a on eGFP-DBP lanes, reflective of a degraded protein. This behavior may result from the DNA-binding region coming apart from the eGFP domain in the FDBP.

Single-Molecule Visualization. Single-DNA visualization was attempted by fluorescence microscopy after incubating FDBP with surface-anchored DNA in a single-molecule flow chamber. Single-molecule chambers were established between two microscope coverslips fastened by double-sided tape. Chambers were first incubated with anti-digoxigenin (5 ng/µl), and then passivated with either casein from bovine milk (10 ng/µl) or bovine serum albumin (BSA, 5 ng/µl). DNA template (48 kbp, 8.3 nM), end-labeled with digoxigenin, was then incubated in order to anchor to the surface. After thorough rinsing with PBS, FDBPs were flowed through the chamber. Due to strong non-specific adsorption by FDBPs, variations in chamber preparation were attempted. Notably, pre-incubation of FDBP with DNA, along with patterning of the anti-digoxigenin were attempted without significant reduction in non-specific surface attachment of FDBP. Expected DNA attachment was confirmed using SYTOX Green DNA stain. All of these attempts appeared nearly identical to Figure 3. The protein appeared to readily adsorb to the surface, even at concentrations as low as 0.5 nM. The resulting background fluorescence prevented visualization of anchored DNA.

Future Work:

Binding of eGFP-DBP to DNA needs to be further characterized, and new protein may need to be expressed and purified. Non-specific adsorption of FDBPs to surfaces in single-molecule flow chambers is currently a significant limitation.

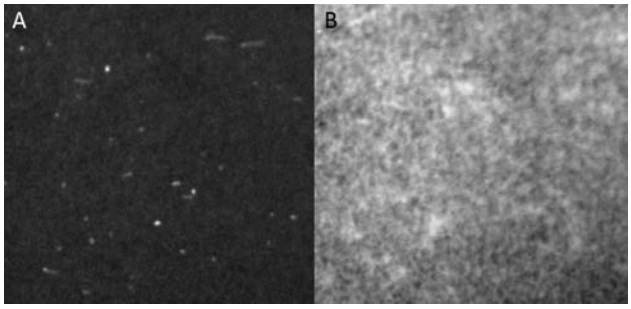

Figure 3: Representative fluorescence microscopy images. (A) SYTOX Green DNA stain fluorescence. (B) mCherry fluorescence.

Passivation can be improved with additional protein characterization (e.g. isoelectric point), concentration tuning, and alternative approaches (e.g. lipid bilayer passivation). Protein concentration for single-molecule visualization also needs further optimization. After optimization, we expect to conduct single-molecule DNA studies with the added visualization functionality provided by FDBPs.

Acknowledgements:

The authors would like to thank Cornell NanoScale Facility REU Program for hosting D.M.A., and Jaeyoon Lee and Ryan Badman for offering insight during the project. Many thanks to the Howard Hughes Medical Institute EXceptional Opportunities Program (HHMI EXROP) for funding this internship.

References:

[1] Lee, S., et al. (2015) DNA binding fluorescent proteins for the direct visualization of large DNA molecules. Nucleic Acids Research 2016 vol. 44, No. 1 e6.

[2] Liu, L. F., and Wang, J. C. (1987) Supercoiling of the DNA template during transcription. Proc. Natl. Acad. Sci. USA Vol. 84, pp. 7024-7027.

[3] Chong, S., et al. (2014) Mechanism of Transcriptional Bursting in Bacteria. Cell 158, 314-326.

Design and Manipulation of Ferroelectric Domains in $BaTiO_3$ Thin-Films

Daniel T. Bouman

Chemistry, Department of Chemistry and Biochemistry, California State University, Fullerton

REU Program: 2017 Platform for the Accelerated Realization, Analysis, and Discovery of Interface Materials Research Experience for Undergraduates (PARADIM REU) Program

PARADIM REU Principal Investigator: Darrell G. Schlom, PARADIM Director, Kavli Institute at Cornell for Nanoscale Science, Cornell University

PARADIM REU Mentor: Eric Langenberg, Department of Materials Science and Engineering, Cornell University

Primary Source of PARADIM REU Funding: NSF Materials Innovation Platform Program, Grant # DMR-1539918

Contact: danieltbouman@csu.fullerton.edu, schlom@cornell.edu, eric.langenberg.perez@gmail.com

Website: http://www.cnf.cornell.edu/cnf_2017reu.html

Abstract and Introduction:

As devices miniaturize, the ability to control nanoscale ordering in ferroelectric materials is important for emerging technologies. Ferroelectric materials exhibit spontaneous polarization and respond hysteretically to electric fields making them attractive for incorporation into devices, such as, non-volatile random-access memory (RAM). Additionally, locally ordered polarized regions form domains that are separated by domain walls (DWs) favorably formed from the minimization of electrostatic interactions between domains of opposing polarization. DWs have properties that differ from the ferroelectric domains and are uniquely mobile. For this reason, control of ferroelectric DW formations is desired for future nanoscale devices and functional optimization. Controlled engineering of domain wall patterns in complex ferroelectric oxides provides an avenue to new nanostructured devices realized by writing, erasing, and moving DWs. Mobile ferroelastic DW configurations can be manipulated to control phonon transportation, promoting novel applications in phononics. Here, using strain engineering, we design a variety of phases and DW configurations in ferroelectric $BaTiO_3$ films [1].

Previously, up/down polarization has been exploited in ferroelectric memory devices. However, limited attention has been given to in-plane polarized ferroelectrics. Recently, large lattice parameter substrates capable of inducing tensile strain in $BaTiO_3$ have been developed to promote in-plane polarization. Biaxial strain achieved during epitaxy, where the ferroelectric thin-film adopts the underlying substrate in-plane lattice in the paraelectric phase (a_0 = 4.007 Å), gives two types of strain depending on the lattice mismatch [2]. Substrates with smaller lattice parameter induce compressive strain, leading to up/down polarization, while substrates with larger lattice constants produce tensile strain, promoting in-plane polarization [3].

The substrates investigated were *Re*ScO_3 (*Re* = Gd, Sm, Nd, Pr), La_2LuScO_6, and $LaLuO_3$, which have orthorhombic structures (*Pbnm*; *No.* 62), but can be represented as pseudocubic. Substrate averaged psuedocubic lattice constants, in Ångströms, are as follows, respectively: 3.968, 3.987, 4.008, 4.020, 4.113, 4.184. $BaTiO_3$ films were grown on the above, single crystal perovskite substrates, by reactive molecular

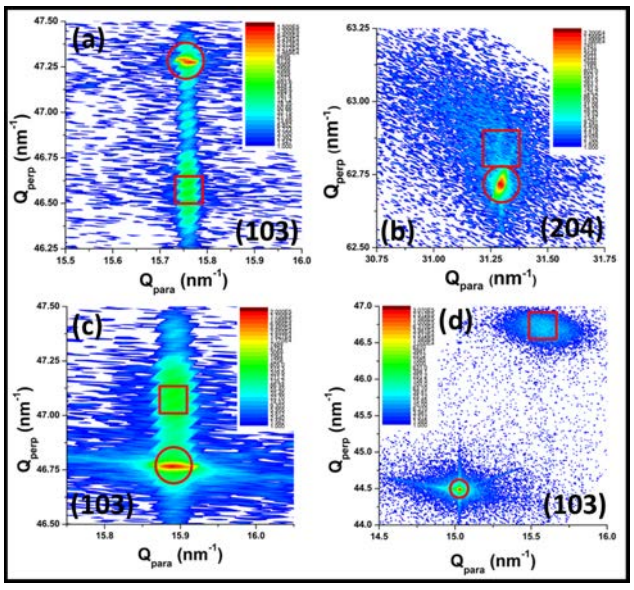

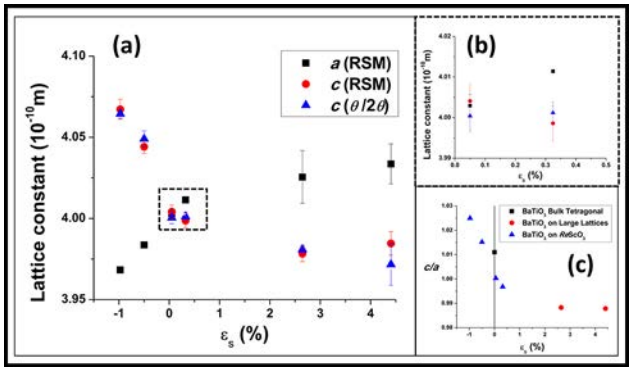

Figure 1, left: Reciprocal Space Maps (RSM) of $BaTiO_3$ on various substrates with reflections indicated: $SmScO_3$ (a), $NdScO_3$ (b), $PrScO_3$ (c), and $LaLuO_3$ (d). Film signals identified by squares and substrates by circles. Figure 2, above: Lattice constants of $BaTiO_3$ thin-films determined by x-ray diffraction θ-2θ scans and reciprocal space mapping (RSM) as a function of strain, (a), with 0-0.5% misfit strain in (b) for clarity, and tetragonality in (c).

beam epitaxy, spanning from -0.97% compressive strain to +4.40% tensile strain, with misfit strain defined beforehand [2]. X-ray diffraction (XRD) and piezoresponse force microscopy (PFM) measurements were used to identify different domains and phases in strained $BaTiO_3$ films.

Results and Conclusions:

Structural Characterization. XRD θ-2θ scans and reciprocal space mapping (RSM) techniques were employed to determine how the $BaTiO_3$ structure varied with epitaxial strain and the resulting phase. From RSM of a compressive film, seen in Figure 1a, the signal of $BaTiO_3$ appears below the $SmScO_3$ signal, indicating a fully strained, coherent film, stabilizing a *c*-domain with polarization along the [001]. Low strain tensile in $BaTiO_3$ on $NdScO_3$ was resolved using the (204) reflection, seen in Figure 1b. RSM of $BaTiO_3$ on $PrScO_3$, in Figure 1c, shows fully strained, coherent tensile strain in the film stabilizing an orthorhombic *aa*-phase with in-plane polarization along the [110] direction. $BaTiO_3$ on $LaLuO_3$ shows relaxation, seen in Figure 1d, from disagreeing $\mathbf{Q}_{para}$ vectors.

From θ-2θ scans, the out-of-plane lattice constant, *c*, was calculated using Bragg's Law from the (002) reflection while RSM signals afford both *c* and *a* lattice constants relative to the signal of the underlying substrate, plotted in Figure 2a, b. In Figure 2c, tetragonality, the ratio of *c* and *a*, reveals the evolution of the strained structure and realized relaxation of $BaTiO_3$ on La_2LuScO_6 and $LaLuO_3$, where the tetragonal phase is favored in-plane, since $a/c \approx c/a$ of bulk tetragonal $BaTiO_3$. Thus, relaxed thin-films on La_2LuScO_6 and $LaLuO_3$ exhibit in-plane polarization in the [100] and [010] directions. When tetragonality is greater than one, as in compressive strained films, out-of-plane polarization is enhanced along the [001], whereas, in tensile strained films, tetragonality is less than one, indicating in-plane polarization.

Domain Mapping and Manipulation. PFM was used to map domain polarization in nanoscale regions and selectively pole local regions upon application of an electric field. Vertical PFM verified *c*-domain formation in compressively strained films of $BaTiO_3$ on $GdScO_3$ and $SmScO_3$, supporting RSM findings. Selective manipulation of a compressively strained, 10 nm $BaTiO_3$ on $SmScO_3$ with a fully strained 6 nm $SrRuO_3$ Inner Back Electrode (IBE) depicts controllable switching, shown in Figure 3, where a 750-nm region was poled using an applied -3-Volt vertical bias to the area in a slow raster and mapped immediately thereafter.

Tensile strained orthorhombic in-plane polarized films with rectangular domains and DW along the [100] and [010] directions can be seen in $BaTiO_3$ on $PrScO_3$ and resemble others [4]. Remarkable out-of-plane local hysteretical switching using a 3-Volt bias waveform on a tensile strained 40 nm $BaTiO_3$ on $PrScO_3$, with an IBE as before, can be seen in Figure 4a, despite having in-plane domains, seen from lateral PFM amplitude response, in Figure 4b, and phase mapping, in Figure 4c. Local switching of the [110] polar axis to [001] shows controlled formation of a tetragonal *c*-domain from an orthorhombic *aa*-phase. Evidence of polarization manipulation using PFM depicts nanoferroelectric functionalities promoting future devices with the ability to controllably write and switch domains using electrical biases.

Acknowledgements:

Special thanks to my Principal Investigator, Darrell Schlom, and my mentor, Eric Langenberg, as well as PARADIM project funding under DMR-1539918 and NSF-1120296.

References:

[1] Schlom, et al., MRS Bull. 2014, 39 (2), 118-130.
[2] Choi, et al., Science 2004, 306 (5698), 1005-1009.
[3] Schlom, et al., Annu. Rev. Mater. Res. 2007, 37 (1), 589-626.
[4] Becher, et al., Nat. Nanotechnol. 2015, 10 (8), 661-665.

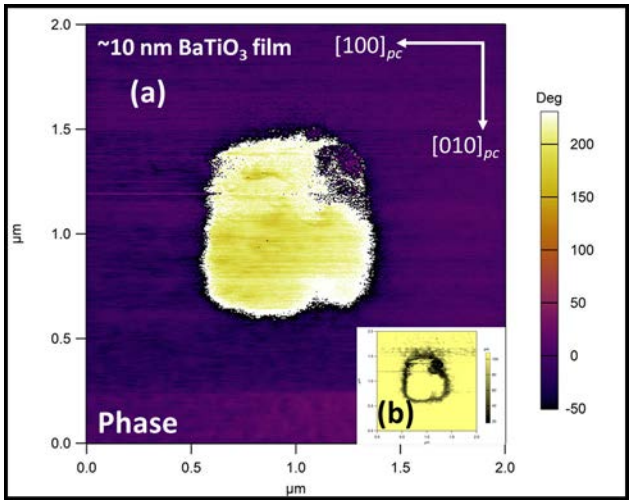

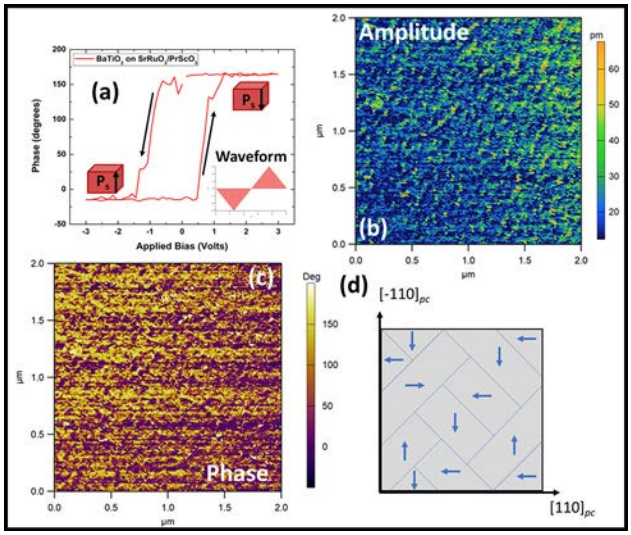

Figure 3, left: Locally poled $BaTiO_3$ thin-film, (a) and the written domain wall seen in PFM amplitude, (b). Figure 4, right: Out-of-plane hysteresis (a) of $BaTiO_3$ on $PrScO_3$, lateral PFM mapping amplitude response (b), the corresponding phase (c), and a derived model depicting truncated* aa*-domains with in-plane polarization (d).

Probing Single Crystal Growth Experimentally and through Computational Simulations

Heather Calcaterra

Chemical Engineering, University of Michigan Ann Arbor

REU Program: 2017 Johns Hopkins University Platform for the Accelerated Realization, Analysis, and Discovery of Interface Materials Research Experience for Undergraduates (JHU PARADIM REU) Program

JHU PARADIM REU Principal Investigator: Prof. Tyrel McQueen, Department of Chemistry, Department of Materials Science and Engineering, Department of Physics and Astronomy, The Johns Hopkins University

JHU PARADIM REU Mentors: Dr. W. Adam Phelan and Mekhola Sinha, Department of Chemistry, The Johns Hopkins University

Primary Source of PARADIM REU Funding: NSF Materials Innovation Platform Program, Grant # DMR-1539918

JHU PARADIM Tools Used: High pressure optical floating zone furnace, laser diode floating zone furnace, induction furnace

Contact: hcalc@umich.edu, mcqueen@jhu.edu, wphelan2@jhu.edu, msinha4@jhu.edu

Website: http://www.cnf.cornell.edu/cnf_2017reu.html

Abstract:

Advanced electronic, magnetic, and topological materials, such as semimetals, skyrmions, and topological insulators, have attracted significant interest for their predicted applications in quantum computing and information storage. To realize many of the necessary electronic and magnetic properties, these materials need be composed of only a single phase of matter arranged in a continuous, unbroken crystal lattice. This state, known as the single crystalline state, is non-trivial to synthesize in bulk.

One of the biggest challenges in single crystal growth is the low yield of the product, which can result from excessive vaporization and a surrounding dynamic fluid environment. To address this problem, we have created a computational model that simulates actual single crystal growth conditions employed in the laboratory. Furthermore, single crystal samples of proposed topological materials were grown within the laboratory through a variety of synthesis techniques and conditions, with aim to control the composition and yield of the final products. Herein, I present my methods and results in the synthesis, growth, and characterization of novel electronic and topological materials and bulk single crystals, both learned experimentally and through computational simulations.

Summary of Research:

During my REU internship, I have undertaken significant collaborations with various members in academia and industry in creating these novel materials.

In summary, several methods exist to create single crystal samples from bulk. Most apply heat to the polycrystalline sample in order to create a temperature gradient; the method of heating differs between samples. Common techniques include the Bridgman, laser diode floating zone, and high pressure floating zone growths. For the floating zone techniques, the material is melted via irradiation with light; for the Bridgman growth, an induction furnace with heating coils is used to heat the sample. We need to accurately choose the technique carefully to optimize the purity and yield.

When a polycrystalline sample is heated above its melting point, it is inevitable that some vaporization will occur. Depending on materials properties such as vapor pressure, the vaporization can be so significant as to greatly decrease the yield of the final product or even prevent proper melting and crystallization. This can be especially problematic at high pressures of the surrounding 'observer' supercritical fluid, as the solubility of the gas in the dynamic fluid environment will increase. Hence, we would like to find a way to minimize this vaporization.

We utilized COMSOL Multiphysics, a finite element differential equation solver, to investigate this phenomenon and decide what

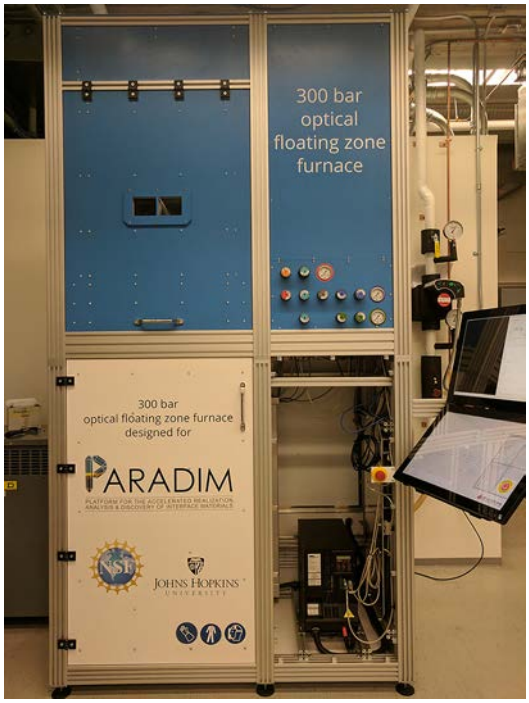

Figure 1: The high pressure floating zone furnace can be used to perform crystal growth under high pressures of inert gases, allowing the formation of materials not accessible under atmospheric pressures.

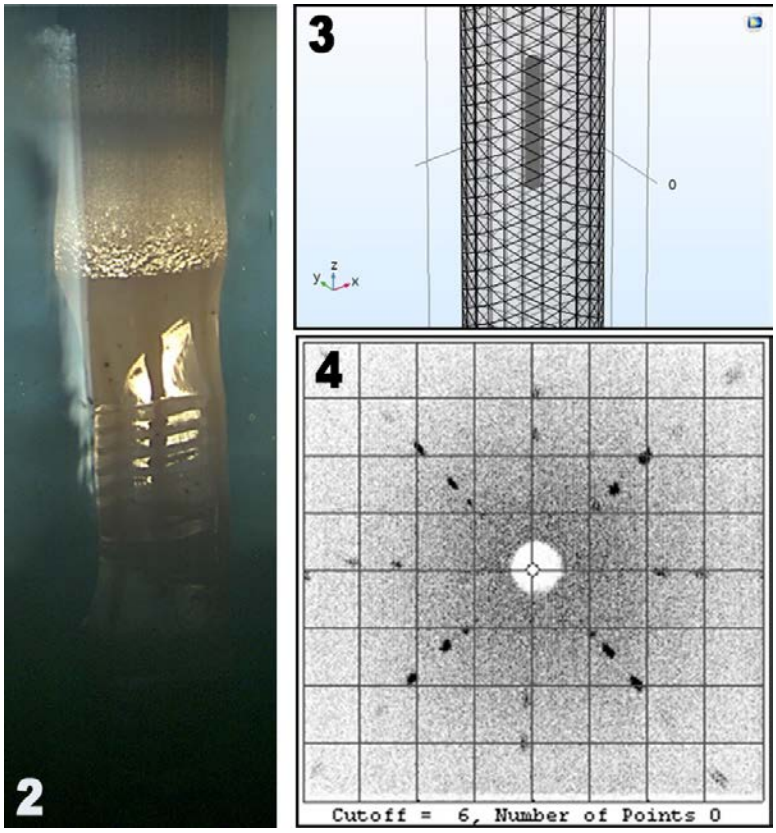

Figure 2, left: The crystal growth SmB_6, a material with predicted topological insulating character, is performed in the high pressure floating zone furnace. Figure 3, top right: Visual representation of the computational model created in COMSOL. The outer cylinder is the protective quartz container and the inner rod is the polycrystalline melt material. Figure 4, bottom right: Laue spots from the grown crystal show good symmetry, indicating the formation of a single crystal.

parameters might be ideal for crystal growth. We sought to investigate the effects of pressure, temperature gradient, and other materials-specific properties on the surrounding fluid environment in accordance with the Navier-Stokes Equations.

For our computational model, we measured dimensions that describe the laser diode floating zone furnace found in PARADIM. We defined the border of the simulation as being made of quartz, which is used as the protective shield in the furnace. The rod of polycrystalline material was created using average dimensions of an actual precursor rod, and we defined the rod properties as several different commonly grown species, such as silicon and titanium oxide. Finally, the simulation space with observer gas of either argon or oxygen, and the pressure exerted by these gases was changed sequentially.

Results and Conclusions:

We were able to model key parameters governing single crystal growth in the high pressure floating zone furnace and adjust them as needed. Difficulties in accurately defining the temperature gradient between the rod and the surrounding quartz tube prevented convergence of our simulation. This suggests to us that the complexity of the surroundings in growing single crystals is non-negligible and further studies must be conducted.

On the experimental end, it is important to ensure that our material is actually a single crystal after performing the melt. Crystallinity is determined by seeing how the material interacts with light, commonly using a technique called Laue diffraction. Symmetric spots show that the material satisfies Bragg's condition and the beam is parallel to a high-symmetry direction of the crystal, hence suggesting single crystallinity of a target material, SmB_6. However, in growing this material we had significant vaporization, solidifying the need for our working computational model.

Future Work:

During my REU, I have collaborated with users to plan, synthesize, and characterize single crystals such as the SmB_6 shown, using the materials by design method. These grown crystals have novel electronic and magnetic properties, such as topologically insulating character, which is helpful for next generation electronic devices and quantum computing.

However, there is still much work to do in minimizing vaporization and creating a more accurate simulation. In real experiments, there are often two rods, a seed and a feed rod, but only one rod was included in our simulation for simplicity. Furthermore, we described the observer gases as stationary. In the future, we would like to be able to simulate conditions for more complex electronic materials grown in PARADIM, such as SmB_6 that was grown experimentally. However, priority should be given to efforts in accurately describing the temperature gradient between the seed and feed rods and on ensuring the convergence of the Navier-Stokes equations used in the model.

Acknowledgements:

I thank NSF, PARADIM, and JHU for their funding. Additionally, I would like to thank Dr. W. Adam Phelan, Mekhola Sinha, Prof. Tyrel McQueen, and all the McQueen Lab members for their help.

References:

[1] W. Adam Phelan, Scientific Reports. 6, 20860 (2016).

Investigation of Atomic Layer Deposition for Distributed Bragg Reflectors

Jonathan Chandonait

Nanoscale Engineering, Colleges of Nanoscale Science and Engineering, SUNY Polytechnic Institute

REU Program: 2017 Cornell NanoScale Science & Technology Facility Research Experience for Undergraduates (CNF REU) Program

CNF REU Principal Investigator: Prof. Huili (Grace) Xing, Department of Electrical and Computer Engineering, Department of Materials Science and Engineering, Cornell University

CNF REU Mentor: Shyam Bharadwaj, Department of Electrical and Computer Engineering, Cornell University

Primary Source of CNF REU Funding: National Science Foundation via the National Nanotechnology Coordinated Infrastructure (NNCI) Grant No. ECCS-1542081

CNF Tools Used: AFM, SEM, Filmetrics, JA Woollam Ellipsometer, Oxford ALD, P7 profilometer, ICP-RIE

Contact: jchandonait@sunypoly.edu, grace.xing@cornell.edu, sb2347@cornell.edu

Website: http://www.cnf.cornell.edu/cnf_2017reu.html

Abstract:

Distributed Bragg reflectors (DBRs) have been proposed as a method for increasing the external quantum efficiency (EQE) of light emitting diodes (LEDs) in the UV-C wavelength range (200-270 nm). The DBR essentially works as a mirror, collecting photons emitted in the active region of the device and reflecting them to an area where they can be extracted from the device. DBRs can be fabricated using molecular beam epitaxy (MBE) using alternating layers of AlGaN with varied composition [1]. However, atomic layer deposition (ALD) provides an alternative with several possible advantages. ALD allows the growth of dielectric films which may improve the effectiveness of these DBRs [2]. ALD also allows easier access to a much broader range of materials thanks to the flexibility of the tools. Here, we discuss preliminary efforts to evaluate ALD as a method for the fabrication of DBRs.

Summary of Research:

In current UV-C LEDs, the external quantum efficiency, or the ratio of generated photons that leave the device to electrons passing through, is currently low due to absorption losses and total internal reflection within the device. Distributed Bragg reflectors have been proposed to mitigate these issues. By using periodic quarter wavelength layers with a high refractive contrast, a mirror stack can be created with very high reflectance (Figure 1). Therefore, a large majority of the photons that reach the mirror stack will be reflected out of the device, improving the EQE of the device.

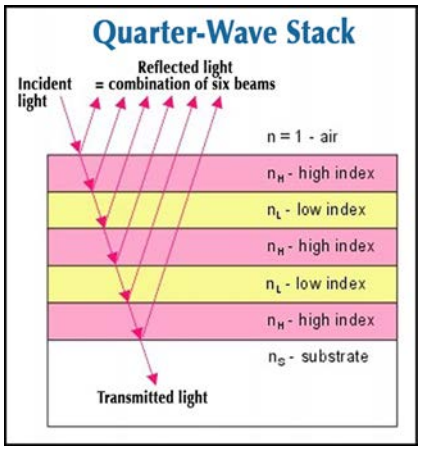

Figure 1: Shows the structure of a DBR and behavior of the photons that enter [3].

Currently there is little variety in the fabrication of DBRs for DUV LEDs. Most use MBE to grow varying compositions of AlGaN, although recently more groups have started to explore more possibilities. There are a few novel methods to change the formula, such as incorporating boron, but choices of materials are limited with MBE. Using ALD broadens the choice of materials, allowing us to take advantage of high-index contrast dielectrics, which could possibly increase the overall reflectance over a standard DBR.

Our goal was to investigate some of the advantages and obstacles involved with using ALD as a method for fabricating DBRs. In the future, the goal is to develop a dielectric mirror stack fabricated by ALD with a reflectance of > 99.9% in order to prove the viability of the method.

Results and Conclusions:

Three different ALD materials were examined for surface roughness. AFM was used to characterize the surface roughness of the deposition for each material. All three depositions were carried out using 300°C plasma ALD. Ta_2O_5 showed the best results (Figure 2), giving an RMS surface roughness of 0.1 nm. Al_2O_3 showed the next best surface roughness with an RMS of 0.7 nm. AlN showed the worst surface roughness with 1.0 nm RMS (Figure 3). Varying the deposition conditions such as growth temperature can affect these results. This shows that ALD is capable of depositing materials with ultrasmooth surfaces, which is important for achieving high reflectivity.

Figure 4 shows a graph of the transmission spectra of the basic substrate (Sapphire with AlN template) and depositions of Al_2O_3 and AlN with the substrate. The graph shows both films are reasonably transparent, which is essential for use in DBRs. The similarity of the two films with the substrate show that extinction is not a big issue. However, the graph also shows that the substrate itself is not very transparent, only transmitting approximately 40% of the light. This might suggest that a future possible step could be to remove the substrate through etching or lift off.

In studying growth rates between MBE and ALD, ALD demonstrates considerably slower growth rates at similar plasma powers. It is well known that ALD generally produces inferior crystal structure quality when compared to other growth methods, presenting a challenge if fabricating devices with ALD materials. However, ALD allows for atomically precise thickness control due to the monolayer nature of the process. This makes it possible to finely tune layer thicknesses to achieve complete constructive interference, which gives the highest possible measured peak reflectance.

Future Work:

There are still several factors that need to be explored to determine the viability of ALD as a method for fabrication of DBRs. The main problem that remains is the problem of crystallinity. With a typical epitaxial design consisting of the DBR being inserted between the substrate and the n-type semiconductor region, the low quality or amorphous crystal structures that are often produced by ALD can lead to defects later in the fabrication of the device. One way of getting around this problem would be to use different designs that move the mirror stack to a position in the device where it would have no effect on the structure of the rest of the device. Possible designs may include a dual-DBR stack, a flip-chip design, and several other possibilities.

Other future work will involve characterization of film strain as a possible concern. Also, the dielectric properties of ALD DBRs are an important factor to explore. Furthermore, using different profiles at layer interfaces in place of flat surfaces should be explored.

Finally, given the many possibilities that ALD offers, many other materials should be explored as options for fabricating DBRs.

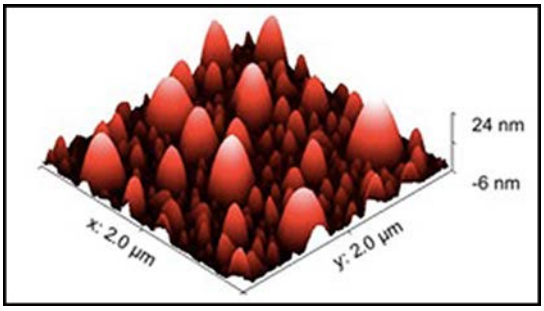

Figure 2: 3D AFM image of 35 nm AlN deposited on an AlN-on-sapphire template substrate. Shows undesirable rough surface.

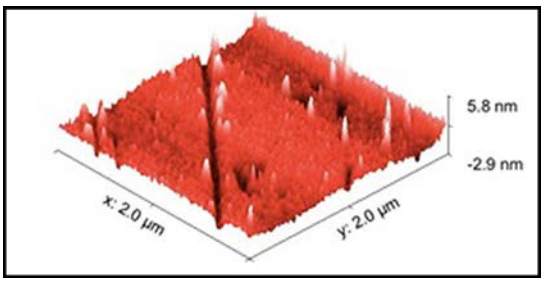

Figure 3: 3D AFM image of 35nm Ta_2O_5 deposited on an AlN-on-sapphire template substrate. Shows desirable smooth surface.

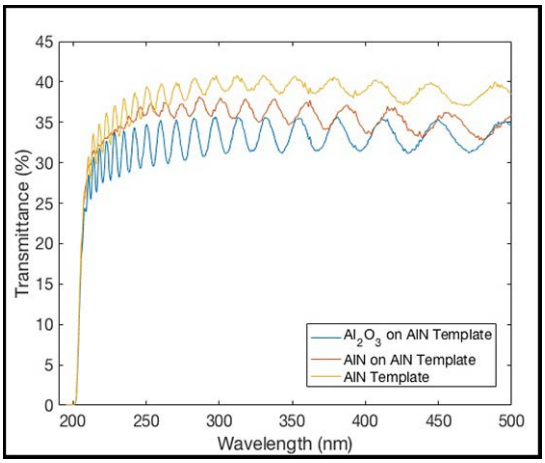

Figure 4: Graph showing the transmission spectra of our substrate, an Al_2O_3 ALD deposition, and an AlN ALD deposition.

Acknowledgements:

This work was funded by the NNCI NSF (grant no. ECCS-1532081). Special thanks to the Cornell NanoScale Science and Technology Facility and their staff for making this work possible. Also thanks to Prof. Grace Xing, Shyam Bharadwaj, and Dr. SM (Moudud) Islam for their help and support throughout the project. Finally, thank you to the NNCI for supporting the opportunity to present this research at the NNCI Convocation in Atlanta, GA.

References:

[1] Kneissl, M., and Rass J. (2016). "III-Nitride Ultraviolet Emitters". Springer Series in Materials Science.

[2] Triani, G., et al. (2005). "Atomic layer depostion of TiO_2/Al_2O_3 films for optical applications." SPIE Conference on Optics and Photonics.

[3] Zhong, Y., et al. (2015). "Arbitrarily-Wide-Band Dielectric Mirrors and Their Applications to SiGe Solar Cells." IEEE Photonics Journal, V7, #4, August 2015.

Synthesis of Core Substituted Napthalenediimides for n-Type Organic Semiconducting

Robert Chrostowski

Chemical Engineering, Texas A&M University

REU Program: 2017 Cornell NanoScale Science & Technology Facility International Research Experience for Undergraduates (CNF iREU) Program at the National Institute of Material Science (NIMS), Tsukuba, Ibaraki, Japan

CNF iREU Principal Investigator: Dr. Masayuki Takeuchi, Molecular Design and Function Group, National Institute for Materials Science, Japan

CNF iREU Mentor: Dr. Atsuro Takai, Molecular Design and Function Group, National Institute for Materials Science, Japan

Primary Source of CNF iREU Funding: National Science Foundation under Grant No. OISE #1559368

Contact: r.chrostowski@tamu.edu, takeuchi.masayuki@nims.go.jp, takai.atsuro@nims.go.jp

Website: http://www.cnf.cornell.edu/cnf_2017reu.html

Abstract:

The lack of stable high performance organic n-type semiconductors is a major challenge for the field. We explored one possibility for creating such a material by further augmenting previously successful *N,N'*-bis(cyclohexyl) napthalenediimide with a novel core extension. The synthesized mono- and bis-core-extended bis(cyclohexyl) napthalenediimides were given to a collaborating group to measure the compound's electronic properties.

Introduction:

Effective organic semiconductors are highly desirable in industry because organics, unlike silicon, are generally elastic and can be deposited with relatively simple solution chemistry techniques, thus allowing for flexible electronics devices and inexpensive roll to roll manufacturing. Semiconductor performance for thin film, field effect transistors is quantified through field effect mobility (FET), which is defined as the average charge carrier (hole or electron) drift velocity per unit electric field. Semiconductors can be considered high performance if they have a FET greater than that of amorphous silicon, which is 1 $cm^2 V^{-1} s^{-1}$.

One of the major challenges in the field of organic semiconductors today is the lack of n-type organic semiconductors that can match the performance of their p-type counterparts [1].

Previous research has demonstrated that the use of cyclohexyl imides dramatically improves the FET of naphthalenetetracarboxylic diimide (NDI), a widely studied and attractive organic n-type semiconductor candidate, to near 6 $cm^2 V^{-1} s^{-1}$ as compared to 0.16 $cm^2 V^{-1} s^{-1}$ for its straight chain hexyl counterpart [2], though issues with stability in air still remain [1]. Recently core substitution has emerged as a powerful tool to improve the stability and tune the electronic properties for NDIs [3]. Our lab has had previous success with core expansion using alkynyl groups [4].

Our research goal was to combine these results by synthesizing core-extended cyclohexyl NDIs.

Synthesis:

The synthetic scheme is outlined in Figure 1. For step one, a mixture of unsubstituted, monobromo-, and dibromo-1,4,5,8-naphthalenetetracarboxylic acid anhydride was reacted with cyclohexamine in acetic acid at reflux for one hour. After the reaction, the resultant precipitate was filtered through a Buchner funnel, washed with methanol and left to dry in the vacuum oven overnight. The dry precipitate was separated using silica gel liquid column chromatography with chloroform as the solvent. Fractions for unsubstituted, monobromo-, and dibromo- cyclohexyl NDI were collected separately.

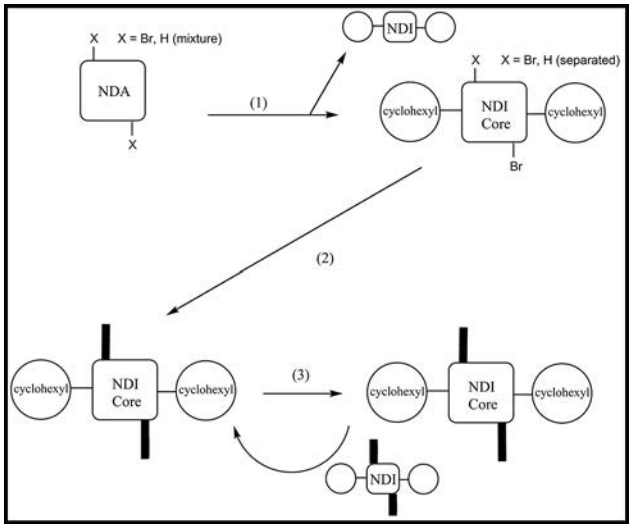

Figure 1: Synthetic scheme for achieving mono- and bis- core extended bis(cyclohexyl) napthalenediimides. (1) Imide Synthesis. (2) Sonogashira Coupling. (3) Deprotection.

For step two, the monobromo- and dibromo- fractions were each separately coupled with an alkynyl reagent with a protecting group through a palladium (II) bis(triphenylphosphine) dichloride and copper (I) iodide catalyzed Sonogashira coupling in dry and degassed tetrahydrofuran and diisopropylamine at 37°C for 16 hours. The product solution was filtered through sodium sulfate and celite. Solvent was removed with a rotary evaporator then the product was left to dry in the vacuum oven for two hours. The dry product was purified using silica gel liquid column chromatography with chloroform as the solvent.

Finally, for step three, the protection group was removed from the core extension moieties of the bis-core-extended fraction by using a deprotecting reagent. After the reaction, the organic solvent was evaporated with the rotary evaporator, and dried in the vacuum oven overnight. The dry product was purified twice using silica gel liquid column chromatography with chloroform as the solvent. Any fractions with the protecting groups still present were recycled. There was insufficient time to perform this step on the mono-core-extended fraction.

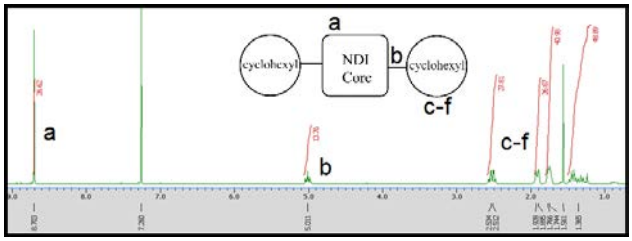

Figure 2: 1H NMR ($CDCl_3$, 400 MHz) spectrum of N,N'-*bis(cyclohexyl) napthalenediimide.*

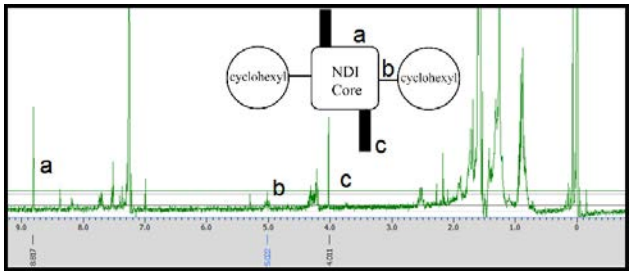

Figure 3: 1H NMR ($CDCl_3$, 400 MHz) spectrum of bis-core-extended N,N'*-bis(cyclohexyl) napthalenediimide. Full assignment impossible because impurity obscures aliphatic region.*

Results:

200 mg of unsubstituted cyclohexyl NDI were obtained as a byproduct from reaction step one to be used as a control. This product's ^1H nuclear magnetic resonance (NMR) in deuterium chloroform ($CDCl_3$) spectrum with peaks assigned is presented in Figure 2.

73 mg of bis-core-extended cyclohexyl NDI were synthesized. This product produced the expected peak in the mass spectrometer. This product's ^1H NMR in $CDCl_3$ spectrum, presented in Figure 3, has the expected aromatic (8.82 s 2H) peak, however the absence of the clear pattern visible in the aliphatic region of Figure 2 indicates the presence of impurities.

Additionally, 50 mg of protected bis-core-extended cyclohexyl NDI (^1H NMR in $CDCl_3$: 8.74 s 2H, 5.01 t 2H, 2.52 q 4H, 1.91 q 4H, 1.76 q 6H, 1.37 m 6H, 0.37 s 18H) and 40 mg of protected mono-core-extended cyclohexyl NDI (^1H NMR in $CDCl_3$: 8.69 m 3H, 5.01 t 2H, 2.52 q 4H, 1.91 q 4H, 1.76 q 6H, 1.37 m 6H, 0.37 s 9H) were synthesized, but did not have synthetic step three performed on them due to lack of time.

Future Work:

After performing synthetic step three on the mono substituted fraction and more thoroughly purifying both target compounds, the target compounds will need to have their presence further confirmed using ^{13}C NMR and have their crystal structure characterized through x-ray diffraction and atomic force microscopy. Collaborators will then measure the FET of organic thin film constructed with the target compounds and the unsubstituted control.

Acknowledgments:

I would like to thank my PI Dr. Masayuki Takeuchi, the tallest chemist in Japan, and my mentor Dr. Atsuro Takai, the coolest senior researcher to ever wear a Florida baseball cap. Special thanks goes to my bench mate Minghan Tan for teaching me through the entirety of my spill prone learning curve. I would also like to thank Dr. Lynn Rathbun, Dr. Nancy Healy, and all the other CNF iREU program staff for providing me with this wonderful opportunity. This research was supported by the National Science Foundation under Grant No. OISE 1559368.

References:

[1] Shan, B.; Miao, Q. Tetrahedron Lett. 2017, 58(20), 1903-1911.

[2] Shukla, D; Nelson, SF; Freeman, DC; Rajeswaran, M; Ahearn, WG; Meyer, DM; Carey, JT. Chem. Mater. 2008, 20(24), 7486-7491.

[3] Kobaisi, M. A.; Bhosale, S. V.; Latham, K.; Raynor, A. M.; Bhosale, S. V. Chem. Rev. 2016, 116, 11685-11796.

[4] Takai, A.; Takeuchi, M. submitted.

Compositional Analysis of Off-Stoichiometric Multiferroic $LuMnO_3$ and Electrode Nanopatterning of $(SrTiO_3)_n(BaTiO_3)_1SrO$ Thin Films

Kaynan Goldberg

Materials Science and Engineering, North Carolina State University

REU Program: 2017 Platform for the Accelerated Realization, Analysis, and Discovery of Interface Materials Research Experience for Undergraduates (PARADIM REU) Program

PARADIM REU Principal Investigator: Dr. Darrell Schlom, Materials Science and Engineering, Cornell University

PARADIM REU Mentors: Natalie Dawley and Rachel Steinhardt, Materials Science and Engineering, Cornell University

Primary Source of PARADIM REU Funding: NSF Materials Innovation Platform Program, Grant # DMR-1539918

Primary CNF Tools Used: Glen 1000 resist strip, Anatech resist strip, Manual resist spinners, ABM contact aligner, SC4500 odd-hour evaporator, Zeiss Supra SEM, Bruker energy-dispersive x-ray spectrometer (EDS)

Primary Cornell Center for Materials Research (CCMR) Tools Used: Asylum MFP-3D AFM

Contact: kmgoldbe@ncsu.edu, schlom@cornell.edu, nmd59@cornell.edu, rs963@cornell.edu

Website: http://www.cnf.cornell.edu/cnf_2017reu.html

Abstract:

Multiferroics are a class of materials that exhibit a combination of ferroelectricity, ferromagnetism, and ferroelasticity. $LuMnO_3$ is one such material with ferroelectric transition temperature of roughly 700 K and antiferromagnetic transition temperature of 90 K. Thin films of $LuMnO_3$ can be grown by molecular-beam epitaxy (MBE) to produce single crystal films with precise control over stoichiometry, $Lu_{1-x}MnO_3$, with up to 25% lutetium deficiency. Here, two $Lu_{1-x}MnO_3$ films with a composition gradient were explored. The films were characterized by atomic force microscopy (AFM) to identify the effects of lutetium deficiency on the surface morphologies, and by energy-dispersive x-ray spectroscopy (EDS) to quantify the surface composition gradient with a superimposed grid across the film. These measurements can be used to correlate ferroelectric and ferromagnetic properties with the observed composition gradient across each film. Additionally, nanoelectrodes were patterned on ferroelectric $(SrTiO_3)_n(BaTiO_3)_1SrO$ thin films.

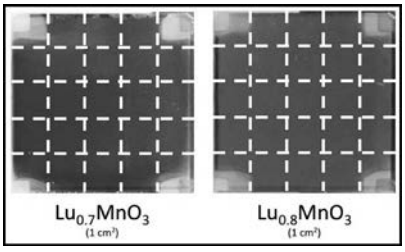

Figure 1: $Lu_{0.7}MnO_3$ on the left, $Lu_{0.8}MnO_3$ on the right, superimposed 5 × 5 grids dictating measurements.

Summary of Research:

Two projects were completed over the summer; characterization of off-stoichiometric lutetium-manganate ($Lu_{1-x}MnO_3$) thin films and patterning nanoelectrodes on strontium-barium titanate superlattice ($(SrTiO_3)_n(BaTiO_3)_1SrO$) thin films. Both materials were first grown using molecular-beam epitaxy (MBE) at Cornell by the REU intern's mentors.

Two $Lu_{1-x}MnO_3$ films were grown by mentor Steinhardt with a composition gradient across the plane of the film by providing Lu and Mn fluxes from opposing directions during growth. The intern characterized the surfaces of these films with energy-dispersive x-ray spectroscopy (EDS) on the Bruker EDS/Zeiss Supra SEM in the CNF and atomic force microscopy (AFM) using the Asylum MFP-3D in the CCMR. In Figure 1, the films are divided into 5 × 5 grids; measurements were performed within the regions dictated by these grids to map the gradient.

Six $(SrTiO_3)_n(BaTiO_3)_1SrO$ films were patterned with nanoelectrodes for capacitance measurements. First, a photolithography mask was created to measure in-plane and out-of-plane dielectric and ferroelectric properties by modifying an L-Edit file already made by mentor Dawley. The final design for this mask is shown in Figure 4a.

The process flow for the second project is outlined below.

- Sonicate samples in acetone, followed by IPA, for five minutes each.
- Rinse in DI water and blow dry.
- Run in Anatech asher on the "descum" program for one minute.
- Pipette one drop of AZ-nLOF 2020 resist to each corner of the sample for an even coating, and spin using 4000 RPM, 100 RPM/s ramp, 45 seconds.
- Bake at 115°C for one minute.
- Expose for 7.5 seconds using the mask in Figure 4a on the ABM contact aligner.
- Rinse the mask with acetone and IPA between exposures.
- Bake for one minute at 115°C.
- Develop in AZ-MIF 726 developer for one minute, gently agitating.

- Rinse in DI water and blow dry.
- Run in the Anatech asher on the "descum" program for one minute.
- Deposit 10 nm of Cr, followed by 100 nm Au by e-beam evaporation.
- The samples may be taped to the evaporation plate if none of the devices are covered up by tape.
- Place the samples in acetone for approximately two hours for liftoff. The excess resist and metal may not fully lift off during this time; if not, sonicate very briefly (15 seconds max) and quickly remove the samples from the acetone solution.
- Place in IPA for two minutes, rinse with DI water, and blow dry.

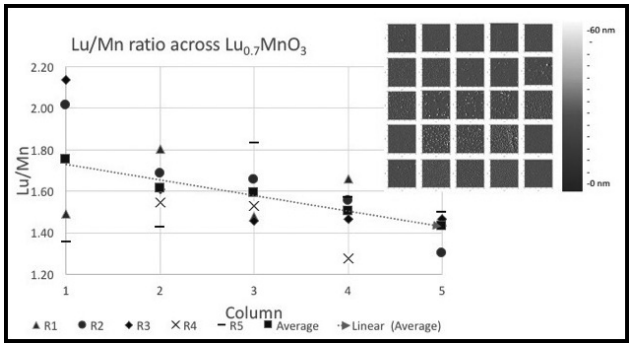

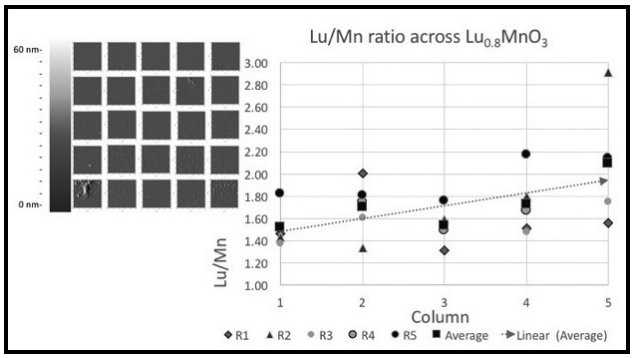

Figure 2, top: Ratio of Lu/Mn across $Lu_{0.7}MnO_3$ film across the surface of the film. Inset: 10 µm × 10 µm AFM images across the surface of the film. Figure 3, bottom: Ratio of Lu/Mn across $Lu_{0.8}MnO_3$ film across the surface of the film. Inset: 10 µm × 10 µm AFM images across the surface of the film.

Results:

Figures 2 and 3 show Lu/Mn ratios progressing across both films from left to right, in five rows, with insets showing the AFM images for each sample. Together, these two techniques show a trend of increasing surface roughness and "islands" with decreasing lutetium content. EDS does not register a chemical difference between these islands and the general surface.

Additionally, there is considerably more Lu on the surface than expected; roughly double the amount of Mn across the entire sample. Our hypothesis is excess Lu segregates to the growth surface during deposition.

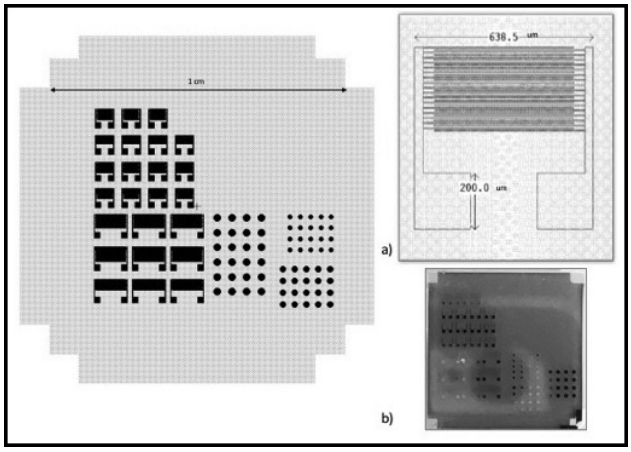

Figure 4: Patterned $(SrTiO_3)_n(BaTiO_3)_1SrO$ capacitive devices. Inset (a): L-Edit mask file. Inset (b): close-up of interdigitated electrode.

The results for the second project are the devices themselves, shown patterned on a sample in Figure 4.

Future Work:

The $LuMnO_3$ samples will undergo further elemental analysis via Rutherford backscattering spectroscopy. This will inspect the bulk composition while EDS is only surface sensitive. Once the composition of each sample is known, ferroelectric and ferromagnetic measurements may be taken which will be correlated to the compositions.

The electrodes on the $(SrTiO_3)_n(BaTiO_3)_1SrO$ samples will be used for capacitance measurements. The interdigitated electrodes (Figure 4b) will be used to measure in-plane capacitance by placing probes on the two terminating pads and applying a voltage across the electrode. The dots will be used to measure out-of-plane capacitance. The $(SrTiO_3)_n(BaTiO_3)_1SrO$ film will be partially removed to access the conductive $SrRuO_3$ layer beneath it. One probe will be placed on the bottom layer, and another probe on a dot, creating a capacitor with $(SrTiO_3)_n(BaTiO_3)_1SrO$ as the dielectric. A voltage will be applied across the two probes to measure capacitance through the film.

Acknowledgements:

Thank you to the CNF, Steve Kriske and CCMR, Julie Nucci and Melanie-Claire Mallison, my mentors and PI, the PARADIM REU community, and Cornell University for welcoming me this summer. Thank you to the NSF for funding, Grant # DMR-1539918.

References:

[1] L.W. Martin, R. Ramesh, "Multiferroic and magnetoelectric heterostructures," Acta Materialia, 60. 6-7, April 2012.

[2] D G Tomuta, S Ramakrishnan, G J Nieuwenhuys and JA Mydosh. "The magnetic susceptibility, specific heat and dielectric constant of hexagonal $YMnO_3$, $LuMnO_3$ and $ScMnO_3$." Journal of Physics: Condensed Matter, Volume 13, Number 20.

Electrical and Structural Characterization of Superconducting Ruthenate Ruddlesen-Popper Thin Films

Morgan Grandon
Chemistry, Truman State University

REU Program: 2017 Platform for the Accelerated Realization, Analysis, and Discovery of Interface Materials Research Experience for Undergraduates (PARADIM REU) Program
PARADIM REU Principal Investigator: Prof. Darrell Schlom, Materials Science and Engineering, Cornell University
PARADIM REU Mentor: Hari Nair, Materials Science and Engineering, Cornell University
Primary Source of PARADIM REU Funding: NSF Materials Innovation Platform Program, Grant # DMR-1539918
Contact: mlg2668@truman.edu, schlom@cornell.edu, hn277@cornell.edu
Website: http://www.cnf.cornell.edu/cnf_2017reu.html

Abstract:

Strontium ruthenate (Sr_2RuO_4) is the only known example of a spin-triplet superconductor. This exotic spin-triplet pairing allows for the possibility of using Sr_2RuO_4 for ground-state quantum computing. However, for practical applications it is essential to fabricate epitaxial thin films of Sr_2RuO_4. Moreover, thin films could potentially provide a route for enhancing the T_c through strain engineering. Indeed, uniaxial strain studies on Sr_2RuO_4 single crystals indicate that T_c can be enhanced from 1.4 K up to 3.4 K. Thin films of Sr_2RuO_4 were grown using molecular beam epitaxy (MBE). Films were characterized structurally using x-ray diffraction (XRD) to ensure phase purity. Four-point probe resistivity measurements were carried out in order to optimize the MBE growth parameters. Films grown under these optimized conditions had low residual resistivities on the order of 4.0 μΩ·cm and were superconducting with a T_c ~ 0.8 K. To date these are the only superconducting Sr_2RuO_4 thin films grown using MBE.

Summary of Research:

Sr_2RuO_4 is a layered perovskite oxide with a spin-triplet superconducting state [1]. This superconducting ground state, in which the Cooper pairs of the material can occupy three quantum states, allows for Sr_2RuO_4 to be a potential material for the realization of quantum computing. To use Sr_2RuO_4 in quantum computers, however, requires the fabrication of epitaxial thin films and the enhancement of the T_c. In order to achieve superconductivity in this material, the disorder of the film must be minimized. Prior to our work, only two examples of a superconducting thin film had been reported. These films were both grown by pulsed laser deposition and showed superconductivity, with the better of the two films having a T_c of 0.9 K [2,3].

Enhancement of T_c in bulk crystals has been demonstrated through the application of uniaxial strain. Under a uniaxial compressive strain of -0.6%, the T_c of a Sr_2RuO_4 crystal was increased from 1.4 K up to 3.4 K [4].

In thin films, strain can be built into the crystal through the use of epitaxy. Using molecular beam epitaxy, we can grow both tensile and compressive strained thin films, as the crystal lattice of the film elastically deforms to match the crystal lattice of the substrate upon which it the film is grown.

This summer, our research focused on growing on $NdGaO_3$ (NGO), a substrate with a smaller crystal lattice than Sr_2RuO_4. This introduced a compressive strain of 0.1 % in one direction and 0.3 % in the other.

To determine the proper growth parameters to achieve superconductivity in the film, we used a cyclical optimization scheme. Films were grown using MBE, then temperature dependent resistivity measured using a four-point probe measurement and finally structural characterization was done using XRD. Based on the results of these measurements, alterations in growth parameters, such as strontium/ruthenium flux ratio, substrate temperature, and oxidizer pressure were modified as necessary and the scheme was repeated.

Results and Conclusions:

θ-2θ XRD scans were conducted to ensure phase purity of the Sr_2RuO_4 films. An example is shown in Figure 1. The presence of five film Bragg peaks, all indexed to Sr_2RuO_4, in the diffraction pattern is indicative of a phase pure film. Presence of Kiessig fringes indicate good crystallinity and smooth interface between film and substrate.

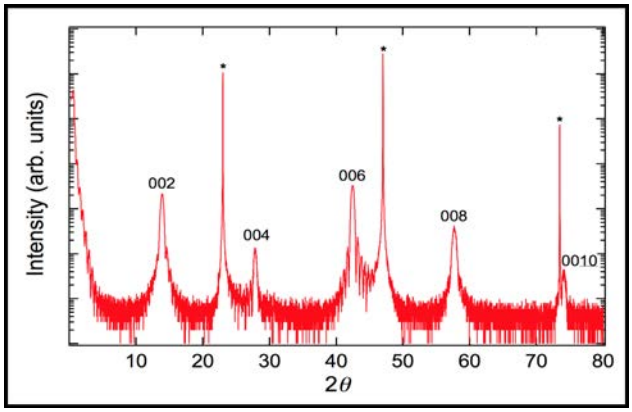

Figure 1: θ-2θ x-ray diffraction pattern of the Sr_2RuO_4 film with asterisks denoting the substrate peaks.

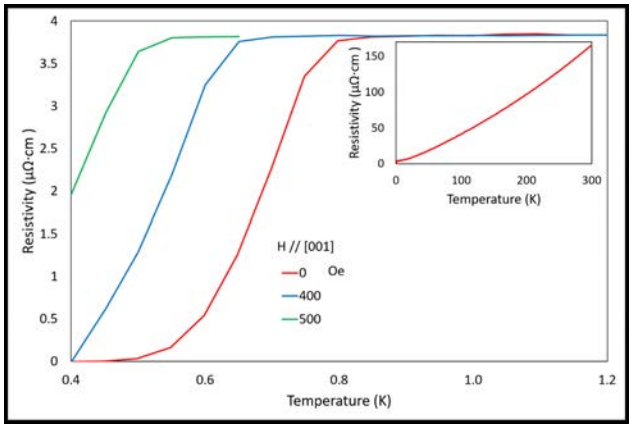

Figure 2: Resistivity as a function of temperature (<1.2 K) under various magnetic fields applied parallel to the c-axis of the film. Inset shows resistivity as a function of temperature up to room temperature.

To characterize the disorder of the film, resistivity versus temperature measurements were taken between 300 K and 4 K using a four-point probe with standard van der Pauw geometry [5]. Disorder is minimized when residual resistivity at low temperature (4 K) is small (< 4.0 μΩ.•cm) and residual resistivity ratio (RRR) is large (> 40). Films with low residual resistivity were measured down to 0.4 K using an in-line probe geometry on a Quantum Design Physical Property Measurement System. Superconductivity over the bulk of the sample was observed in multiple films with a $T_c \sim$ 0.8 K. Application of a magnetic field, which suppresses the T_c of the sample, provides further support of superconductivity.

In conclusion, cyclical modification and characterization of films allowed for determination of the optimal parameters for the growth of superconducting Sr_2RuO_4 thin films on NGO using MBE and better knowledge of the growth space of Sr_2RuO_4.

Future Work:

In continuing this work, the Schlom group will be conducting further magnetic field dependence studies on the samples that have already demonstrated superconductivity. The enhanced knowledge of the growth space will be used to grow Sr_2RuO_4 films on different substrates, therefore altering the strain state. This will allow for studies on the dependence of T_c on epitaxial strain.

Acknowledgements:

I would like to especially thank my mentors, Hari Nair and Jacob Ruf, as well as my principal investigator, Prof. Darrell Schlom. I would also like to acknowledge support from grants DMR-1539918, DMR-1120296, and GBMF3850.

References:

[1] Maeno, Y.; et al. Nature 1994, 372, 532-534.

[2] Krockenberger, Y.; et al. Appl. Phys. Lett. 2010, 97 (8), 82502.

[3] MacManus-Driscoll, J.; et al. Supercond. Sci. Technol. 2016, 29 (9), 1-6.

[4] Steppke, A.; et al. Science (80). 2017, 355 (6321), 9398.

[5] Tegenkamp, C.; et al. JPCM, 2015, 27 (22), 223201.

Bacterial Mechanics on a Chip

Gabriel Guisado

Biomedical Engineering, University of Rochester

REU Program: 2017 Cornell NanoScale Science & Technology Facility
Research Experience for Undergraduates (CNF REU) Program

CNF REU Principal Investigator: Prof. Christopher Hernandez, Meinig School of Biomedical Engineering and Sibley School of Mechanical and Aerospace Engineering, Cornell University

CNF REU Mentor: Melanie Roberts, Meinig School of Biomedical Engineering and Sibley School of Mechanical and Aerospace Engineering, Cornell University

Primary Sources of CNF REU Funding: National Science Foundation via the National Nanotechnology Coordinated Infrastructure (NNCI) Grant No. ECCS-1542081; NSF Grant CMMI-1463084

CNF Tools Used: Heidelberg DWL 2000, Gamma, ASML, Oxford 80s and 100, Trion, MOS Furnaces, Versalaser, AJA, AFM, SEM, Profilometer P10

Contact: gguisado@u.rochester.edu, cjh275@cornell.edu, mfr75@cornell.edu

Website: http://www.cnf.cornell.edu/cnf_2017reu.html

Abstract:

The ability of bacteria to squeeze into constrictions a fraction of their size can lead to bacterial infections such as osteomyelitis. In osteomyelitis, bacteria cells squeeze into small channels in the bone where they are protected from immune cells and become much more difficult to treat with antibiotics. To simulate the mechanical loading conditions bacteria experience as they move through sub-micron channels, bacteria were analyzed in similarly sized tapered channels through the fabrication of a microfluidic device. The sub-micron channels were created using deep ultraviolet (DUV) photolithography in the CNF, and then etched to transfer the design to a fused silica device. The design includes an inlet of approximately 1.2 µm, an outlet of 250 nm, and is 75 µm long. The bacteria trapped in the channels are imaged with both traditional and super-resolution microscopy. The distance travelled is then measured and compared to the pressure drop experienced by the bacteria in the channels. This pressure drop is defined as the difference in pressure across the bacteria trapped in the channel. Data collected this summer revealed that under a high inlet pressure, the bacteria can go into a channel width a fraction of their size. At a low inlet pressure, the bacteria will not squeeze into a constriction less than half their diameter. However, with the introduction of a large pressure drop, the bacteria can squeeze into a constriction up to a quarter of their diameter (Figure 1).

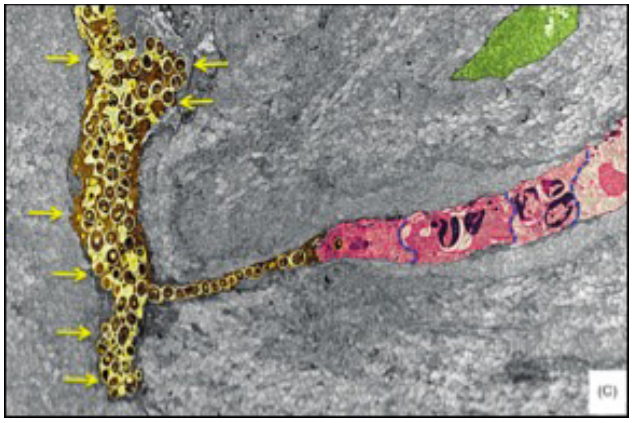

Figure 1: MRSA (yellow) penetrating bone (gray) to point where immune cells (pink) can't reach the MRSA (Nishitani, et al. 2016).

Summary of Research:

Extrusion loading is the loading mechanism the lab refers to as the mechanical stimuli that *E. coli* undergo when in the designed tapered channels. Extrusion loading is unique among methods of mechanically stimulating bacteria in that it achieves a non-uniform stress and strain experienced by the bacteria.

Manufacturing the microfluidic device begins with a CAD design (Figure 2). The channels in the design are tapered, ranging from an inlet width of 1.2 µm and an outlet width of 250 nm. The design is created so there would be varying pressure drops across each channel. This varying pressure drop is because of a resistance to fluid flow in the bypass (Figure 3). There is a decline in

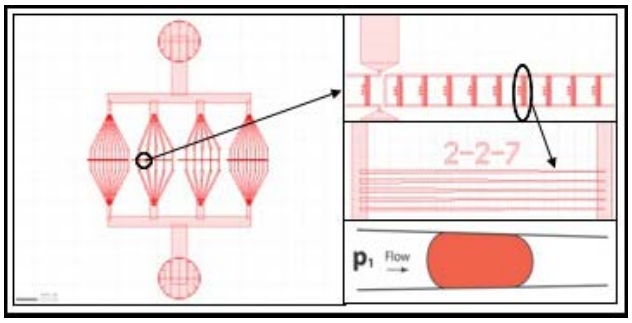

Figure 2: The tapered channels used to trap bacteria have a 1.2 µm inlet, a 250 nm outlet, and are 75 µm long. Multiple tapered channels are on each device. Six devices are present on each wafer.

pressure as the fluid moves through the channels, giving every channel its own distinct upstream pressure. The device uses 600 different channels so that several different pressure drops can be examined at once.

The silica glass device is created with DUV lithography. Fused silica was chosen because it is much stiffer than the bacteria and its transparency allows for microscopy. SEM, AFM, and the profilometer are used to check for proper taper geometry, outlet width, channel depth and to allow optimization of the process in subsequent application. After characterization, the device is bonded to a thin (170 nm) silica wafer and ready for experimentation. The device is placed on the microscope stage and bacteria in liquid suspension are flowed into the inlet using a syringe pump with a pressure gage reporting pressure at the inlet.

Experiments are performed at inlet pressures of 25 kPa and 60 kPa. Using a syringe pump that controls flow rate, the bacteria in M9 media are transported into the device. A pressure sensor is connected to the tube and a computer so that the pressure can be monitored and controlled based on the flow rate of the syringe pump.

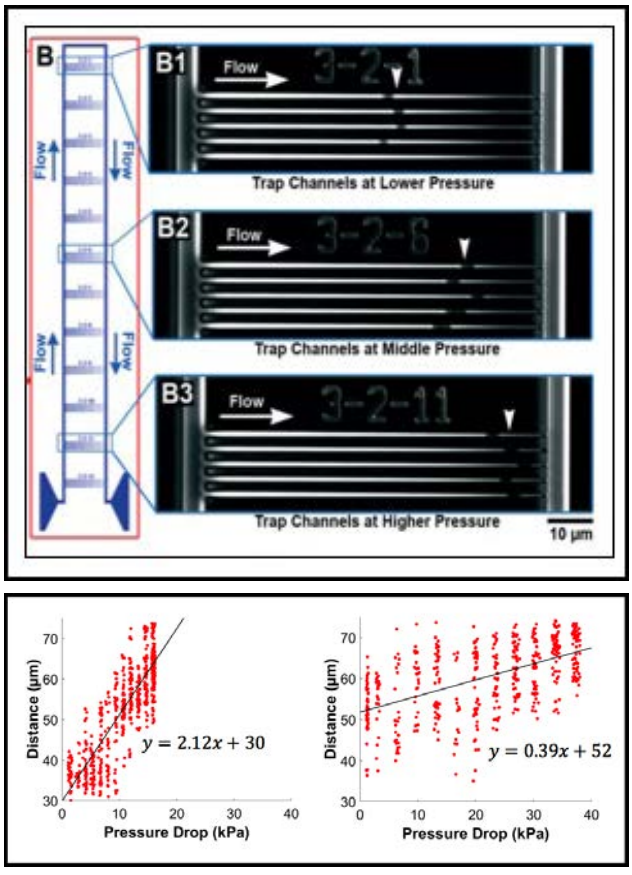

Figure 3, top: Tapers are placed in sets of five separated by a distance. Each set of tapers experiences a different drop in pressure across its length. This pressure drop is determined by the difference between upstream and downstream pressure (Sun et al Lab Chip 2014). Figure 4, below: Shown here are over 1000 analyzed cells. The relationship between pressure drop across the channel and penetration of the bacteria differs between an external pressure of 25kPa (left) and an external pressure of 60 kPa (right).

Images of the bacteria in the tapered channels are collected using transmission microscopy and the distance traveled by the bacteria was determined. The pressure drop across each bacterium in a tapered channel is determined using hydraulic circuit calculations. The distance traveled by bacteria is determined using the channel's number labels as a positional marker in the experimental images. The results indicate the relationship between loading conditions and how far the bacteria travel.

Results and Conclusions:

Over 1000 cells from over 20 different experiments were analyzed. Experiments were performed at both 60 kPa and 25 kPa inlet pressure. At a 60 kPa inlet pressure, the regression line shows an intercept of 52 µm traveled (75 µm channel length), and an average width of 500 µm under a 1 kPa pressure drop; R^2 = 0.39. At a 25 kPa inlet pressure, the regression line shows an intercept of an average of 30 µm traveled; R^2 = 0.71. In regards to reaching max constriction (250-300 nm) in the channels, this can be done in the 60 kPa experiments at approximately 6 kPa pressure drop, while it takes at least double that in the 25 kPa conditions.

It was previously undetermined whether in the 25 kPa experiments the bacteria would be able to reach the end of the channels where it is under the max constriction. Therefore, these findings present the lab with new information regarding loading conditions that enable bacteria to squeeze deep into these channels (Figure 4).

Future Work:

Future work would be to conduct a similar experiment, but with bacteria known to cause infections, such as *Staphylococcus aureus*. Since this strain of bacteria has a higher safety level than the *E. coli* used, the study would have to be moved to a different lab facility. As more of a long-term goal, we want to find out what component or components of bacteria play the biggest role in how they are able to squeeze into these sub-micron channels. Finding the biological pathways in which bacteria squeeze into these sub-micron channels could eventually lead to better antibiotics for treating bacterial infections.

Acknowledgements:

NSF grant no. ECCS-1542081, NSF Grant no. CMMI-1463084, NNCI, CNF REU Program Coordinators and Staff. Thank you to Professor Christopher Hernandez and Melanie Roberts for affording me this opportunity, and the Peng Cheng Group for collaborating on this study.

Multi-Functional Platform for Characterization of Nanostructured Polymer Brushes

Michael E. Klaczko

Chemistry, SUNY College of Environmental Science and Forestry

REU Program: 2017 Cornell NanoScale Science & Technology Facility Research Experience for Undergraduates (CNF REU) Program

CNF REU Principal Investigator: Dr. Christopher Ober, Materials Science and Engineering, Cornell University

CNF REU Mentor: Wei-Liang Chen, School of Chemical and Biomolecular Engineering, Cornell University

Primary Source of CNF REU Funding: National Science Foundation via the National Nanotechnology Coordinated Infrastructure (NNCI) Grant No. ECCS-1542081

Primary CNF Tools Used: AJA sputter, Hamatech, Oxford PECVD, Gamma Developer, ASML stepper, AFM, SEM, Oxford 81 and 100, Trion Etcher

Contact: mklaczko@syr.edu, christopher.ober@cornell.edu, wc497@cornell.edu

Website: http://www.cnf.cornell.edu/cnf_2017reu.html

Abstract:

Polymer brushes have been of interest because of their unique ability to act as a functional coating. The unique structure of polymer brushes allows them to be used for several applications including antifouling, cell adhesion, resistance to nonspecific binding, and biosensing. With the realized applications of polymer brushes, it has become more important to understand their fundamental structure and the resultant stimuli-responsive behavior. This project aims to create a way to observe the polymer brushes at the molecular level by putting polymer brushes onto the sidewalls of diffraction gratings. Once successful, completed observation can be done on the macro scale by observing the diffraction of light through the gratings, and on the molecular scale by observing the scattering of neutron beams across the sides of the diffraction gratings. These measurements are exemplified in Figure 1. By successfully utilizing photolithography and subsequent multiple etching steps pattern transfer on a sandwich structure to create our multi-functional platform, the base platform has been created and the process to reaching this goal has been furthered.

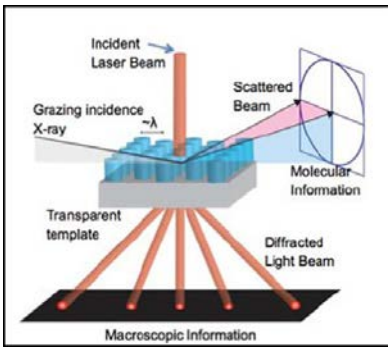

Figure 1: Diagram showing how laser diffraction and neutron beam scattering can be used to gain macroscopic and microscopic information on the polymer brushes grown on the multi-functional platform.

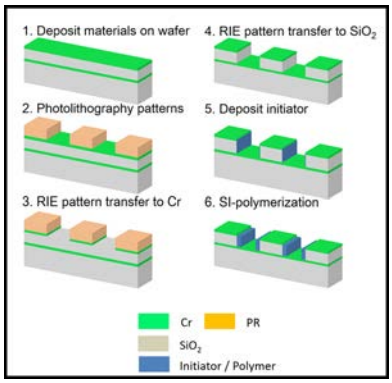

Figure 2: Wafer development process to create the multi-functional platform.

Summary of Research:

The focus of this summer's research was on developing a multi-functional platform which could be used to characterize nanostructured polymer brushes. As shown in Figure 2, this was done by developing a sandwich structure on top of a fused silica wafer that could be manipulated through photolithography and etching to create a structure, which only had silicon dioxide exposed on the sidewalls of the structure. Since the small molecule initiator, which is for the polymerization of polymer brushes, can only bind to hydroxyl groups, it will only bind to the sidewalls that have exposed silanol groups. This in turn creates a structure which only has polymer brushes on its sidewalls after polymerization. The structure was characterized with atomic force microscopy (AFM), scanning electron microscopy (SEM), and laser diffraction. These characterization techniques were also used throughout the fabrication process to correct problems along the way and to determine whether the process was being completed successfully.

Results and Conclusions:

In the end, this process was completed successfully as determined using AFM, SEM, and laser diffraction. The multi-functional structure was made so that a diffraction grating was created. As shown in Figure 3a and 3b, this structure was proven after a beam of green laser light with 532 nm was diffracted when shown through the

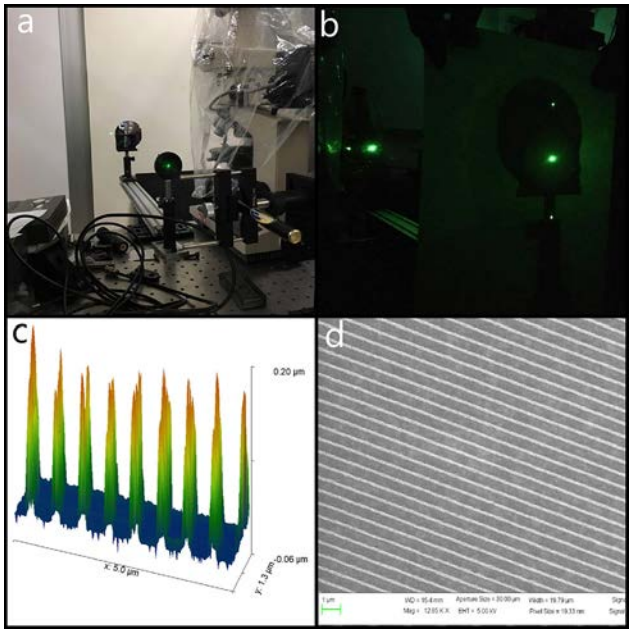

Figure 3: a) the laser diffraction setup b) a laser being diffracted by the final structure of the multi-functional platform c) An AFM image of the pattern on the final structure form d) An SEM image of the pattern on the final structure form.

pattern. Figure 3c and 3d further support this conclusion by showing the diffraction grating through their imaging process. During the creation of the platform it was found that layer uniformity, layer cleanliness, wafer flatness, and ARC/Resist type and coating were all very important to the success of the structure. After completing the process, it was determined that layer uniformity and wafer flatness both worked together to counteract the advances made in photolithography. With a high numerical aperture, it was necessary for the overall shape of the wafer to be very homogeneous and uniform. To fix this, the numerical aperture was lowered and the chromium was coated with a plasma bias which made deposition denser and more uniform. The problem of layer cleanliness was fixed by cleaning and seasoning the chamber of the Oxford plasma enhanced vapor deposition (PECVD) before depositing the silicon dioxide onto the wafer, and by cleaning the wafer before each layer deposition with a hot piranha clean. After trying both negative and positive resists and several types of anti-reflective coatings (ARC), the resist UV210-0.6 was used with the ARC DUV-42P.

The successful completion of this project now allows for a more comprehensive observation and understanding of polymer brushes to be reached which would have never been reached had such a platform never been created. Figure 4 shows what the completed structure looks like.

Future Work:

Using this multi-functional platform, experiments can now be done which isolate the polymer brushes to the sidewalls of the structure which will ultimately enhance our knowledge of polymer brushes and how they work. Initiator will be deposited onto the structure and if it only attaches to the sidewalls like it is supposed to, polymer brushes will be grown here and laser diffraction as well as neutron beam scattering experiments will be able to be done on them. If it is found that the initiator does not only bind to the sidewalls but other areas as well, then the structure will be re-evaluated and recreated in a way that allows us to achieve this structure with silicon dioxide only exposed on the sidewalls. Using laser diffraction and neutron beam scattering information, the study of several different types of polymer brushes can be completed. From the greater understanding of polymer brushes given by these studies, research can be done on applying polymer brushes to their realized applications and to developing new ways that they could be used.

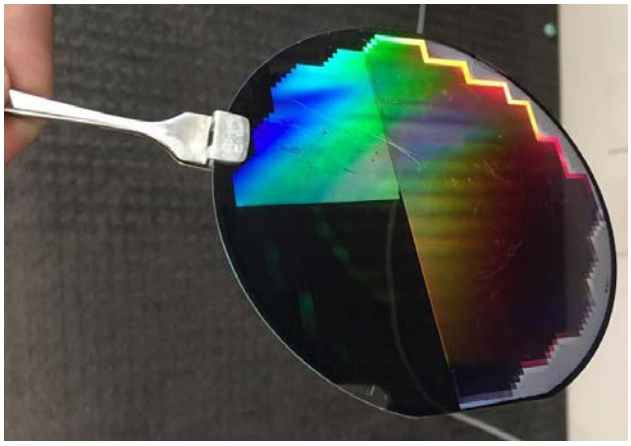

Figure 4: The multi-functional platform after its process completion. Differences in chrome etch time were measured on this wafer but the top half portion is where the pattern was successfully developed and processed.

Acknowledgements:

I would like to thank Dr. Christopher Ober for allowing me to work in his research group this summer, my mentor Wei-Liang Chen for guiding through the field of nanotechnology and providing the support for my success in this program, Melanie-Claire Mallison for creating such a welcoming and loving environment, and the staff at CNF for all their expert help and support. I would also like to thank my peers in the REU program for their support throughout the program, and for their continued support moving forward. Funding was provided by NSF via the NNCI Grant No. ECCS-1542081.

References:

[1] W-L. Chen, R. Cordero, H. Tran, and C. K. Ober. 50th Anniversary Perspective: Polymer Brushes: Novel Surfaces for Future Materials. Macromolecules 2017 50 (11), 4089-4113.

[2] Swann, J. M. G.; Bras, W.; Howse, J. R.; Topham, P. D.; Ryan, A. J. Quantifying Hydrogel Response Using Laser Light Scattering. Soft Matter 2010, 6 (4), 743-749.

High Concentration Supporting Electrolytes for Enabling Stable Zinc Electrodeposition

Jadiel López González
Chemical Engineering, University of Puerto Rico, Mayagüez Campus

REU Program: 2017 Keeping the Ezra Promise Research Experience for Undergraduates (KEP REU) Program
KEP REU Principal Investigator: Prof. Lynden A. Archer, Chemical and Biomolecular Engineering, Cornell University
KEP REU Mentor: Snehashis Choudhury, Chemical and Biomolecular Engineering, Cornell University
Primary Source of KEP REU Funding: Keeping the Ezra Promise (KEP), Robert Frederick Smith School of Chemical and Biomolecular Engineering, Cornell University
Contact: jadiel.lopez@upr.edu, laa25@cornell.edu, sc2563@cornell.edu
Website: http://www.cnf.cornell.edu/cnf_2017reu.html

Abstract:

Zinc metal is an excellent choice for metal based secondary batteries not only because of its high abundance and low toxicity, but also due to its high anodic redox potential and energy density when compared with cells that use nickel and lead anodes. Furthermore, aqueous electrolytes can be used, thus minimizing the risk of thermal runaway or explosion. A common problem faced in such batteries is the formation of dendrites, needle-like structures, which can pierce separators and produce sudden short circuits. In this work, the electrodeposition of zinc metal was visualized using an in-house built electrochemical setup with a base electrolyte of zinc sulfate heptahydrate ($ZnSO_4 \cdot 7H_2O$) dissolved in water. Results discussed in this report show that aqueous electrolytes containing higher concentrations of zinc salts and zinc cells operated at lower current densities exhibit significant less tendency to dendrite formation. Additionally, an enhanced stability at a current density as high as 1000 mA/cm^2 was obtained using high concentration of zinc sulfate solutions and sodium-salts as supporting electrolytes.

Summary of Research:

Zinc metal batteries are in development as a new generation of battery systems which can achieve high energy densities to power full electric vehicles [1]. Zinc metal is an excellent choice for the anode in secondary batteries not only because of its high natural abundance and low toxicity, but also due to its high anodic redox potential and energy density when compared with the commonly used nickel and lead anodes [2]. Furthermore, because the cells can be operated in aqueous electrolytes, this minimizes the risk of thermal runaway or fires. A common problem faced in such batteries is the formation of dendrites, needle-like structures, which can pierce separators and produce sudden short circuits [1,2].

The purpose of this project was to investigate how conditions in the electrolyte influence dendrite formation during zinc electrodeposition. Electrolyte salt concentration, current density and a secondary/supporting electrolyte salt additive were studied in order to determine their respective relationship with dendrite formation. Electrodeposition was visualized in an in-house built electrochemical cell which consisted of a glass slide, zinc metal (99.994%, Alfa Aesar), which acted as the electrodes, and copper strips. The electrode separation distance of each cell was maintained constant at 1 cm apart. Each electrodeposition experiment was filmed for one hour under an optical microscope (Olympus BX51) at a constant current density. Each electrolyte solution was prepared using zinc sulfate heptahydrate, $ZnSO_4 \cdot 7H_2O$ (J.T. Baker), and sodium sulfate, Na_2SO_4 (Macron Fine Chemicals), dissolved in deionized water at different molarities. Impedance spectroscopy was also done in order to calculate the conductivity and interface resistivity of each electrolyte solution.

Results and Conclusions:

The effect of concentration, current density and the use of a secondary salt additive were studied in order to assess their respective influence on Zn dendrite formation. As shown in Figures 1 and 2, using higher concentrations of zinc salts in the electrolyte solution limits dendrite formation significantly. Also using lower current densities and sodium sulfate as a secondary salt additive have the same effect as well. As shown in Figure 3, a stable electrodeposition was obtained using a current density as high as 1000 mA/cm^2. This was done using a mix electrolyte solution of zinc sulfate heptahydrate at 1.70M and sodium sulfate at 0.80M.

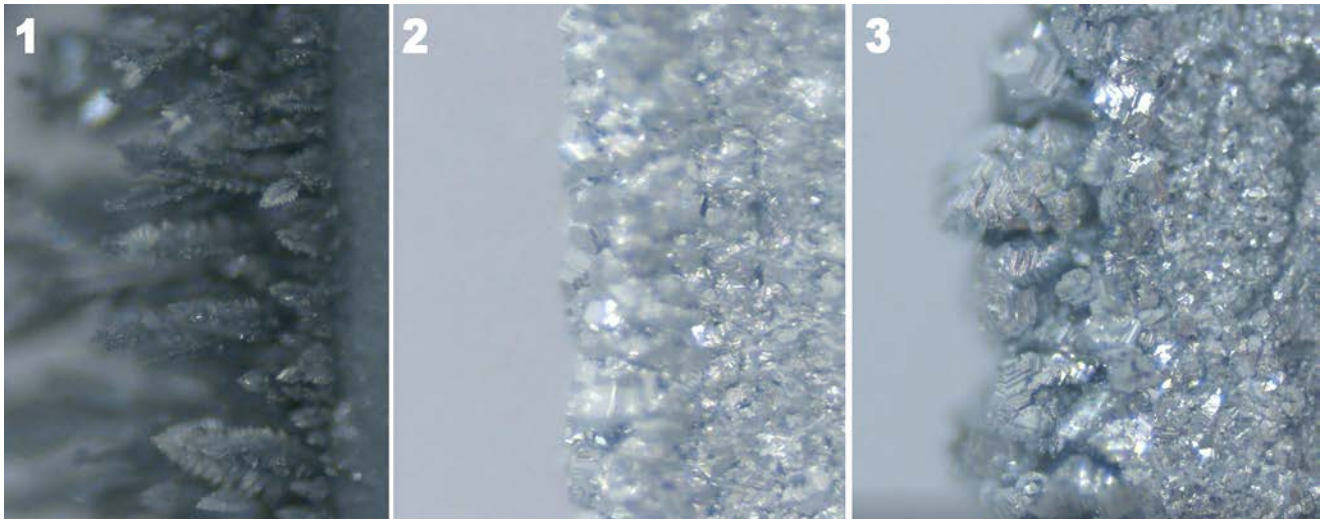

Figure 1, left: Electrodeposition of zinc sulfate heptahydrate at a concentration of 0.10M and a current density of 400 mA/cm^2 after one hour. Figure 2, middle: Electrodeposition of zinc sulfate heptahydrate at a concentration of 2.00M and a current density of 400 mA/cm^2 after one hour. Figure 3, right: Electrodeposition of a mix electrolyte solution of zinc sulfate heptahydrate at a concentration of 1.70M and sodium sulfate at a concentration of 0.80M at a current density of 1000 mA/cm^2 after one hour.

As a result of zinc achieving a stable deposition at a current density of 1000 mA/cm^2, indicates that zinc metal batteries are an excellent choice for further development to increase energy density, battery life and increase further applications.

Impedance spectroscopy was used to characterize the effect of the salts on ion transport in bulk electrolytes and at the interfaces between electrodes and electrolytes. Electrolyte concentration displays a linear effect on conductivity, where higher concentrations showed higher conductivity, as shown on Figure 4.

On the contrary, using higher concentrations of zinc have a tendency of increasing interfacial resistance. Also, the interfacial resistance using the supporting electrolyte had the same tendency as before, where higher concentrations showed higher interfacial resistance. Therefore, it can be concluded that the sodium was participating in the electrodeposition process.

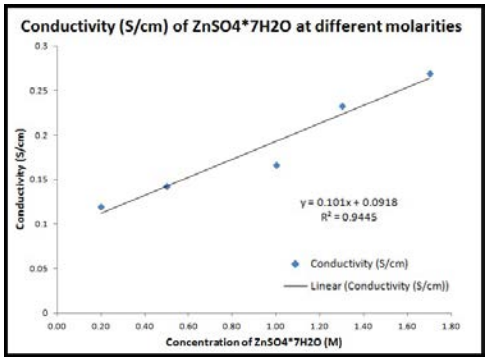

Figure 4: Linear regression of conductivity (S/cm) versus molarity of zinc sulfate heptahydrate.

Future Work:

Due to sodium participating in the electrodeposition process, silica nanoparticles and ionic liquids will be used as stable salt additives in order to study how it affects dendrite formation. The growth rate of each electrodeposition will be calculated using a Matlab code. Also, the transferance number of zinc in solutions will be determined as well.

Acknowledgements:

I would like to thank my professor Dr. Lynden A. Archer, my mentor Snehashis Choudhury, the program coordinators Melanie Claire-Mallison and Professor Susan Daniel. This project was supported by the Robert Frederick Smith School of Chemical and Biomolecular Engineering, Cornell University, and the National Science Foundation.

References:

[1] Garcia, G.; Ventosa, E.; Schuhmann, W. ACS Appl. Mater. Interfaces. 2017, 9, 18691.18698.

[2] Sun, K. E. K.; Hoang, T. K. A.; Nam, T.; Doan, L.; Yu, Y.; Zhu, X.; Tian, Y.; Chen, P. ACS Appl. Mater. Interfaces. 2017, 9, 9681.9687.

Nanostamp Optimization for Single-Molecule DNA/Protein Array Studies

Mónica M. López Martínez
Chemical Engineering, University of Puerto Rico-Mayaguez Campus

REU Program: 2017 Cornell NanoScale Science & Technology Facility
Research Experience for Undergraduates (CNF REU) Program
CNF REU Principal Investigator: Dr. Michelle D. Wang, Laboratory of Atomic and Solid State Physics, Howard Hughes Medical Institute, Cornell University
CNF REU Mentors: Ryan Badman, Laboratory of Atomic and Solid State Physics, Cornell University; Dr. James E. Baker, Laboratory of Atomic and Solid State Physics, Cornell University
Primary Source of CNF REU Funding: National Science Foundation via the National Nanotechnology Coordinated Infrastructure (NNCI) Grant No. ECCS-1542081
Primary CNF Tools Used: JEOL 6300 e-beam lithography, Oxford Cobra etcher, AFM, SEM
Contact: monica.lopez8@upr.edu, mdw17@cornell.edu, rpb226@cornell.edu, jeb94@cornell.edu
Website: http://www.cnf.cornell.edu/cnf_2017reu.html

Abstract:

Over the past two decades, biophysical single molecule DNA, RNA and motor protein studies have demonstrated the important role that the structural and mechanical properties of single molecules play in gene replication and expression. Specifically, genetic processes can be significantly affected when DNA experiences torque or protein interaction forces, which happens often *in vivo*. Single molecule DNA studies typically "tether" DNA between a protein anchor on a surface, and a microbead in solution, that can be twisted or pulled with optical or magnetic tweezers. Nanostamping of protein spot anchor arrays, compared to blanket coating a substrate with protein for DNA anchoring, aids in single molecule studies by precisely controlling the DNA anchor position. This improves resolution and throughput of the technique. Thus, we are exploring a nanostamping method called the "Ink Subtract Print" method by optimizing the dimensions of electron beam-patterned nanostamps that can selectively pattern arrays of 100-300 nm wide circles of protein on a glass surface.

Summary:

Introduction. The deoxyribonucleic acid molecule (DNA) has a double helix structure with unique mechanical properties that subsequently influence the way that other proteins interact with DNA to achieve complex biological functions of transcription and replication.

Our lab is interested in studying the interactions between DNA and motor proteins that are present in DNA processing activities. Although DNA can be macroscopically long, it is only 2 nm wide and cannot be visualized with light microscopy. DNA is therefore tethered between a microsphere handle and microscope slide for observation and manipulation.

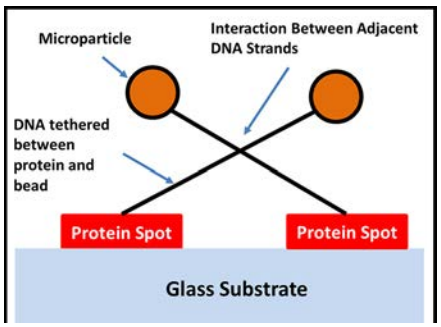

Figure 1: Schematic of protein-DNA-bead tethers.

To obtain organized observations of these microscopic molecules and investigate interactions between a protein and multiple DNA strands, we precisely placed the position of the separate DNA molecules on a glass slide so that the distance between strands was well-defined. Specifically, we patterned a protein surface array using the Ink-Subtract-Print (ISP) nanostamping method [1], so the DNA could be anchored on the surface at one end of the DNA molecule with high spatial precision. (Figure 1).

Ink-Subtract-Print Method (ISP). This protein patterning procedure consists of inking a PDMS square with protein to cover the whole surface, and then stamping the square on the patterned silicon template to remove the protein everywhere on the PDMS except in the array of small circles [1]. This subtractive step is physically possible because plasma cleaning the silicon template gives hydrophilic properties to the wafer. Since the protein on the PDMS is also hydrophilic, it will be attracted to the top surface of the subtraction template wafer.

When the PDMS is pulled away, the protein will be attached to the wafer in the non-patterned areas. In contrast, the PDMS will retain protein where the silicon wafer had holes. The patterned protein spots on the

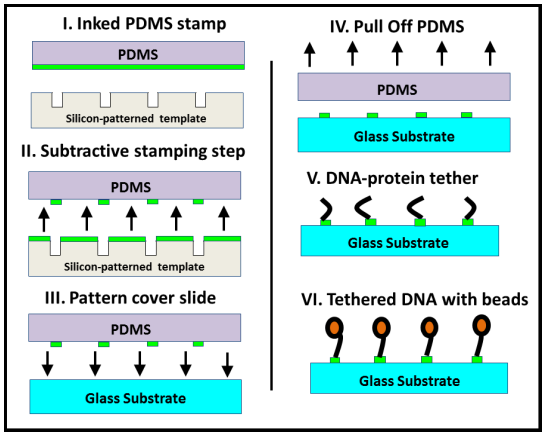

Figure 2. Ink-Subtract-Print stamping method.

PDMS after subtraction are, then, stamped or "printed" on a plasma-cleaned glass surface which will be the area used to perform the DNA-binding experiments. (Figure 2)

Nanofabrication of Patterned Silicon Template Method. Our main goal thus was to create patterned silicon templates containing periodic hexagonal arrays of 100-300 nm circular holes spaced at a 3 µm pitch that could be used as a subtraction template (Figure 3a) to produce patterned protein spots on PDMS (Figure 3b).

To acquire the target pattern needed to perform the ISP stamping procedure on our silicon wafer, the first step was to expose a silicon wafer coated with ZEP520A resist using the JEOL JBX-6300FS 100kV electron-beam (e-beam) lithography system. Once the wafer was exposed and developed, the Oxford Cobra inductively coupled plasma (ICP) etcher was used to etch the silicon wafer according to the e-beam pattern. To remove the ZEP520A and obtain our final cleaned, patterned nanostamp template, we used a bath of 1165 organic stripper for approximately four hours. Finally, we obtained four 1 cm × 1 cm stamp areas patterned on each wafer.

Results:

After four hours of DNA incubation time (13.7 kbp DNA, 25 pM), we observed an average of 10 tethers in each microscope field of view, which contained ~ 1,500, 150 nm wide protein spots. To increase the number of tethers, the incubation time was increased to 17 hours and yielded ~ 50-100 DNA-protein tethers per field of view. By increasing anchor protein spots to 300 nm in diameter, we were able to obtain more tethers in a shorter amount of time compared to 150 nm wide protein spots. An analysis of these results shows that since the area of each protein anchor spot is small compared to anchor spots described in previously published reports [2], it will take more time for the DNA to bind to these small features (Figure 4).

There are several ways to improve the number of DNA tethers in the future work: (1) Increase DNA concentration (2) tether DNA to magnetic beads and place a magnet under the glass so the DNA is more likely to dwell near the cover slide surface and thus more likely to bind to the protein anchor or (3) test larger stamp circles.

References:

[1] Coyer, Sean R., Andrés J. García, and Emmanuel Delamarche. "Facile Preparation of Complex Protein Architectures with Sub-100-nm Resolution on Surfaces." Angewandte Chemie International Edition 46.36 (2007): 6837-6840.

[2] De Vlaminck, Iwijn, et al. "Highly parallel magnetic tweezers by targeted DNA tethering." Nano letters 11.12 (2011): 5489-5493.

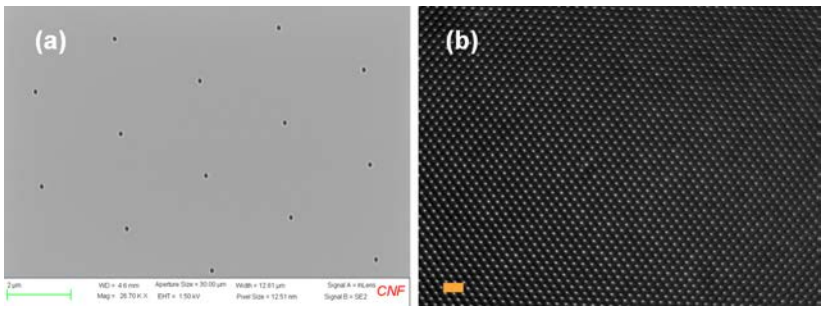

Figure 3: (a) A scanning electron microscope image of the silicon template with a hexagonal array of holes for subtractive stamping, scale bar is 2 µm. (b) A fluorescent microscope image of the final protein array on glass, scale bar is 6 µm.

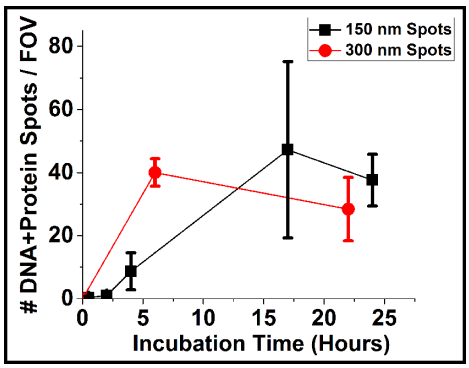

Figure 4: The number of DNA tethers bound to protein anchors per field of view (FOV) under a fluorescent microscope, per hour of incubation, using (1) 150 nm wide protein anchors and (2) 300 nm wide protein anchors.

Exploring Thermoelectric Properties of Thin Film YbB_x

Maya Martirossyan
Harvey Mudd College, Claremont, CA

REU Program: 2017 Cornell NanoScale Science & Technology Facility International Research Experience for Undergraduates (CNF iREU) Program at the National Institute of Material Science (NIMS), Tsukuba, Ibaraki, Japan
CNF iREU Principal Investigator and Mentors: Takashi Aizawa, Gabin Guélou, Takao Mori, National Institute of Materials Science, Tsukuba, Japan
Primary Source of CNF iREU Funding: National Science Foundation under Grant No. OISE 1559368
Contact: mmartirossyan@g.hmc.edu
Website: http://www.cnf.cornell.edu/cnf_2017reu.html

Introduction:

Thermoelectric materials have the potential as sources of renewable energy because they can generate electricity from heat with no waste, and vice versa, by the Peltier and Seebeck effects. To be a good candidate for thermoelectric power generation, a material must have a high electrical conductivity σ, high Seebeck coefficient S, and low thermal conductivity κ, in order to maximize the figure of merit, ZT, which is related to a materials power conversion efficiency. The ZT value is given by the equation:

$$\mathrm{ZT} = \frac{(S^2\sigma)T}{\kappa}$$

Typical commercial thermoelectrics have a ZT ≈ 1, but the necessary ZT for a good power conversion efficiency depends on the type of application [1].

Certain metal-boride compounds, such as SrB_6, have been known to make good thermoelectrics [2], as have bulk ytterbium-boride compounds [3,4]. Previously, only bulk YbB_6 has been investigated for its thermoelectric properties. Our research focuses instead on thin film ytterbium borides of many different stoichiometries. Thin film thermo-electrics are important to study because of their niche applications, such as use in microsensors or on flexible substrates [5].

Measurements and Results:

X-Ray Diffraction. X-ray diffraction (XRD) was used in order to determine the chemical composition of our thin films. The XRD data were collected over a 2θ range of 10-110°, at a rate of 2.0-2.8°/min, with a 0.02°/step. We first performed XRD analysis on our sapphire substrate in order to exclude the reflections originating from the substrate. Since the penetration depth of the x-rays were much larger than the thickness of our films, reflections with the highest intensities (and corresponding angle) were assigned to the substrate, and the remaining peaks correspond to reflections from the sample. Our deposition process produced highly orientated films, which resulted in XRD peaks of different intensities than those of a powder sample. The two primary YbB_x stoichiometries we observed from XRD analysis in our films were either YbB_6 or YbB_2, as shown in Figures 2 and 3. These two compounds differ greatly in their crystal structure: YbB_6 has a cubic structure with space group Pm-3m and a lattice constant of 4.1444 Å, while YbB_2 has a hexagonal structure with space group P6/mmm and a lattice constant of with lattice parameters 3.2503 Å × 3.2503 Å × 3.7215 Å [6].

Our XRD measurements did not allow us to deduce the exact stoichiometry of our films, and both our XRD data and the large variances in our measurements of electrical conductivity and Seebeck coefficient suggest that some of our samples may be non-stoichiometric.

Electrical Properties Measurements. The Ulvac ZEM-3 was used to measure the electrical properties of our thin films, using a 4-point probe method to measure the electrical resistivity and the Seebeck coefficient of our films simultaneously. We chose a temperature range of 325-575 K to measure these properties, as we could not go any higher without possibly damaging the electrical contacts. Measurements were performed several times on the same sample, in different locations on the sample in order to test for good uniformity. The color legend for all measured samples is provided in Figure 4.

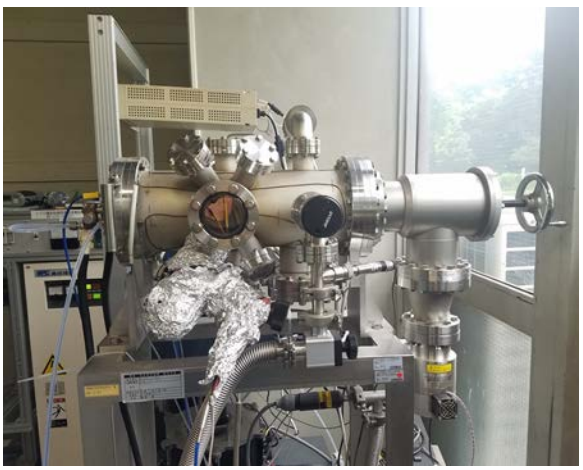

Figure 1: An image of our custom-built CVD tool.

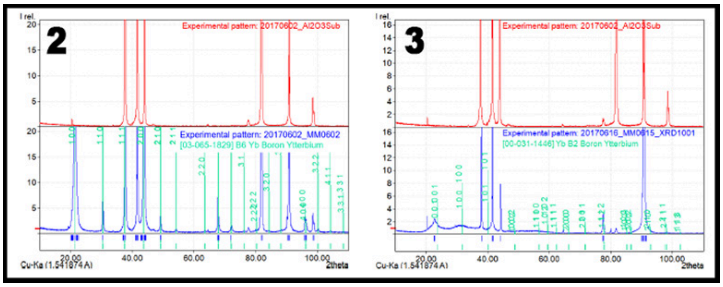

Figure 2, left: XRD analysis of a YbB_6 film. Figure 3, right: XRD analysis of a YbB_2 film.

As seen in Figure 5, our results from the Seebeck coefficient measurements show that our films all present n-type semiconducting behavior. Together, these results suggest that our films may all be degenerate semiconductors.

Our results from the resistivity measurements were not always very consistent for one given sample, and we can see from Figure 6 different slopes for different measurements on the same sample. However, these measurements remain within the same order of magnitude. Moreover, across measurements from different samples, the differences between individual measurements from each given sample are negligible, as can be seen from Figure 7.

The power factor, calculated from the Seebeck coefficient and the resistivity, gives us a clear understanding of which films might perform the best as thermoelectrics. For thermal properties measurements, we chose the best YbB_6 and the best YbB_2 film in order to proceed with measurements.

Time-Domain Thermoreflectance. We measured the thermal diffusivity of our thin films, necessary for calculating the thermal conductivity, using a picosecond time-domain thermoreflectance method [7]. After depositing an aluminum thin film on our sample, a picosecond laser was used to heat the sample, and a probe laser was used to measure how the reflectivity changed with the changing temperature of the sample. This process is shown in Figure 9. By fitting the curve of thermoreflectance vs. time, we calculated the thermal diffusivity of our thin films at room temperature.

Results and Conclusions:

From the thermal diffusivity measurements we were able to calculate room temperature thermal conductivity values for two of our samples. Using the power factor values at T ≈ 562 K, we calculated ZT values for these two films (Note: we expect the thermal conductivity to decrease with higher temperature, so the ZT at this temperature should be a slight overestimate). As shown in Table 1, we see that the ZT value for this YbB_6 sample to be an order of magnitude better than that of the YbB_2 sample. Our results suggest that thin film YbB_6 may make a better thermoelectric than thin film YbB_2 because of its higher ZT value. However, future work remains to be done on this research, such as finding the thermal conductivity at higher temperatures for more films, and potentially also examining thin film YbB_4 as a viable thermoelectric.

Acknowledgements:

Thank you to Isao Okubo for profilometer measurements, Kazuo Ogata for ZEM-3 measurements, Yohei Kakefuda for time-domain thermoreflectance measurements. Additionally, thank you to my mentors, Takashi Aizawa and Gabin Guélou, and professor Takao Mori. This material is based upon work supported by the National Science Foundation under Grant No. OISE 1559368.

References:

[1] CRC Handbook of Thermoelectrics. Rowe, David M. CRC Press, 1995.
[2] T. Tynell, et al. J of Crystal Growth 449 (2016) 10-14.
[3] M. Takeda, et al. J of Solid State Chemistry 177 (2004) 471-475.
[4] K Kaymura and M Takeda. IOP Conference Series: MSE, V20, N1.
[5] H. Baltes, et al. Sensors Set, 2008, pgs. 13-55.
[6] K. Momma and F. Izumi. J. Appl. Crystal-logr., 44, 1272-1276 (2011).
[7] Y.K. Koh, et al. J of Applied Physics 105, 054303 (2009).

Figure 4: The color legend for all the electrical properties measurements.

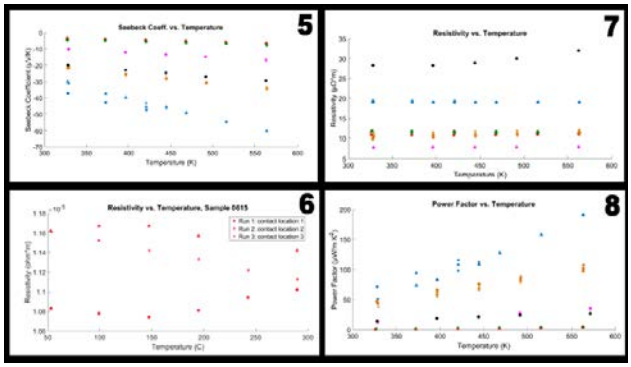

Figure 5: The Seebeck coefficient measurements over a range of temperatures for different thin films. Figure 6: The resistivity measurements over a range of temperatures for the same thin film. Figure 7: The resistivity measurements over a range of temperatures for different thin films. Figure 8: The power factor, calculated from the Seebeck coefficient and resistivity measurements, over a range of temperatures for different thin films.

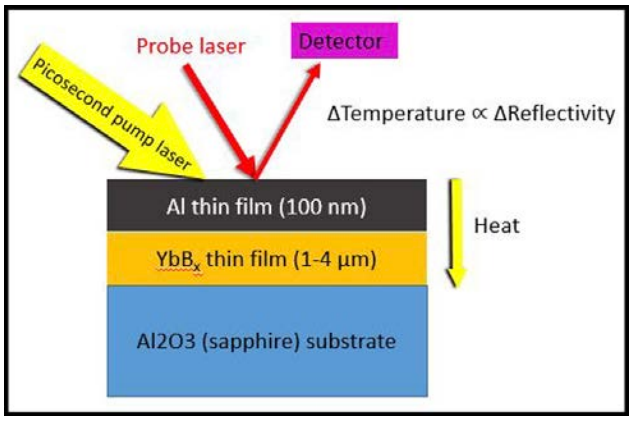

Figure 9: The process by which time-domain thermoreflectance works.

T ≈ 562 K	YbB_6	YbB_2
Power Factor (μ W/ mK)	191	4
Room Temp Thermal Cond. (W/mK)	2.540	1.064
ZT	≈ 0.04	≈ 2×10^{-3}

Table 1: The table of power factor at T ≈ 562 K, room temperature thermal conductivity, and calculated ZT from one YbB_6 (blue sample in Figure 4) and one YbB_2 sample (red sample in Figure 4).

Find Maya's complete CNF iREU report online at http://www.cnf.cornell.edu/cnf_2017reu.html

An Investigation into the Effects of Quantum Structures on the Carrier Dynamics of GaAs/GaNAs Solar Cells

John Nance

B.S. Physics, University of North Carolina - Chapel Hill

REU Program: 2017 Cornell NanoScale Science & Technology Facility International Research Experience for Undergraduates (CNF iREU) Program at the National Institute of Material Science (NIMS), Tsukuba, Ibaraki, Japan

CNF iREU Principal Investigators: Dr. Takeshi Noda, Photovoltaics Group, National Institute for Materials Science; Dr. Hiroyuki Sakaki, Nano-electronics Laboratory, Toyota Technological Institute

CNF iREU Mentor: Dr. Martin Elborg, Photovoltaics Group, National Institute for Materials Science

Primary Source of CNF iREU Funding: National Science Foundation under Grant No. OISE #1559368

Contact: jausnance@gmail.com, noda.takeshi@nims.go.jp, h-sakaki@toyota-ti.ac.jp, elborg.martin@nims.go.jp

Website: http://www.cnf.cornell.edu/cnf_2017reu.html

Abstract:

The addition of quantum wells (QWs) to solar cells is a potential method of implementing an intermediate band solar cell (IBSC). Three gallium arsenide (GaAs) solar cells containing ten differently doped gallium nitride arsenide (GaNAs) QWs are characterized, then compared to a reference GaAs solar cell via time-resolved photocurrent (TRPC) measurements. Carrier dynamics in QW solar cells is discussed.

Introduction:

The IBSC is a solar cell design with the potential to overcome the Shockley Quiesser efficiency limit for p-n solar cells. In these devices, the addition of an intermediate energy level within the band gap of the solar cell's host material allows the device to utilize a larger portion of the solar spectrum, resulting in an increased theoretical maximum efficiency of 63.1% [1]. This design can be implemented by the addition of nanostructures into the solar cell. A layer of material with a smaller band gap than the host material is added, creating wells in the band diagram. These QWs provide the intermediate energy states necessary for an IBSC.

Here we study how QW-originated states influence carrier transport properties. In this project we measure temporal evolution of photocurrent, which is generated by a nano-second laser.

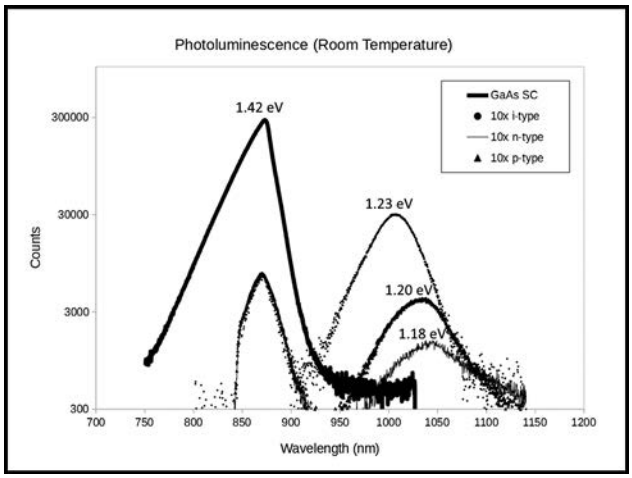

Figure 1: Photoluminescence spectrum at room temperature.

Experimental Procedure:

The four samples discussed here are a reference GaAs solar cell, and three GaAs solar cells containing ten GaNAs QWs. The three QW samples contain differently doped QWs, i-type, n-type, or p-type. Each sample was grown using molecular beam epitaxy (MBE), and, except for the presence or lack of QWs, they share the same dimensions. Following growth, each sample underwent an identical fabrication process in which electrical contacts are applied to each device.

Photoluminescence (PL) measurements were done to determine the nitrogen concentration and the depth of the GaNAs QWs. Each sample was illuminated with a 532 nm wavelength (2.33 eV) laser, and its photon emission spectrum was recorded. Current-voltage (IV) measurements were conducted on each device to characterize its performance under illumination by a solar simulator. The TRPC was measured for each device. The transient photocurrent signal was recorded with an oscilloscope under a single 2 ns pulse from a 532 nm, 40 μW laser. The power is controlled by filter and optical setup.

Results and Conclusions:

Figure 1 shows PL spectra of all samples at room temperature. A peak observed at 872 nm is shared between all samples, corresponding to the expected GaAs band gap of 1.42 eV at 300 K. Another peak in

the PL spectrum was observed at around 1030 nm (1.20 eV), which originates from the GaNAs QWs. The nitrogen composition and QW depth were determined to be 2%, and 0.22 eV, respectively, using the model for GaNAs band gap derived in [2]. Here we ignore the valence band discontinuity. Additionally, the relative intensities of the GaNAs peaks in the QW samples are indicative of the level of recombination in that sample, with the highest being i-type, lowest being n-type.

Figure 2 shows the IV curves obtained from each device. Rather than the expected increase in photocurrent, each QW sample showed a decrease in both short circuit current, and open circuit voltage, resulting in reduced efficiency.

The results of the TRPC measurements are shown in Figure 3. Table 1 lists the photocurrent decay time constants and the total number of extracted carriers, both obtained from the TRPC curves. The TRPC results for each QW sample vary. These differences must be due to recombination, as the only difference between each device is doping. The extracted carriers in the i-type QWs are the lowest, while those in the n and p-type QWs are comparable to those in the reference sample. Hence, recombination in the i-type QWs is higher than in the n and p-type QWs. This is consistent with PL results, as PL from the QW in i-type sample is higher than others.

We next discuss the time constant, τ, of photocurrent decay. The i-type sample exhibits a shorter time constant than other samples including the reference sample, which is reasonable because large recombination diminishes photogenerated carriers quickly. The fact that the n-type and the reference sample have very close τ, suggests that addition of QWs has little effect on carrier transport. In the p-type sample, the PC decay is characterized by two τ's. Although further work is necessary, our observation will be useful in understanding carrier transport in solar cell devices.

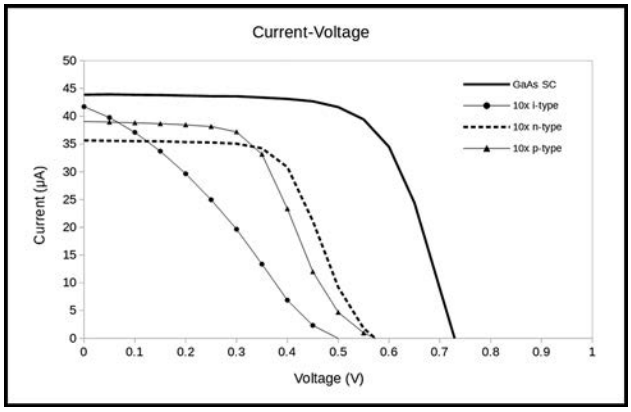

Figure 2: Light IV curves.

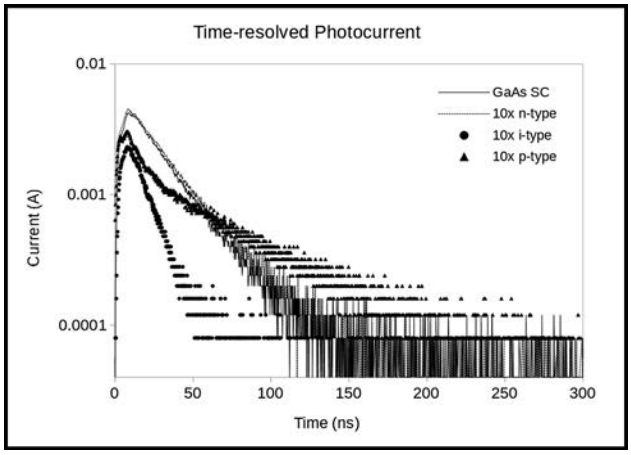

Figure 3: TRPC signals under single laser pulse.

	Time Constant (ns)	Extracted Carriers
GaAs SC	30.3	3.84E+18
10 i-type QWs	19.2	1.16E+18
10 n-type QWs	35.7	4.29E+18
10 p-type QWs	23.8, 66.7	3.57E+18

Table 1: Photocurrent decay time constants, and total number of extracted carriers.

Future Work:

Future experiments should measure TRPC in devices with the same QW doping, but varying number of QWs, to clarify the effect of trapping in devices with similar levels of recombination.

Acknowledgments:

I would like to thank my PI, Dr. Takeshi Noda, and my mentor, Dr. Martin Elborg, for their instruction and assistance in this project, and NNCI and NIMS for organizing this program. Research supported under National Science Foundation Grant OISE-1559368.

References:

[1] A. Luque and A. Marti, Phys Rev. Lett., 78, 26 (1997).

[2] W. Walukiewicz, et al., PV 99-11, p. 190, The Electrochemical Society Proceedings (1999).

Growth Parameter Control of Structures and Properties of Perovskite Thin Films

Skye Tackkett

Physics, Missouri University of Science and Technology

REU Program: 2017 Cornell NanoScale Science & Technology Facility International Research Experience for Undergraduates (CNF iREU) Program at the National Institute of Material Science (NIMS), Tsukuba, Ibaraki, Japan

CNF iREU Principal Investigator: Dr. Naoki Ohashi, Electroceramics Group, National Institute for Materials Science

CNF iREU Mentor: Dr. Takeo Ohsawa, Electroceramics Group, National Institute for Materials Science

Primary Source of CNF iREU Funding: National Science Foundation under Grant No. OISE #1559368

Contact: skye.tackkett@gmail.com, ohashi.naoki@nims.go.jp, ohsawa.takeo@nims.go.jp

Website: http://www.cnf.cornell.edu/cnf_2017reu.html

Abstract:

Application of growth parameters to control thin film structures and properties is an important method for improving film quality for applications in advanced electronic devices. Lattice engineering of thin films is key to improve the crystallinity and quality of films and the devices they comprise. In this study, as a model system we seek to control the growth of a perovskite oxide film, strontium titanate ($SrTiO_3$), through magnetron sputtering. Film growth of $SrTiO_3$ was investigated on lattice-matched lanthanum aluminate-strontium aluminum tantalite ($(LaAlO_3)_{0.3}(Sr_2AlTaO_6)_{0.7}$) substrates, where we focused on the distance between substrates and sputtering target. We find that alteration of the distance leads to good Sr and Ti control, high crystallinity, and smooth surfaces, but oxygen deficiency in the films is still an obstacle to improving the electrical properties.

Introduction:

Stacked thin film heterostructures are important in the development of many devices, such as multilayer ceramic capacitors, batteries, and integrated circuits [1]. Highly crystalline films and interfaces are essential in determining the quality of thin films and improving device performance.

Sample	Temperature (°C)	Sputtering power (W)	Ar flow (sccm)	Ar pressure (mTorr)	Distance (mm)	Deposition time (h)	Thickness (nm)
Sample A	500	40	0.2	20	53	1	165
Sample B	500	40	0.2	20	73	1	315
Sample C	500	40	0.2	20	93	1	22

Table 1: Typical deposition growth parameters for STO thin films.

The most common technique for producing practical stacked thin films is magnetron sputtering, due to the advantages of low-cost deposition and relative simplicity of the system [2]. To obtain high-quality thin films, lattice and orientation matching between substrate and film are important [3]. For instance, selection of substrates with larger or smaller lattice constants than those of the films results in tensile or compressive strain in the films, respectively. Selection of substrates and growth parameter optimization during sputtering deposition are crucial to improve film properties.

Our goal in this project is to alter growth parameters to control perovskite thin film structures and properties. In this study, we used a compact sputtering gun with an adjustable head and controlled the distance between the substrate and sputtering target during deposition to fabricate $SrTiO_3$ (STO) thin films.

Experimental Procedure:

Thin films of STO were grown on lattice-matched $(LaAlO_3)_{0.3}(Sr_2AlTaO_6)_{0.7}$ (100) (LSAT) and lanthanum aluminate, $LaAlO_3$ (LAO) substrates using radio-frequency magnetron sputtering. In-plane lattice constants of STO and LSAT are 0.390 and 0.387 nm, respectively, resulting in $(a_{STO}-a_{LSAT})/a_{LSAT}=0.0103$. Typical growth conditions are summarized in Table 1. These conditions were held constant for each sample, but the sample holder height was changed to 130 mm, 150 mm, or 170 mm, which correspond to a distance ($d_{s\text{-}t}$) between substrate and sputtering target of 53 mm, 73 mm, and 93 mm, respectively. After the sputtering depositions, STO films were characterized via profilometry, atomic force microscopy (AFM), x-ray diffraction (XRD), and x-ray fluorescence (XRF). Gold/titanium electrodes were deposited onto the films using vacuum evaporation to form Ohmic contacts for resistivity and Hall-effect measurements.

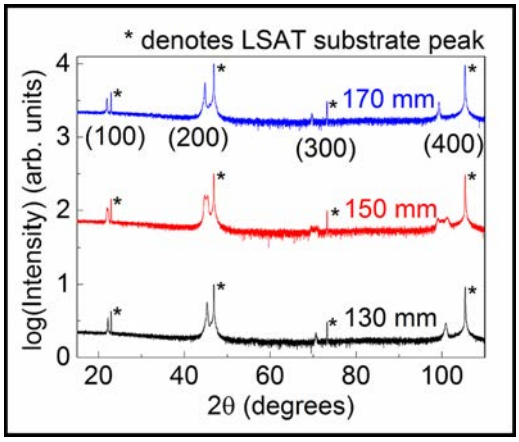

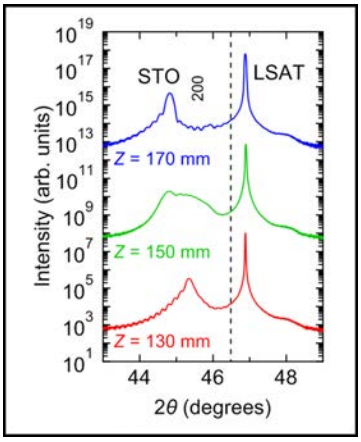

Figure 1, left: XRD wide scan of STO/LSAT samples. Figure 2, right: XRD (200) peak of STO/LSAT samples.

Results and Conclusions:

Figure 1 shows XRD wide scans of the STO/LSAT samples deposited under different $d_{s\text{-}t}$. It is clear the films were *c*-axis oriented and single-phase without impurity peaks. A closer look at the 200 peak of the films shows all three film peaks occurred at lower angles than the bulk STO peak, represented by the dashed line in Figure 2. The lower peak angles indicate the films are compressively strained, as the lattice constant of LSAT is lower than that of STO, which led to the lengthening of the c-axis parameters. Additionally, oscillations visible on the 200 peak are an indication the films are highly crystalline, which was confirmed by rocking curve scans showing peak widths around 0.1°.

The AFM images (Figure 3) of the STO/LSAT samples revealed the thin films were significantly more smooth, with a root-mean-square roughness of 0.177 nm and 0.271 nm for samples A and C, respectively. The faint diagonal lines visible in Figure 3 indicated stepped-and-terraced surface, implying the surface of sample C was very flat. We performed XRF measurements on the STO/LAO samples rather than the STO/LSAT, as LAO does not contain Sr which would convolute the measurement. The XRF analysis of the stoichiometry revealed a Sr deficiency in sample A, but near stoichiometric ratios of Sr:Ti in samples B and C. These results imply that the enlargement of *c*-axis parameters resulted from compressive strain and amount of oxygen rather than cation (non)stoichiometry.

Electric properties collected from Hall-effect measurements showed resistivity (1.1 Ωcm) and carrier concentration ($2.8*10^{19}$ cm^{-3}) in sample C were several orders of magnitude different than the other samples. In fact, sample C looked light gray, indicating an oxygen-deficient film as is usually seen in n-type oxide semiconductors. Although former literatures reported that compressively strained STO films show a ferroelectric transition [4], our STO films, even sample C, could not show these effects.

We were able to conclude that our sputtering method grew highly crystalline STO thin films with smooth surfaces. Cation stoichiometry for Sr and Ti was controlled through the changing of $d_{s\text{-}t}$. Electric properties remained poor due to oxygen deficiency in the STO films.

Future Work:

Oxygen control is necessary in improving the properties of sputtered thin films. In order to achieve this control, we can next use oxygen gas exposure in addition to argon gas during the sputtering deposition procedure. Additionally, we can test the effect of changing the angle of the head of our sputtering gun and tune the angle for property control of the film growth.

Acknowledgements:

I would like to thank my PI, Dr. Naoki Ohashi, my mentor, Dr. Takeo Ohsawa, the iREU site staff, Drs. Lynn Rathbun and Nancy Healy, and the CNF iREU Program. This work was supported by the National Science Foundation Award OISE: 1559368.

References:

[1] Kambara, H. et al. Chemical Solution Deposition of Functional Oxide Thin Films. Vienna (Austria): Springer. Chapter 22: Thin Film Multilayer Capacitors; p. 547-570(2013).

[2] Harp, G.R. et al. Thin Solid Films, 288 (1-2):315-324 (1996).

[3] Hecht, J. Understanding Lasers: An Entry-Level Guide. New York (NY): Wiley-IEEE Press. Chapter 8: Semiconductor Lasers; p.246-294 (2001).

[4] Verma, A. et al. AP Letters, 107(19):192908 (2015).

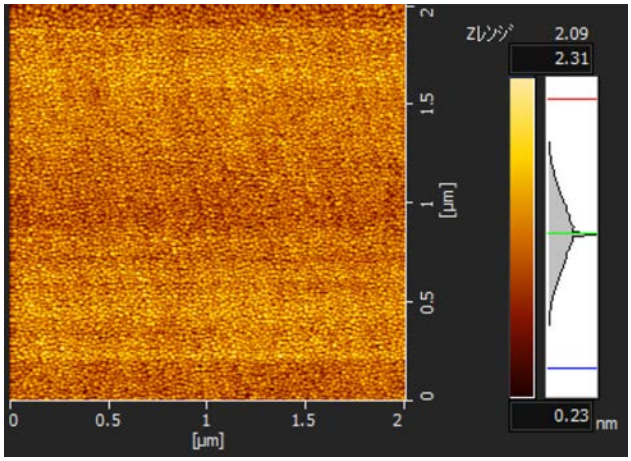

Figure 3: 2000 × 2000 nm 0.98 Hz AFM scan of 170 mm STO/LSAT thin film.

Piezoelectric RF SAW-Based Energy Detectors

Daniel Teal

Mechanical Engineering & Mathematics, University of Texas at Austin

REU Program: 2017 Cornell NanoScale Science & Technology Facility
Research Experience for Undergraduates (CNF REU) Program
CNF REU Principal Investigator: Dr. Amit Lal, SonicMEMS Lab, Cornell University
CNF REU Mentor: Alex Ruyack, SonicMEMSLab, Cornell University
Primary Source of CNF REU Funding: National Science Foundation via the National Nanotechnology Coordinated Infrastructure (NNCI) Grant No. ECCS-1542081
Primary CNF Tools Used: Heidelberg 2000, SÜSS MA6, odd-hour evaporator, Disco dicing saw, ultrasonic wire bonder
Contact: dteal@utexas.edu, amit.lal@cornell.edu, arr68@cornell.edu
Website: http://www.cnf.cornell.edu/cnf_2017reu.html

Abstract:

Extremely low-power electronic devices promise improvements in remote and distributed sensor networks, among other applications. Thus, we have designed and studied mechanisms based on piezoelectric surface acoustic wave (SAW) and graphene properties that detect and manipulate high frequency (200 MHz) electronic signals characteristic of radio frequency (RF) communications intercepted by such a device in hopes of using these signals as a power source. We demonstrate conversion of RF signals to SAWs on a lithium niobate (LN) substrate with standard interdigitated transducers. Electrodes of monolayer graphene placed on top of the substrate intercept the SAWs and convert them back to electric current via the acoustoelectric effect.

Summary of Research:

Our ultimate goal is to create devices that can trigger a nanoelectromechanical (NEMS) switch using a nanowatt radio frequency (RF) signal. To this purpose, here we build mechanisms that have the potential to rectify or otherwise modify such an alternating current (AC) RF signal at the Cornell NanoScale Science and Technology Facility (CNF).

A surface acoustic wave (SAW), a Rayleigh wave, can be excited on a piezoelectric substrate by means of an interdigitated transducer (IDT) — an array of electrodes with alternating electrical bias. Because the substrate is piezoelectric, such a wave carries with it an alternating electric field. Next, monolayer graphene placed on top of the substrate allows electron mobility. Electrons are pushed by the field caused by the SAW, namely, the acoustoelectric effect. This electron current can be captured by electrodes placed across the path of the SAW. The current across these electrodes is proportional to the SAW power density and cross-sectional area of the conductor [1]. We also note a related physical effect: the resistivity of graphene increases whenever the material undergoes strain [2], as when stretched by a passing SAW.

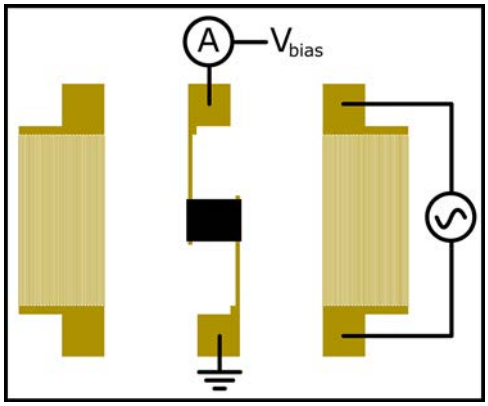

Figure 1: Schematic of tested device. Length of IDT fingers is approximately 1 mm. A rectangle of graphene (black, center) is placed on two electrodes and in between two IDTs.

We use 4-inch 128°Y-cut black lithium niobate (LN) wafers as device substrates. SAWs will propagate in the X direction. First, gold electrodes are patterned using a liftoff process — 75 nm of gold are evaporated with a 10 nm Ti adhesion layer on top of a 2.5 µm negative photoresist mask of nLOF 2020. The nLOF is dissolved in 1165 to isolate the electrodes. Gold IDTs use 5 µm electrodes at a 10 µm pitch for a 20 µm wavelength. We designed for 200 MHz signals.

Inspired by Trung, et al. [3], we attempted to use a liftoff process to pattern graphene on top of the gold. An alternative method was to pattern gold with an oxygen plasma RIE etch with a photoresist mask, but the CNF does not allow gold to be used in most RIE tools. We found that graphene transferred via (CITE) on top of our LN wafer with a 2 µm nLOF 2020 mask, baked overnight at 130°C, then placed in 1165 for half an hour and 30s in the ultrasonicator produces graphene features reliably. However, graphene resistors with thicknesses less than 100 µm cannot be manufactured reliably. Finally, the chips were diced with the Disco saw and wirebonded to printed circuit boards (PCBs) that connected to external instrumentation.

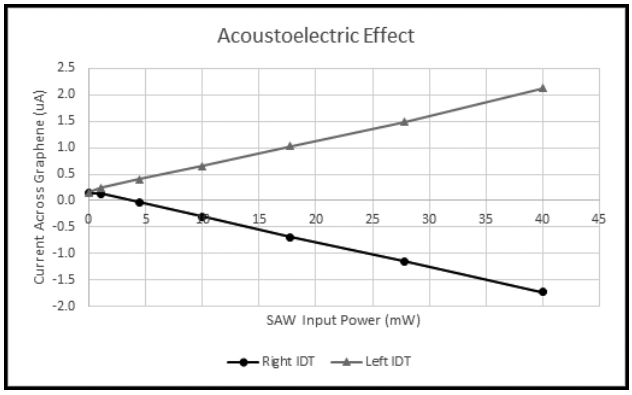

Figure 2: Power input to IDT to create SAW vs. current output from graphene for each IDT.

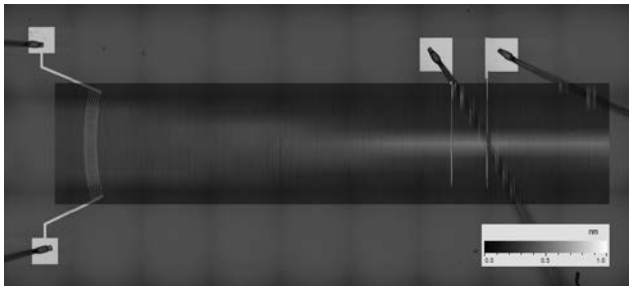

Figure 3: Another device. A curved IDT, left, creates a SAW that propagates right to an invisible piece of graphene placed across two electrodes. The SAW is concentrated at the graphene location.

Among other tests, we placed two IDTs opposing each other with a graphene electrode in the center, as shown in Figure 1. An alternating current fit into either IDT should induce an acoustoelectric current in the graphene, confirming the process's functionality. In Figure 2, we plot the current measured across the graphene with a Keithley 2400 when the instrument is set to source zero voltage bias. A 192.733 MHz wave, its frequency having been chosen as a resonance peak via an earlier frequency sweep on the device, was fed into the left, then right IDT at various powers through a 50 Ω waveform generator. We observed that current was affected linearly with IDT intensity as predicted by Bandhu, et al. [1], and the SAWs sent in opposite directions produced opposite changes, as expected.

We also measured the location intensity of a SAW generated from a curved IDT with a Polytec UHF scanning doppler vibrometer. Focusing the SAW had two benefits: first, it was easier to capture the entirety of the SAW energy with a graphene electrode, and second, the greater strain from the SAW amplitude should increase the graphene resistance, thus increasing the voltage induced across the graphene. The measurement is shown in Figure 3.

Results and Conclusions:

We have successfully replicated the acoustoelectric effect using a lithium niobate process in the CNF cleanroom, as well as a focused SAW. We conclude these processes may work for our purposes, namely, triggering a NEMS switch from an extremely low power RF signal.

Future Work:

Now that we can build this system in the CNF, we need to scale it to work with much less power. Once complete, this system can be combined with RF generating sensors and a NEMS switch.

Acknowledgements:

Thanks to my PI, Dr. Amit Lal, my mentor, Alex Ruyack, and acquaintances, Benyamin Davaji and Nabil Shalabi, for technical help, and for the CNF for hosting this internship. Finally, the National Science Foundation via the National Nanotechnology Coordinated Infrastructure (NNCI) Grant No. ECCS-1542081 provided funding for this Research Experience for Undergraduates Program.

References:

[1] Bandhu, L., Lawton, L. M., and Nash, G. R. (2013). Macroscopic acoustoelectric charge transport in graphene. Applied Physics Letters, 103 (13), 133101. https://doi.org/10.1063/1.4822121

[2] Fu, X.-W., et al. (2011). Strain dependent resistance in chemical vapor deposition grown graphene. Applied Physics Letters, 99(21), 213107. https://doi.org/10.1063/1.3663969

[3] Trung, T.N., Kim, D.-O., Lee, J.-H., Dao, V.-D., Choi, H.-S., and Kim, E.-T. (2017). Simple and Reliable Lift-Off Patterning Approach for Graphene and Graphene-Ag Nanowire Hybrid Films. ACS Applied Materials & Interfaces, 9(25), 21406-21412. https://doi.org/10.1021/acsami.7b05790

Manipulation of Cell Spreading and Cytoskeleton of Stem Cells by Micropatterned Surfaces

Cooper Thome

Chemical Engineering, University of Tennessee at Chattanooga

REU Program: 2017 Cornell NanoScale Science & Technology Facility International Research Experience for Undergraduates (CNF iREU) Program at the National Institute of Material Science (NIMS), Tsukuba, Ibaraki, Japan

CNF iREU Principal Investigator: Dr. Guoping Chen, Tissue Regenerations Group, National Institute for Materials Science

CNF iREU Mentor: Yingjun Yang, Tissue Regenerations Group, National Institute for Materials Science

Primary Source of CNF iREU Funding: National Science Foundation under Grant No. OISE #1559368

Contact: gwf532@mocs.utc.edu, guoping.chen@nims.go.jp, yang.yingjun@nims.go.jp

Website: http://www.cnf.cornell.edu/cnf_2017reu.html

Abstract:

This study aimed to further explore the manipulation of cell spreading and cytoskeleton of mesenchymal stem cells (MSCs) by use of easily fabricated micropatterned surfaces designed for single-cell culture and precise control of cell spreading area. Micropatterned surfaces were fabricated by a UV photolithographic process using azidophenyl-derivatized PVA (AzPhPVA), a photoreactive and non-cell-adhesive polymer. AzPhPVA and micropatterned surfaces were characterized using assorted techniques. General MSC cytoskeletal structure and morphology were analyzed using fluorescence and confocal microscopy. Significant cytoskeletal and morphological differences were observed between cells with small and large spreading areas.

Introduction:

Mesenchymal stem cells (MSCs) are undifferentiated cells that exhibit multipotency, the ability to differentiate into a variety of types of cells, as well as the potential for long-term self-renewal. MSCs have a variety of therapeutic applications and are widely studied in tissue engineering [1]. It has been shown that MSC structure and behavior are dependent on the cellular microenvironment, which has both biochemical and biophysical components. The cell spreading area, a biophysical microenvironmental component, has been shown to affect MSC cytoskeletal formation and differentiation, amongst other cell behaviors [2,3].

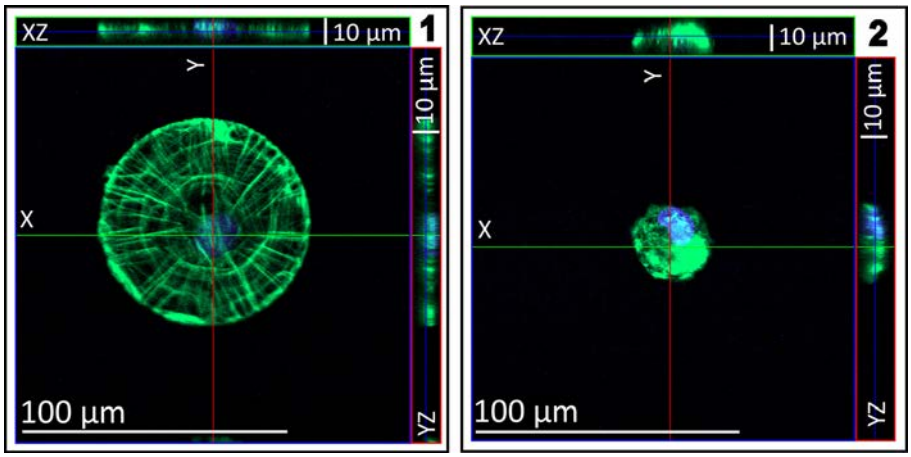

Figure 1, left: Confocal microscope image of MSC cultured on 80 µm micropattern and stained for F-actin. Note the defined actin filaments in the large image and the flat morphology shown in the XZ and YZ cross-sections. Figure 2, right: Confocal microscope image of MSC cultured on 30 µm micropattern and stained for F-actin. Note the randomly oriented cortex actin in the large image and the rounded morphology shown in the XZ and YZ cross-sections.

Our goal was to fabricate micropatterned surfaces designed to precisely control cell spreading of single cells to further analyze cell morphology and cytoskeletal structure of MSCs. Specifically, actin structures of MSCs at varied spreading areas were examined.

Experimental Procedure:

Azidophenyl-derivatized poly(vinyl alcohol) (AzPhPVA), a photoreactive and non-cell-adhesive polymer, was synthesized from poly(vinyl alcohol) (PVA) and 4-azidobenzoic acid and purified according to a previous work [2]. The resulting AzPhPVA solution was analyzed using ultraviolet-visible spectroscopy, which indicated successful grafting of the azidophenyl-derived group to the PVA. Using ^{1}H-NMR spectroscopy, the grafting ratio was calculated to be 2.5%.

To fabricate micropatterned surfaces, cell-adhesive polystyrene substrates were cut from a vacuum gas plasma treated tissue culture flask. Substrates were then coated with 200 µl of AzPhPVA using a drop coat method. The AzPhPVA was dried at 25°C in the dark. After drying, the AzPhPVA coated substrates were UV irradiated through a photomask containing six matrices of microdots with designed diameters of 10, 20, 30, 40, 60, and 80 µm. After UV irradiation, samples were placed in an ultrasonic bath in Milli-Q water in order to remove the excess and unexposed AzPhPVA, revealing patterns of polystyrene microdots in the AzPhPVA layer. The resultant micropatterned surfaces were characterized using both optical microscopy and atomic force microscopy (AFM). 3D images of the microdots collected from AFM were used to determine micropattern diameter and thickness. Examples of standard 3D AFM images are seen in Figures 1 and 2. The diameters of the micropatterned microdots were nearly identical to those of the microdots on the photomask. The thickness of the micropatterns varied from 50.56 to 90.76 nm, which is suitable for single-cell adhesion and culture.

After micropattern characterization, human MSCs were cultured on the micropatterns. After a few hours, cells adhered and spread on microdots, which controlled cell spreading area and morphology. Cell adhesion was significantly lower for micropatterns with diameters of 10 and 20 µm when compared to larger diameter micropatterns. After spreading, MSCs were stained for F-actin filaments which were observed by fluorescence and confocal microscopy.

Results and Discussion:

The UV photolithography micropatterning technique was successful for fabricating micropatterns for single-cell culture and precise control of cell spreading. Fluorescence microscopy revealed significant cyto-skeletal and morphological differences between cells with varied spreading areas. Cells with larger spreading areas, such as on the 80 µm microdots, exhibited highly ordered actin structures characterized by defined filaments organized in both the radial and concentric fashion. Cells with smaller spreading area, mostly 30 µm and below, did not exhibit defined filaments but instead showed randomly oriented cortex actin. Additionally, the morphology of the MSCs at varied cell spreading areas was quite different. As seen in confocal microscope images in Figures 3 and 4, cells with larger cell spreading areas had a flat morphology, while cells with smaller spreading areas became more rounded.

Future Work:

Future work includes further cytoskeletal analysis of MSCs with varied cell spreading, as well as the study of the influence of cell spreading area on MSC behavior, possibly in relation to biochemical microenvironmental components. The UV photolithographic technique also allows for the creation of a variety of micropattern geometries which may be further explored.

Acknowledgements:

I would like to thank my Principal Investigator, Dr. Guoping Chen, as well as my mentor, Yangjun Yang, and rest of the Tissue Regenerations Group at the National Institute for Materials Science (NIMS) for help and guidance throughout this project. I would also like to thank NIMS, Cornell NanoScale Facility (CNF), National Science Foundation (NSF), and Dr. Lynn Rathbun for making this experience possible. The NSF, via CNF Grant No. OISE #1559368, provided funding.

References:

[1] Song, W.; Kawazoe, N.; Chen, G., Dependence of Spreading and Differentiation of Mesenchymal Stem Cells on Micropatterned Surface Area. Journal of Nanomaterials 2011, 2011, 9.

[2] Wang, X.; Nakamoto, T.; Dulinska-Molak, I.; Kawazoe, N.; Chen, G., Regulating the stemness of mesenchymal stem cells by tuning micropattern features. Journal of Materials Chemistry B 2016, 4 (1), 37-45.

[3] Kilian, K. A.; Bugarija, B.; Lahn, B. T.; Mrksich, M., Geometric cues for directing the differentiation of mesenchymal stem cells. Proceedings of the National Academy of Sciences 2010, 107 (11), 4872-4877.

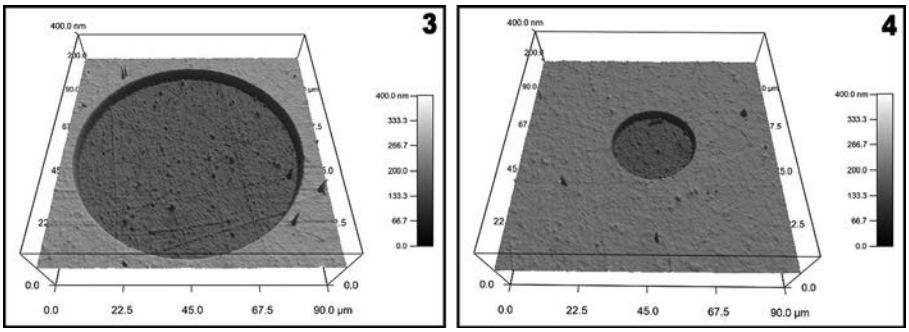

Figure 3, left: Typical 3D atomic force microscopy image of 80 µm microdot. The bottom of the microdot is cell-adhesive polystyrene, while the walls and rest of the upper surface are non-cell-adhesive AzPhPVA. Figure 4, right: Typical 3D atomic force microscopy image of a 30 µm microdot. The bottom of the microdot is cell-adhesive polystyrene, while the walls and rest of the upper surface are non-cell-adhesive AzPhPVA.

Investigation of Ferroelectric Properties of Oxide Superlattices at Low Temperatures: How do Strain, Dimensionality, and Polarization Compete in the Low-Dimensional Structure, $(SrTiO_3)_n(BaTiO_3)_mSrO$?

Vibha Vijayakumar

The California Institute of Technology

REU Program: 2017 Platform for the Accelerated Realization, Analysis, and Discovery of Interface Materials Research Experience for Undergraduates (PARADIM REU) Program with Caltech SURF

PARADIM REU Principal Investigator: Dr. Darrell Schlom, PARADIM Director, Materials Science and Engineering, Cornell University

PARADIM REU Mentor: Natalie Dawley, Materials Science and Engineering, Cornell University

REU Caltech Co-Mentor: David Hsieh, Assistant Professor of Physics, California Institute of Technology

Primary Sources of PARADIM REU Funding: NSF Materials Innovation Platform Program, Grant # DMR-1539918; Caltech Student-Faculty Programs Summer Undergraduate Research Fellowship (SURF)

Contact: vvijayak@caltech.edu, schlom@cornell.edu, nmd59@cornell.edu

Website: http://www.cnf.cornell.edu/cnf_2017reu.html

Abstract:

The oxide superlattice $(SrTiO_3)_nSrO$ has been identified as a promising tunable dielectric for modulating frequency signals, especially at 5G gigahertz frequencies, due to its epitaxial strain to enhance tunability and defect mitigating structure that reduces charged point defects. The next generation of this material, $(SrTiO_3)_n(BaTiO_3)_1SrO$ thin films, combines two ferroelectric materials, $SrTiO_3$ and $BaTiO_3$, in a superlattice broken up with non-ferroelectric SrO layers.

This study explored the in-plane and out-of-plane ferroelectric and dielectric properties of the $(SrTiO_3)_n(BaTiO_3)_1SrO$ thin films at temperatures 80-340 K for n = 1, 3, and 5. Understanding the competing $SrTiO_3$'s and $BaTiO_3$'s polarizations' interactions can be useful for optimizing the material for planar and vertical devices. Measurements involved the use of Cr/Au interdigitated electrodes for in-plane characterization and a $SrRuO_3$ bottom electrode with Cr/Au circular top electrodes for out-of-plane characterization. The data was collected by combining ferroelectric and dielectric measurement software with a low temperature probe setup. By investigating dielectric constants with temperature and measuring ferroelectric hysteresis loops at 80 K, we found that in-plane shows a clear ferroelectric transition around 170-180 K and clearly shows ferroelectric properties at 80 K. Out-of-plane measurements show high leakage and did not clearly indicate ferroelectric properties.

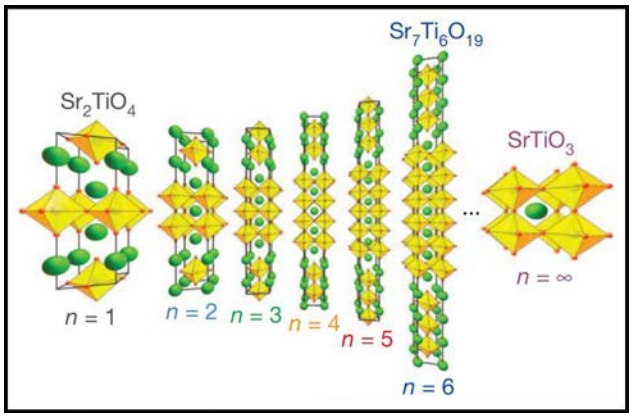

Figure 1: Structure of $(SrTiO_3)_nSrO$ [1].

Introduction and Background:

Telecommunications companies have been exploring gigahertz frequencies for 5G cell phone technologies as fertile territory to address our ever-increasing need for more data.

Prof. Darrell Schlom's group at Cornell University identified the Ruddlesden-Popper phase, $(SrTiO_3)_nSrO$ (see Figure 1 for structure), as a candidate for its low loss in bulk and reduced point defects. The resulting paper found $(SrTiO_3)_nSrO$ phases exhibited high performance levels and was highly tunable for n > = 3 at frequencies up to 125 GHz. The superlattice periodicity, n, can additionally be exploited to achieve high performance at room temperatures [1].

Results:

By investigating dielectric constants between the temperatures 80 K and 340 K and measuring ferroelectric hysteresis loops at 80 K, we found that in-plane samples show a clear ferroelectric transition around 170K at about 1000 (see Figure 2) for n = 3 and around 180 K at about 1100 for n = 5 (note: n as in $(SrTiO_3)_n(BaTiO_3)_1SrO$). In-plane samples for n = 3, 5 are clearly ferroelectric at 80 K (see Figure 3). Additionally, out-of-plane measurements have high leakage (see Figure 4) and did not clearly indicate ferroelectric properties for any value of n (see Figure 5 a and b for further explanations and graphs). To lower dielectric leakage for the out of plane devices, recommendations

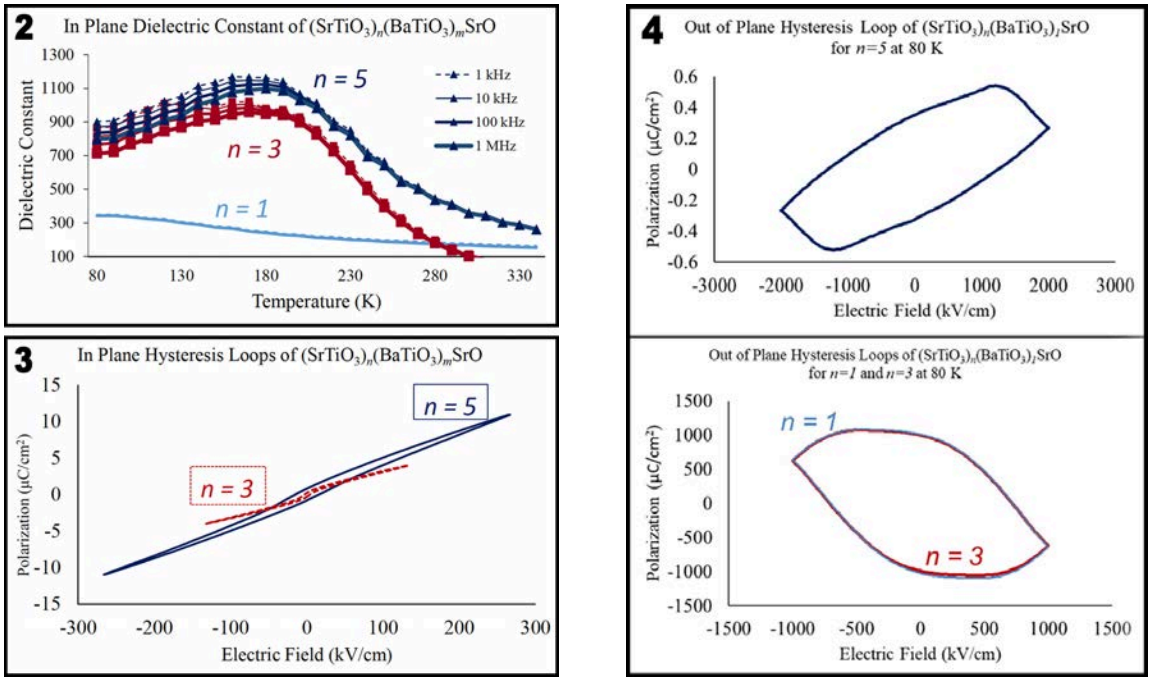

Figure 2, top left: For* n *= 1, there is no peak that would be indicative of a ferroelectric transition. In contrast, for* n *= 3 and for* n *= 5, there are peaks indicating ferroelectric properties. Figure 3, bottom left: The shapes of the hysteresis loops indicate presence of ferroelectric properties (though probably not that strong). Figure 4, right: The top graph for the sample* n *= 5, while indicating reasonable looking polarization values, indicates leakage from the shape. This leakage is made much more clear in the* n *= 1 and* n *= 3 samples in the bottom graph, which shows unreasonable polarization measurements.

are to use more oxide compatible materials for both electrodes and to use smaller pad sizes if possible (the size used was 150 μm in diameter).

Acknowledgements:

The author would like to thank Caltech SURF, PARADIM REU Program, and National Science Foundation for their support. The author would also like to thank Professor Schlom and Natalie Dawley for the opportunity to conduct this SURF project. And finally, she would like to thank to Dr. Julia Mundy for her advice and Dr. Vladimir Vladimirovich Protasenko for training on the cryoprobe equipment.

References:

[1] C.H. Lee, N.D. Orloff, T. Birol, Y. Zhu, V. Goian, E. Rocas, R. Haislmaier, E. Vlahos, J.A. Mundy, L.F. Kourkoutis, Y. Nie, M.D. Biegalski, J. Zhang, M. Bernhagen, N.A. Benedek, Y. Kim, J.D. Brock, R. Uecker, X.X. Xi, V. Gopalan, D. Nuzhnyy, S. Kamba, D.A. Muller, I. Takeuchi, J.C. Booth, C.J. Fennie, and D.G. Schlom, "Exploiting Dimensionality and Defect Mitigation to Create Tunable Microwave Dielectrics," Nature 502, (2013) 532-536.

Find Vibha's full Caltech report online at http://paradim.cornell.edu/education/2017-reu-participants/

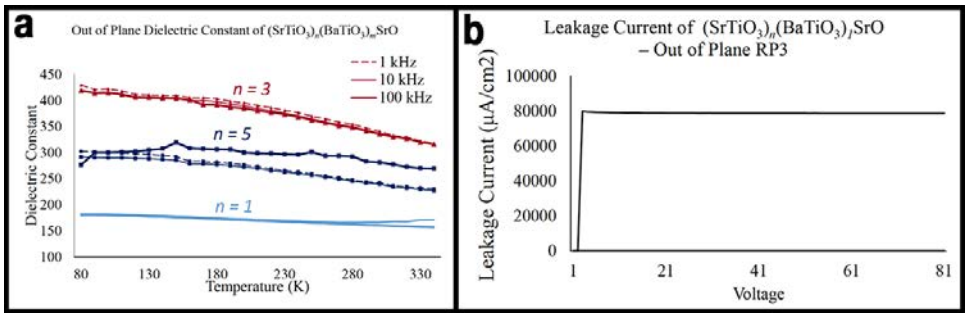

Figure 5: (a) For all of the samples measured, there is no clear peak, and therefore, ferroelectric transition indicated. Compared to in-plane, out-of-plane dielectric constants are much lower. (b) This measurement shows that for even voltages as low as perhaps 5V, the leakage current measured is extremely high.

Tracking Atoms in Two-Dimensional Materials Using Scanning Transmission Electron Microscopy

Jacob Waelder

Department of Physics, University of Washington

REU Program: 2017 Platform for the Accelerated Realization, Analysis, and Discovery of Interface Materials Research Experience for Undergraduates (PARADIM REU) Program

PARADIM REU Principal Investigator: Lena Kourkoutis, School of Applied and Engineering Physics, Cornell University

PARADIM REU Mentor: Ismail El Baggari, Department of Physics, Cornell University

Primary Source of PARADIM REU Funding: NSF Materials Innovation Platform Program, Grant # DMR-1539918

Contact: jacob.waelder@gmail.com, lena.f.kourkoutis@cornell.edu, ie52@cornell.edu

Website: http://www.cnf.cornell.edu/cnf_2017reu.html

Abstract:

Layered transition metal dichalcogenides (TMDs) possess unusual physical properties, such as superconductivity and metal-to-insulator transitions, that strongly depend on the structure of the atomic lattice. In tantalum ditelluride ($TaTe_2$), a structural phase transition occurs below 150 K, as indicated by x-ray diffraction and bulk resistivity measurements, but the precise microscopic structure is not well understood. Here, we use scanning transmission electron microscopy (STEM) to map the structure of $TaTe_2$ with atomic resolution. We perform measurements at room and liquid nitrogen temperatures, and at each of these temperatures the material is imaged from two different lattice orientations. We use fast Fourier transforms (FFTs) of the lattice images to extract periodic lattice information, and compare the high and low temperatures to determine the structural phase change. Atomic mapping of this structural phase change can help to understand and utilize the exotic properties of $TaTe_2$.

Introduction:

A Titan Themis CryoS/TEM is used at 300 kV to scan a narrowly focused electron beam across a thin sample of material. Electrons scattered from the sample are recorded on an annual detector at each scan position to produce a two-dimensional (2D) image. The STEM can image materials with atomic resolution, and the intensity of the image will scale with atomic number. Using this, a structural phase change in $TaTe_2$ at 150 K can be investigated.

These projection images will only give 2D information about the material, so two different lattice orientations are chosen to give a more complete picture of the structural changes. The plan-view orientation is a top-down view of the material 90-degrees rotated from the b-axis, and the cross-sectional orientation is along the b-axis where the gaps between the individual layers of the material are visible. The structural change in $TaTe_2$ is subtle, and requires high precision STEM imaging. Averaging over the entire field of view, the FFT of an image will have intensity peaks that correspond to its periodic structure. Because of this, FFTs are used to determine structural changes between two images; a more complex FFT implies a more complex physical structure.

Sample Preparation:

In preparation for STEM imaging the samples have to be thinned to electron transparency. To view the desired orientations, the $TaTe_2$ must be prepared for the microscope such that the imaging plane is orthogonal to the electron beam (Figure 1). The plan-view orientation is obtained through a standard mechanical exfoliation method, where flakes of $TaTe_2$ are exfoliated onto PDMS. A thin flake is selected using an optical microscope, and is then stamped down onto a Si_3N_4 electron microscope grid. The system is then heated to around 76°C and the PDMS is peeled away slowly, leaving the flake on the grid. The cross-sectional orientation requires the use of a focused ion beam. Gallium ions are used to mill trenches through a thin film of $TaTe_2$, which is then removed using a needle and then transferred to a microscope grid.

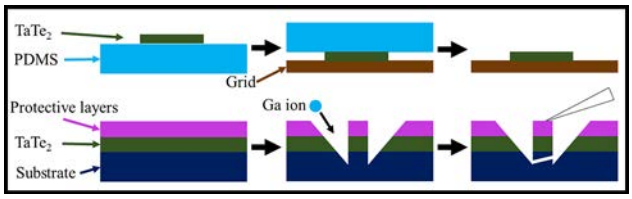

Figure 1: Graphics of sample preparation for plan-view (top), and cross-sections (bottom).

STEM Imaging:

$TaTe_2$ is imaged in plan-view at room temperature and cryogenic temperature (Figure 2). The tantalum atoms are slightly misaligned in their stacking, leading

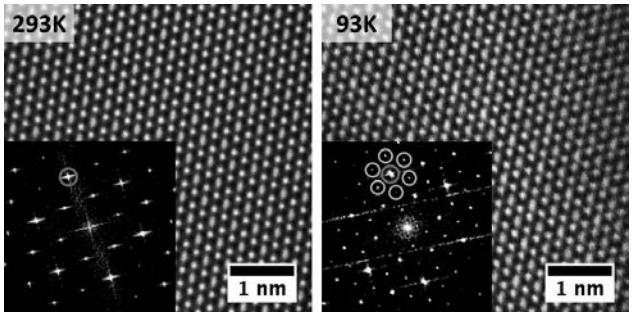

Figure 2: Plan-view STEM images of $TaTe_2$ with FFTs at room and cryogenic temperatures.

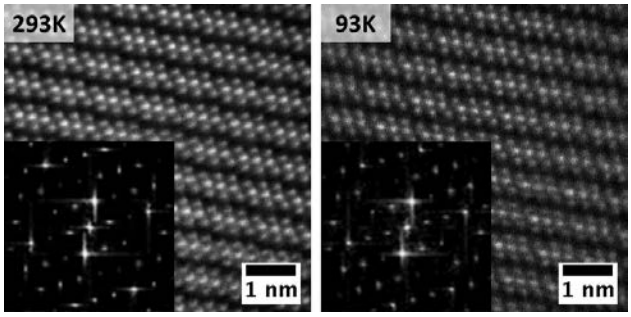

Figure 3: Cross-sectional STEM images of $TaTe_2$ with FFTs at room and cryogenic temperatures.

to an elongated shape, and the tellurium atoms form a hexagonal ring around the tantalum. Imaging at cryogenic temperatures is difficult, due to increased sample drift and the occasional bubbling of the liquid nitrogen. This causes the low temperature images to appear slightly noisier, but atomic resolution is still achieved. Looking at these images, it is not immediately evident that there is a structural change in the material. When comparing the FFTs, each has strong peaks which correspond to the symmetry of the structure, but the cryogenic image shows additional satellite peaks, indicating a structural phase change not easily seen in the real-space images.

The cross-sectional prepared $TaTe_2$ is also imaged at room and cryogenic temperature (Figure 3). The individual layers of the material are distinct and stacked on top of each other. The layers themselves are comprised of rows of tantalum with tellurium on top and bottom. Like the plan-view orientation, the structural change is not clear from the images. Additionally, the structural change is also not visible in the FFTs. This could imply that the structural change is not visible from this orientation, meaning the modulation is occurring along the axis of the electron beam. Looking closely, the tantalum in the center of the layers have larger spacings between every three atoms, which appear to decrease in intensity from left to right. By taking line profiles of several groups of three in each image, the intensity can be averaged and normalized to the far-left peak (Figure 4). The average intensity of the far-right atom is 96% of the far-left atom at room temperature, compared to 88% at cryogenic temperature. This subtle change might be due to a structural change that is not visible in the real-space image or its FFT.

Conclusions and Future Work:

STEM enables atomic resolution imaging of 2D materials to better understand their structure. These experiments show a structural phase transition of $TaTe_2$ in two different orientations at cryogenic temperatures. In the future, $TaTe_2$ will be imaged in different orientations so that the modulation can be extracted from the real-space images. These results will help to build a complete picture of this structural phase, allowing for better utilization of $TaTe_2$ properties.

Acknowledgements:

I would like to thank Dr. Lena Kourkoutis for this opportunity, as well as my mentor Ismail El Baggari and the entire Kourkoutis group for their guidance. This research was also supported by PARADIM and the National Science Foundation (DMR-1120296, DMR-1539918).

References:

[1] H. Chen. EPL. 15 March 2017, 117, 2.

[2] A. Castellanos-Gomez, et al. 2D Materials. April 4, 2014. V1, #1.

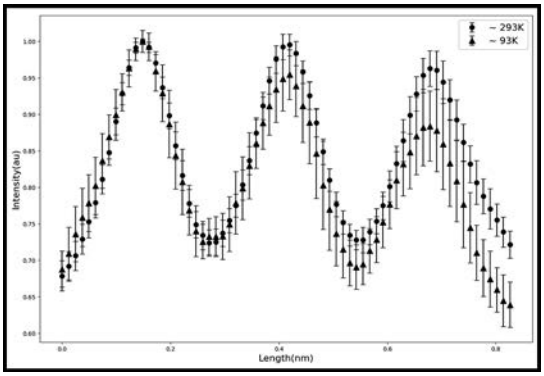

Figure 4: Average intensity across tantalum atoms in groups of three.

Index

PROGRAMS

CNF iREU 2, 16, 30, 32, 34, 38
CNF REU. .. .. .. .14, 22, 24, 28, 36
HHMI EXROP. 8
JHU PARADIM REU.. 12
KEP REU. 4, 26
PARADIM REU.. .. ..10, 18, 20, 42
PARADIM & Caltech SURF. .6, 40

A

Accolla, Robert 2
Agosto Berríos, Natalia. 4
Aizawa, Takashi 30
Anderson, Margaret 6
Archer, Lynden. 26
Avalos, Dante. 8

B

Badman, Ryan 28
Baker, James 8, 28
Bharadwaj, Shyam 14
Bouman, Daniel 10

C

Calcaterra, Heather 12
Chandonait, Jonathan 14
Chen, Guoping 38
Chen, Wei-Liang 24
Choudhury, Snehashis 26
Chrostowski, Robert 16

D

Daniel, Susan 4
Dawley, Natalie. .. .. .18, 40

E

El Baggari, Ismail 42
Elborg, Martin 32

F

Faber, Katherine 6

G

Goldberg, Kaynan.. 18
Grandon, Morgan 20
Guélou, Gabin 30
Guisado, Gabriel 22

H

Hernandez, Christopher 22
Hsieh, David 40

K

Klaczko, Michael. 24
Kourkoutis, Lena 42

L

Lal, Amit.. 36
Langenberg, Eric. 10
López González, Jadiel.. 26
López Martínez, Mónica.. 28

M

Martirossyan, Maya 30
McQueen, Tyrel 12
Mori, Takao.. 30

N

Nair, Hari 20
Nakanishi, Jun 2
Nance, John.. 32
Nathan, Lakshmi. 4
Noda, Takeshi 32

O

Ober, Christopher.. 24
Ohashi, Naoki. 34
Ohsawa, Takeo.. 34

P

Phelan, W. Adam 12

R

Roberts, Melanie 22
Ruyack, Alex 36

S

Sakaki, Hiroyuki 32
Schlom, Darrell
.. .. 6, 10, 18, 20, 40
Sinha, Mekhola. 12
Steinhardt, Rachel 6, 18

T

Tackkett, Skye 34
Takai, Atsuro.. 16
Takeuchi, Masayuki. 16
Tan, Chuang. 8
Teal, Daniel.. 36
Thome, Cooper. 38

V

Vijayakumar, Vibha.. 40

W

Waelder, Jacob.. 42
Wang, Michelle. 8, 28

X

Xing, Huili (Grace) 14

Y

Yamamoto, Shota 2
Yang, Yingjun 38

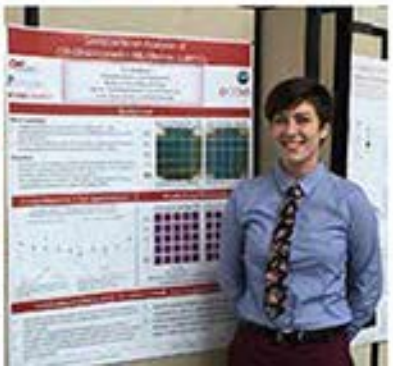

CNF
Cornell NanoScale
Science and Technology Facility

PARADIM
PLATFORM FOR THE ACCELERATED REALIZATION, ANALYSIS & DISCOVERY OF INTERFACE MATERIALS

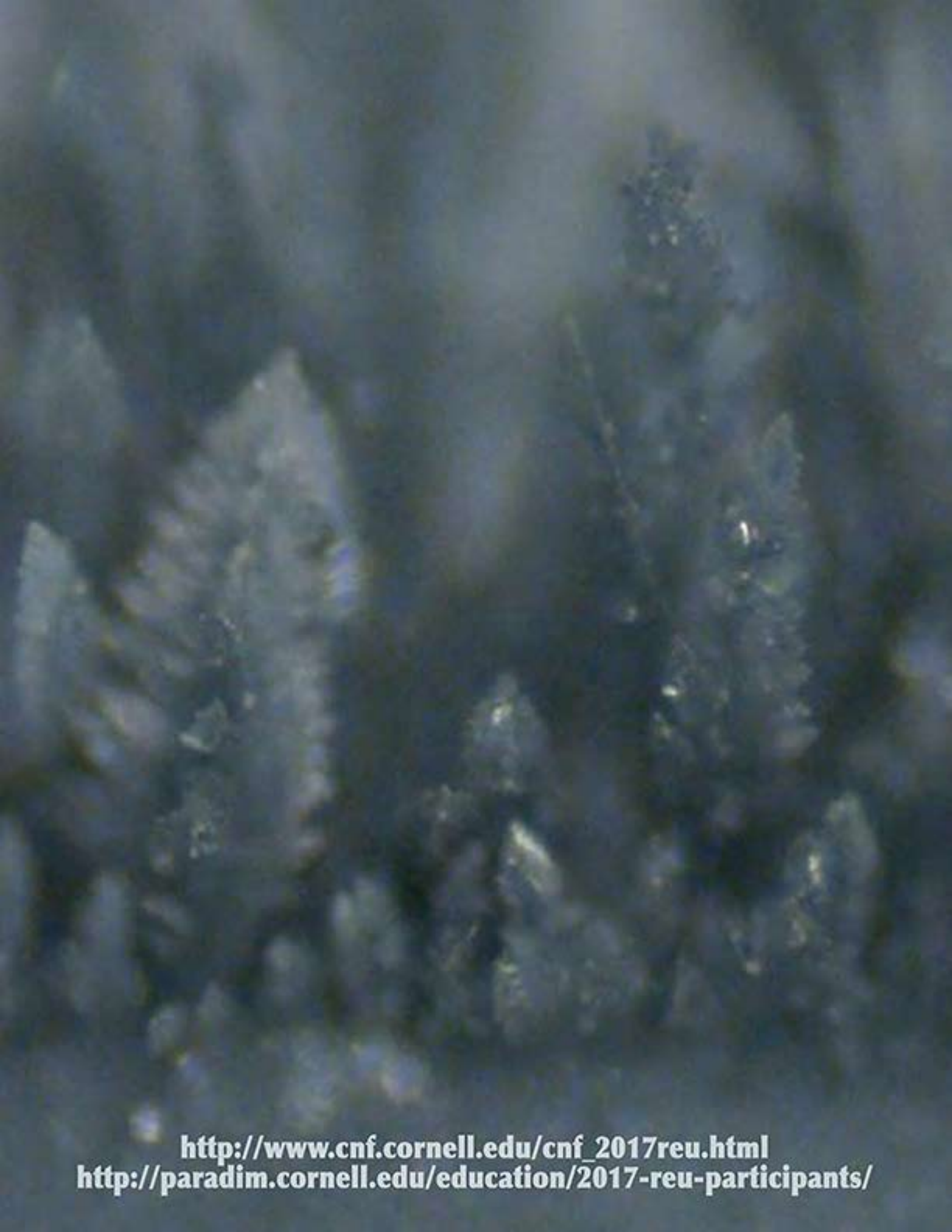
http://www.cnf.cornell.edu/cnf_2017reu.html
http://paradim.cornell.edu/education/2017-reu-participants/